Spectrogram Evaluation of Seismic Risk in Managua, Nicaragua

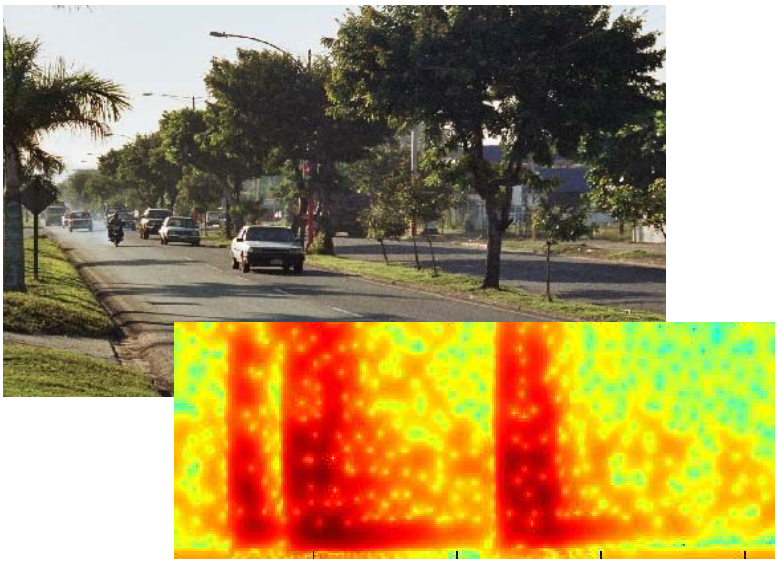

Jonas Hedberg

Master of Science Thesis, 2005

Department of Engineering Geology
Lund Institute of Technology
Lund University

Spectrogram Evaluation of Seismic Risk in Managua, Nicaragua

Jonas Hedberg

Department of Engineering Geology
Lund University
Sweden

ISRN LUTVDG/TVTG--5093--SE

Printed in Sweden

Resumen

Titulo: Spectrogram Evaluation of Seismic Risk in Managua, Nicaragua

Autor: Jonas Hedberg

Supervisor: Peter Ulriksen, Department of Engineering Geology, Lund University.

Co-supervisor: Rainer Manolo Parrales Espinoza, Centro de Investigaciones Geoscientificas, Universidad Nacional Autonoma de Nicaragua.

Descripción del problema: Managua ha sido expuesto a dos grandes terremotos durante el siglo pasado, lo qual ha resultado en grandes pérdida humanas. La destrucción fue particularmente grande en zonas definidas de la ciudad, incluyendo su antiguo centro. Este fenómeno puede ser relacionado con amplificación en los depositos superficiales causada por cambios en impedancia y efectos de resonancia.

Objetivos: El objetivo es de probar un metodo de evaluar resonancia y atenuación de los depositos superficiales utilizando la representación en espectrogramas de la respuesta al impacto. Sería un método rápido para identificar sitios sensitivos ante eventos sismicos, para despues hacer investigaciones de las propiedades dinámicas del suelo con otros métodos.

Metodología: El método utiliza la respuesta del suelo a impactos producidos por vehiculos pesados. Es logrado colocando un obstaculo sobre el pavimiento que hace los vehículos impactar verticalmente el suelo. La respuesta del terreno al impacto es grabada y representado en un espectrograma, que muestra el attenuación en cada frequencia.

Las grabaciones de la respuesta del suelo fueron realizadas en 128 puntos a lo largo de carretera norte y sur de la Pan-Americana, cruzando la ciudad en el terreno bajo cerca del Lago Xolotlán, donde los sedimentos más espesos son previstos. El area incluye el antiguo centro de Managua.

Como método de evaluación el análisis de amenaza frecuencia-tiempo “time-frequency hazard analysis” es desarollado para el estudio. Hace la convolución de la espectrograma en cada instante con un espectro típico de terremoto y un espectro de respuesta de casa para obtener una estimación del riesgo local ante los sismos.

Conclusiones: En general frequencias de resonancia no son presentes en los espectrogramas. Solo cinco sitios muestran una frequencia prevalente.

La característica transiente de los señales grabadas puede resultar en picos menos distinctos al respecto de aquellos obtenidos con un análisis de microtremores, dado que la resolución en frequencia mejora con ventanas más largas en el tiempo. Resonancias débiles entonces pueden ser dificiles de interpretar, pero resonancias que amplifica considerablemente amplitudes de oscillación aparecen, dado que el impacto del vehiculo contiene frequencias suficientemente bajas para excitar la frequencia de resonancia fundamental de los depósitos superficiales.

El “time-frequency hazard analysis” da una medida integral de la resonancia y atenuación sin precisar una interpretación subjetiva.

La interpretación de espectrogramas y los resultados del análisis de amenaza frecuencia-tiempo “time-frequency hazard analysis” muestran que los depósitos superficiales en general son bastante competentes para no producir amplificaciones debidas a resonancia, con la excepción de zonas muy locales y el area del antiguo centro de ciudad.

Palabras claves: Terremotos, Managua, Nicaragua, Respuesta de sitio, Espectrograma, Riesgo local, Vulnerabilidad, Tectonica, Fallas, Resonancia, Atenuación, Amortiguamento, Impedancia, Nakamura, Propriedades dínamicas, Depositos superficiales, Sedimentos, Suelo, Geofísica, Analisis espectral, Desastres naturales, CIGEO, UNAN, ASDI, MFS, Geología.

Abstract

Title: Spectrogram Evaluation of Seismic Risk in Managua, Nicaragua

Author: Jonas Hedberg

Supervisor: Peter Ulriksen, Department of Engineering Geology, Lund University.

Co-supervisor: Rainer Manolo Parrales Espinoza, Centro de Investigaciones Geoscientificas, Universidad Nacional Autonoma de Nicaragua.

Problem description: Managua has experienced two devastating earthquakes during the last century resulting in major human loss. The destruction in the earthquake of 1972 was particularly severe in defined areas of the city, including the former city centre, which is now unused terrain. This may have been because of amplification in those areas due to impedance contrasts and resonance effects in the surface layers.

Objective: The aim is to test a method of evaluating resonance and attenuation in the surface layers by imaging the traffic impulse response in a spectrogram. This would be a fast method of identifying earthquake-sensitive sites for more thorough investigation of the dynamic properties with other methods.

Methodology: The traffic impulse response method uses heavy vehicles as a seismic source. This is done by placing an obstacle over the road which causes the vehicles to vertically impact the ground. The ground response to that impact is then recorded and represented in a spectrogram image, where the attenuation with time on each frequency can be seen.
Measurements are carried out at 128 sites along the Pan-American Highway crossing the city in the low area close to Lake Xolotlán where the sediments can be expected to be the thickest. These include the area where the former city centre was located.
The time-frequency hazard analysis is developed as an evaluation method for this study. It convolves the spectrogram at each time instant with a typical earthquake

spectrum and a building response spectrum in order to obtain an estimate of the local seismic risk.

Conclusions: In the measurements resonances are generally not seen in the spectrograms. Only five sites exhibit clear prevailing frequencies.
The transient nature of the impulse response may provide resonance peaks less distinct than in microtremor analysis, as the frequency resolution improves with a longer time window. Weak resonances may thus be hard to interpret from the spectrogram but resonances that can considerably amplify earthquake motion will show, as long as the vehicle impact contains power at sufficiently low frequencies to not miss the surface layer resonance peak.
The time-frequency hazard analysis gives an integrate measure of resonance and attenuation without having to rely on subjective interpretation.
The spectrogram interpretation and the time-frequency hazard analysis show that the surface layers along the Pan-American Highway are generally competent enough not to give rise to any resonance amplification, with the exception of very localized zones and in the area of the city centre.

Keywords: Earthquakes, Managua, Nicaragua, Site response, Traffic impulse response, Spectrogram, Time-frequenzy hazard analysis, Local risk, Vulnerability, Earthquake-sensitivity, Short-term Fourier transform, Tectonics, Faults, Elastic rebound, Resonance, Attenuation, Damping, Impedance, Nakamura, Dynamic properties, Surface layers, Sediment, Soil, Geophysics, In-situ testing, Frequency analysis, Natural disasters, CIGEO, UNAN, SIDA, ASDI, MFS, Geology.

LUNDS TEKNISKA HÖGSKOLA
Lunds universitet

Lund University
Lund Institute of Technology
Department of Engineering Geology

This study has been carried out within the framework of the Minor Field Studies (MFS) Scholarship Programme, which is funded by the Swedish International Development Cooperation Agency, Sida.

The MFS Scholarship Programme offers Swedish university students an opportunity to carry out two months' field work in a developing country resulting in a graduation thesis work, a Master's dissertation or a similar in-depth study. These studies are primarily conducted within subject areas that are important from an international development perspective and in a country supported by Swedish international development assistance.

The main purpose of the MFS Programme is to enhance Swedish university students' knowledge and understanding of developing countries and their problems. An MFS should provide the student with initial experience of conditions in such a country. A further purpose is to widen the human resource base for recruitment into international co-operation. Further information can be reached at the following internet address: http://www.tg.lth.se/mfs

The responsibility for the accuracy of the information presented in this MFS report rests entirely with the authors and their supervisors.

Gerhard Barmen
Local MFS Programme Officer

Preface

This study has been carried out as part of the collaboration between Centro de Investigaciones Geoscientificas (CIGEO) at Universidad Nacional Autonoma de Nicaragua in Managua, and the Department of Engineering Geology at Lund University.

Rainer Parrales, engineer from CIGEO in Managua, is carrying out a study on the earthquake sensitivity of soils in the Managua area. This work is intended to form part of that study.

I would like to give my gratitude to the supervisor of this project, Peter Ulriksen, for his generous support and valuable feedback.

An equally great thanks to co-supervisor Rainer Parrales for giving me the support I needed in Managua and for making me feel at home there. He also proved an excellent field work partner.

A special thanks to Dionisio Rodriguez, head of department at CIGEO, and Marvin Valle, vice head of department, for providing the logistic support necessary to carry out the measurements along the Pan-American Highway.

To Roger Blandón for valuable support and coming with creative solutions in the field.

To Orlando Hernandez Rubio of the Managua Municipality for providing material used in this study.

To all the staff at CIGEO for giving me a good stay in Nicaragua and for practical support.

I would also like to give my gratitude to the Swedish International Development Cooperation Agency for providing the financial possibility to carry through with this project.

Finally but most importantly to the drivers of Managua for their spiritfull driving, without them this project could not have been realized.

Jonas Hedberg, Lund 16th of May 2005.

Table of contents

1 Introduction

1.1 Background

Managua, the capital of Nicaragua, lies in a seismically active part of the country. Its population has experienced two catastrophic earthquakes in the past century with major human loss as a consequence. These occurred in 1931 and 1972.
The Earthquake of 1972 caused the destruction of the old city centre of Managua and the loss of approximately 10000 human lives (Incer Barquero et al., 2000). The major destruction occurred in defined areas of the city, which may indicate that the thickness of surface layers played an important role in the resulting surface movement and rendered some parts of the city more vulnerable than others. This led to a prohibition of construction in the most damaged areas of the city centre which still is in effect.

Figure 1.1 A collapsed five-story building in the 1972 earthquake.

Managua is a growing city and in need of the areas now deemed unfit for construction. If the earthquake vulnerable areas are mapped out and the dynamic properties of their surface layers investigated, earthquake-safe buildings could be constructed on the now unexploited grounds.

1.2 Objectives

This work is aimed at testing the Spectrogram Evaluation Technique as a method of fast identification of earthquake-sensitive sites. This operation would be a first step in a strategy to evaluate Seismic Risk in Managua. After that more thorough investigations to evaluate the soil's dynamic properties at the vulnerable sites can be undertaken.

A vulnerable site can be the result of various properties in the soil strata. For one the passage of the earthquake shockwaves from hard bedrock to softer surface materials will cause a growth in vibration amplitude. In addition to that the surface layers may enter into resonance. This can occur if the combined layers have a resonance frequency within the frequency domain of the earthquake, and in addition a sufficiently low attenuation to permit a build-up of energy in the resonance mode during the duration of the earthquake. Therefore the resonance modes and the attenuation are of special interest in the identification of vulnerable sites.

A microzonation study using the Nakamura technique has already been carried out in the central parts of Managua by Stål and Westberg (Stål and Westberg, 1996). The Nakamura technique is ideal for use in urban areas as it uses microtremors as seismic source and thus benefits from the background noise that presents an obstacle to most other seismic surveys. It gives the fundamental resonance frequency and the shear wave transfer function of the sedimentary layers.

It is not possible, however, to determine the soil attenuation with Nakamura's technique.

Use of the Spectrogram Evaluation Method could provide all the resonance modes (not only the fundamental), and an estimate of the soil attenuation.

The spectrogram evaluation technique uses heavy traffic as seismic source and is thus quick to use, although the necessity of proximity to major routes means a certain limitation. In Managua the passage of the Pan-American Highway through the city in a right-angle to the faulting direction provides us with an ideal seismic source along which the measurements can be made. It crosses the area of Managua bordering to Lake Xonotlán where the former city centre lay before the earthquake of -72.

In the field study measurements of both microtremors and active traffic sources have been made to enable the use of both the Nakamura and the Spectrogram Evaluation Technique, but the analysis with Nakamura's technique is outside the scope of this masters' thesis.

Figure 1.2 Map of Nicaragua (CIA, 1997).

2 Tectonics

2.1 Moving plates

It is today known that the Earth's lithosphere is divided into several tectonic plates that move relative to one another (Figure 2.2). Although the mechanism behind this motion cannot be seen, it is believed to be caused by convection in the semi-solid Mantle of the earth (Figure 2.1). In this chapter information is taken from the U.S. Geological Survey (Kious and Tilling).

2.1.1 The mechanism of plate drift

The traces that can be seen on the earth's surface of this supposed convection process are the mid-ocean ridges and oceanic trenches. The ridges are formed by magma pushing up from the mantle and causing spreading of the sea-floor, a divergent boundary. The best known divergent boundary is the Mid-Atlantic Ridge that spreads the Atlantic sea-floor at a relative rate of 2.5 cm per year.

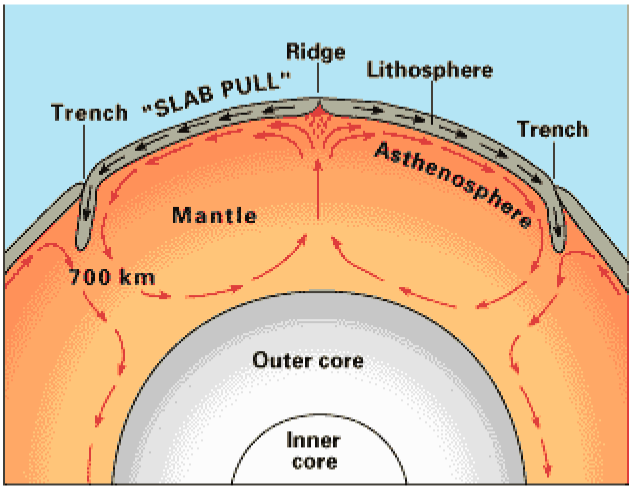

Figure 2.1 Convection cell in Mantle (USGS)

The spreading of the sea-floor implicates the collision of plates along other, convergent, boundaries. If an oceanic plate encounters a continental plate, the continental plate will force down the heavier oceanic plate into the Mantle. This will cause the most profound depths of the ocean, the trenches. Below a depth of about 700 km, the descending plate begins to soften and lose its form because of the increasing heat. The material sinks closer to the earth's core where it gets reheated and lighter and starts to rise again, completing the convection cell.
A convection cell needs a source of heat to be initiated and kept alive. The heat comes from two sources: radioactive decay of elements in the earth's core and residual heat left from the collapse and compression of material at the birth of the planet.
Until the 1990s the sea-floor spreading prevailed as the chief motive force behind the continental drift. Today the subduction in the convergent zones is considered a bigger motive force. The sinking subdued slab pulls the rest of the plate with it in its fall through the Mantle.

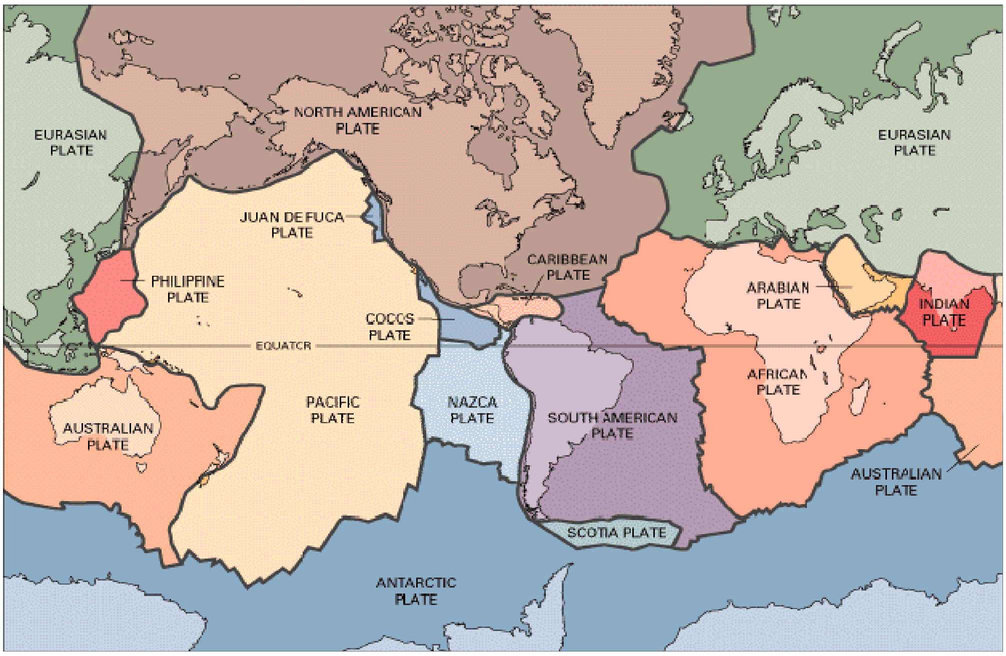

Figure 2.2 Tectonic plates of the world (Kious and Tilling).

The interaction between plates is the main cause of earthquakes. Even if the relative velocity between plates is only a few centimetres per year the mass of the motion builds up an enormous potential energy, which is released when the local shear strength of the material is exceeded. There are four basic ways in which two plates can interact along a boundary to build up stresses in the Earth's crust. These are called divergent boundaries, collision boundaries, subduction boundaries and transform boundaries.

2.1.2 Divergent boundaries

In the divergent boundaries magma is pushing up from the mantle and creates new crust material. In this process the plates are pushed apart and a spreading ridge is formed. The Mid-Atlantic ridge is a submerged spreading ridge that stretches from the Arctic region to beyond the southern tip of Africa. Most spreading ridges occur in the oceans, but the Great Rift Valley is an example of a continental spreading centre. It stretches from Lebanon, through Eastern Africa and all the way to Mocambique.

2.1.3 Collision boundaries

When two continental plates collide head-on (Figure 2.3) neither is subdued, because both are relatively light and resist downward motion. Instead they tend to buckle and push each other upwards or sideways. One will usually override the other and crumple up to create a mountain range, like in the case of Himalaya.

2.1.4 Subduction boundaries

A plate subduction occurs either when an oceanic plate collides with a continental plate, or when two oceanic plates collide (Figure 2.3).

In the first case the heavier oceanic plate will be forced down under the thicker but lighter continental plate. The continental plate crumples up under the stress to form a coastal mountain range. Normally there is volcanic activity in connection with the subduction zone, but if the source of the magma is the melting of the subdued slab or the continental slab, or both, is still not known.

If two oceanic plates collide one will be forced down under the other to form a trench. Like in the case of oceanic-continental convergence volcanoes form parallel to the trench. After millions of years piling up volcanic debris on the sea-floor they can form Island arcs, like the Marianas and the Aleutian Islands.

2.1.5 Transform boundaries

Two plates sliding past one another form transform boundaries. Normally they occur on the ocean floor, where they offset the spreading ridges and create the zig-zag pattern seen in for example the Mid-Atlantic Ridge.

But the San Andreas Fault in California is an example of a transform boundary that crosses land. It connects the East Pacific Rise, a spreading ridge to the south, with the South Gorda-Juan de Fuca-Explorer Ridge to the north (Figure 2.4).

Along it the Pacific Plate has been grinding past the North American Plate for 10 million years at a rate of 5 cm per year.

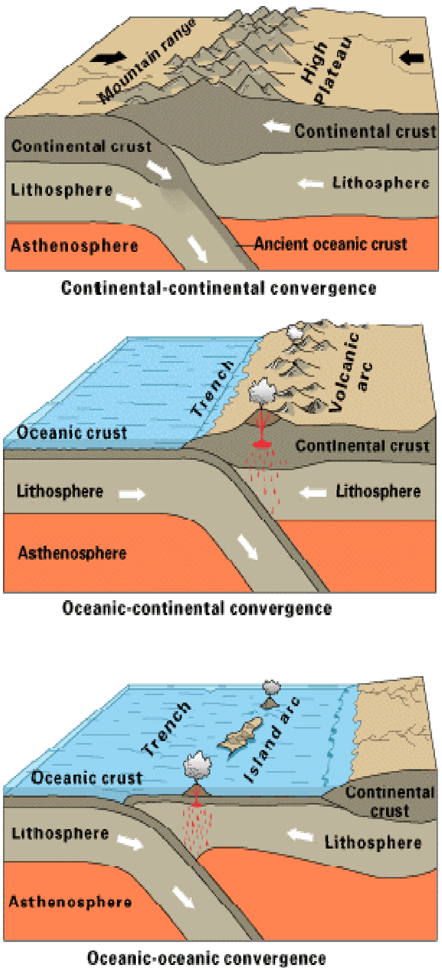

Figure 2.3 Convergent boundaries. Two Continental plates moving together form a Collision boundary. An oceanic and a continental plate, or two oceanic plates, moving together form a subduction boundary (Kious and Tilling).

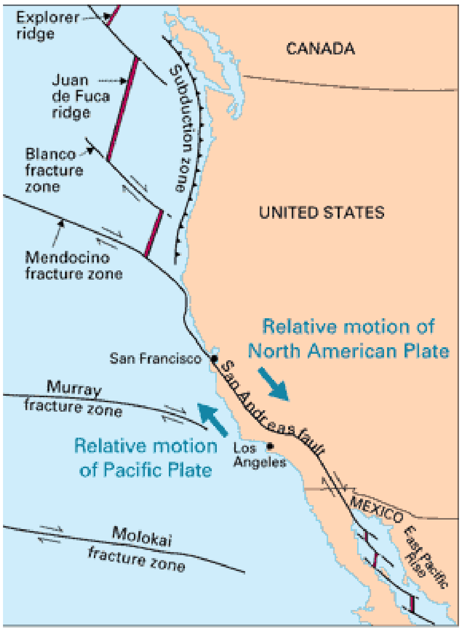

Figure 2.4 The San Andreas Fault and some ocean floor transform faults (Kious and Tilling).

2.2 Fault kinematics

In the boundaries between tectonic plates great stresses build up. The part of the tectonic plate close to the boundary deforms under the stress and fractures. This gives rise to heavy faulting close to plate boundaries. Like with plate boundaries the faces of the fault build up stress under the deformation until their shear strength is reached and they rupture. This is explained in the Elastic Rebound Theory.

2.2.1 Elastic rebound

When shear deformation occurs in the crust, elastic strain energy will build up in the rock. This build-up will go on until the shear strength in the rock is reached along the weakest plane. The weakest plane will usually be along a pre-existent fault. The rock faces of a fault are usually rough and enable enormous stresses to build up before slipping.

In Figure 2.5 the process of stress build-up and rupture in a strike-slip fault is shown. The fence crossing the fault shows the deformation in the ground.

Initially the ground is not deformed and the fence goes in a straight line over the fault. Then tectonical movement causes shear forces in the ground, but the interlock friction between the fault faces resist slip. The ground deforms and builds up elastic strain energy.

When the friction cannot resist anymore the fault slips and the ground ruptures. The

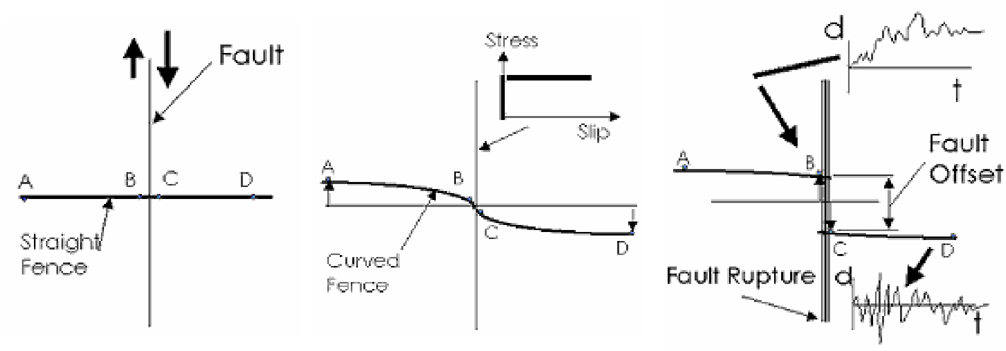

Figure 2.5 Elastic Rebound in a strike-slip fault (Mahin).

edges of the fault try to catch up with the middle as they release their potential energy, but don't quite make it due to fault drag. The fence remains slightly curved.

It follows that if the rock strength, fault length and slip rate are known, it is possible to calculate the time it will take to build up enough strain energy to cause an earthquake, and its probable magnitude.
When rupture occurs and the stress drops in one fault, other faults in the same system will have to carry its load. Frequently other faults will then rupture as a consequence of the first, a fault swarm is released. If other faults in the system do not rupture their next slip will in any case be rescheduled to an earlier date due to the added shear load they have received.

2.2.2 Fault geometry

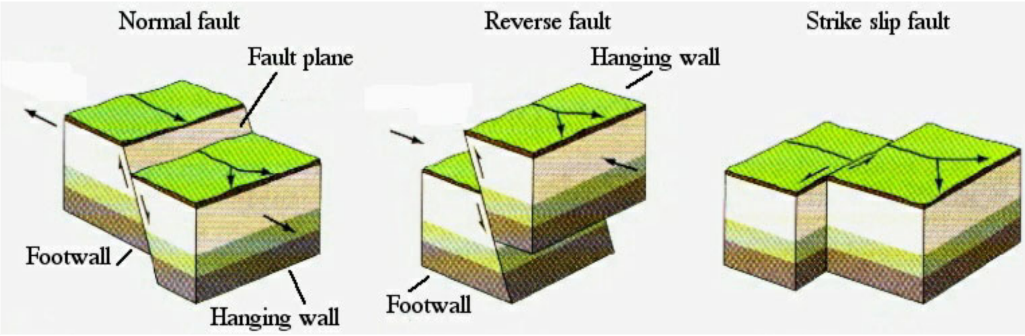

Figure 2.6 Normal faulting, reverse faulting and strike-slip faulting (Rey, 2003).

There are three ways in which two blocks can move relative to one another in a fault (Figure 2.6).
Normal faults and **reverse faults** are both dip-slip faults which implicates a dipped fault plane with a vertical relative movement between the blocks.
In a normal fault the two blocks move away from one other and the hanging wall is sinking relative to the footwall. In a reverse fault the two blocks are pushed together and the hanging wall rises above the footwall.
A **strike-slip fault** has no dip and the walls move only horizontally relative to one another. It is dextral if the motion is clockwise and sinistral if the motion is counter-clockwise.
These fault types rarely occur in their pure forms. Usually a fault has a combined dip-slip and strike-slip motion.

2.3 Regional tectonic setting

Nicaragua occupies a segment of the Central American land strip connecting North America to South America, thus having both a Caribbean and a Pacific Coastline. It lies on the so called Ring of Fire (Figure 2.7) encircling the Pacific Ocean, with a high rate of seismic and volcanic activity.

About 120 km off the Pacific coast runs the Middle American trench, marking the border between the Cocos and the Caribbean tectonic plate (Figure 2.2). The two plates are converging at a relative velocity of about 8 cm/year. In the collision the Cocos Plate is subdued by the Caribbean plate and thrust down at an angle of approximately 80° (Cowan et al., 2000). The collision has given rise to the Central American Volcanic Front running parallell the Middle American Trench at a distance of about 170 km into the Caribbean Plate and stretching from Costa Rica to Guatemala.

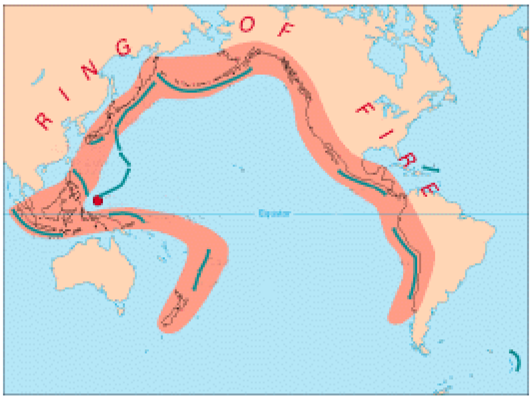

Figure 2.7 The Pacific Ring of Fire (Kious and Tilling).

2.4 The faulting in Managua

The Central American Volcanic Front is abruptly displaced in the area of Managua (Figure 2.8). The reason for this displacement is not clear. One theory suggests that the Cocos Plate may be segmented under the Caribbean Plate. The plate segments are subducted at different angles and create a lateral offset in the volcanic chain. Another suggestion is that the volcanic chain is actually a spreading rift. The displacement would then be analogous to the offset caused by transform boundaries seen in ocean spreading ridges and in the Great Rift Valley (see chapter 2.1.5). It remains to be investigated if there's an active extension going on in the Nicaraguan depression.

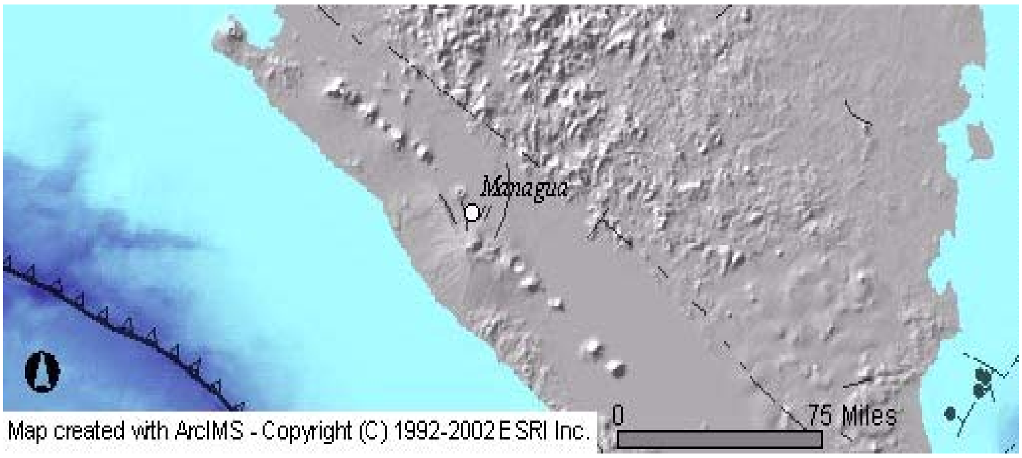

Figure 2.8 Topographic map showing the interruption of the volcanic front at Managua. The black lines indicate major faults, the jagged line indicates the subduction zone of the Middle American Trench (French and Schenk).

Whatever the explanation is for the displacement, the consequence is a pull-apart graben with numerous quaternary fault systems running through it (the quaternary is a geological time period which can be seen in Figure 3.2 in chapter 3).
The western boundary of the graben is defined by volcanic cinder cones and collapse pits extending south from the Apoyeque Caldera, known as the Nejapa-Miraflores alignment. The Asososca-Acahualinca and San Judas Faults (NI-04 in Figure 2.9) form east-facing escarpments along this alignment. The eastern boundary is formed by the Cofradia fault system (NI-09 in Figure 2.9), a prominent west-facing escarpment rising up to 15 meters above the graben floor.

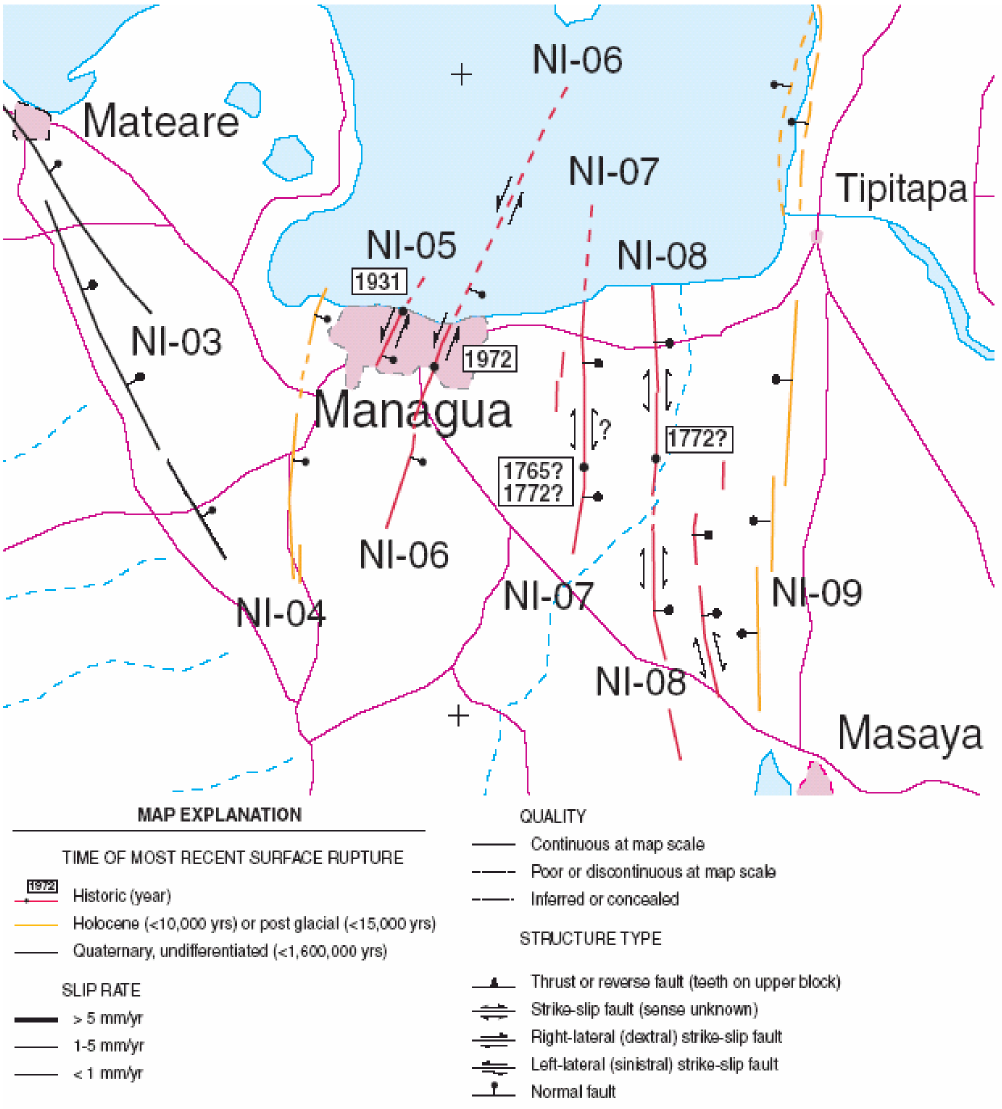

Figure 2.9 Quaternary faults in the vicinity of Managua (Cowan et al., 2000).

QUATERNARY FAULTS OF NICARAGUA
LAS FALLAS CUATERNARIAS DE NICARAGUA

Number Número	Name of structure Nombre de estructura	Sense of movement (major/minor) Sentido de movimiento (mayor/menor)	Time of most recent movement Edad del último movimiento	Slip rate (mm/yr) Tasa de movimiento (mm/año)
NI-01	La Pelona fault zone	Unknown	<15 ka	<1.0
NI-02	La Paz Centro fault zone	Unknown	<15 ka	0.2-1.0
NI-03	Mateare fault zone	Unknown	<1.6 Ma	0.2-1.0 (?)
NI-04	Asososca-Acahualinca and San Judas fault zone (Managua graben)	Unknown	<15 ka	0.2-1.0 (?)
NI-05	Estadio fault	Left-lateral	Historic (1931)	0.2-1.0 (?)
NI-06	Tiscapa fault	Left-lateral	Historic (1972)	0.2-1.0 (?)
NI-07	Aeropuerto fault	Strike slip	Historic (1650-1880, possibly 1765 or 1772)	0.2-1.0 (?)
NI-08	Unnamed faults, Eastern Managua graben	Strike slip	<15ka, possibly historic (1772?)	0.2-1.0 (?)
NI-09	Cofradia Fault, Eastern Managua graben	Normal	<15 ka	<1.2
NI-10	Ochomogo fault zone	Not reported	<15 ka	0.2-1.0 (?)

Table 2.1 Quaternary faults in the vicinity of Managua (Cowan et al., 2000).

The graben hosts a closely spaced system of NE-SW-trending strike-slip and oblique-normal faults. Many of the faults are slightly curved. The strike-slip faults for which the sense of movement has been determined show a sinistral (counter-clockwise) movement, which seems anomalous in view of the dextral offset in the volcanic chain. This relation has not yet been resolved, neither has the curvature of the faults. The regional kinematics is not clear.

The faults within the Managua Graben have been responsible for the two catastrophic earthquakes in the 20th century. Though the magnitude of the events is small or moderate they are capable of producing severe damages because of their shallow depth. The earthquakes occur in cycles at depths between 5 to 12 km (Parrales Espinoza and Picado Romero, 2001).

The elastic rebound in the Estadio Fault (NI-05 in Figure 2.9) in 1931 caused a 2 km long surface rupture and the loss of approximately 1000 human lives.

The Tiscapa Fault (NI-06 in Figure 2.9) was the cause of the 1972 Earthquake, in which around 10000 people died and the downtown area was destroyed. The movement occurred in 4 faults in the system with rupture lengths from 1.6 to 5.9 km, totalling 15.4 km.

Figure 2.10 A ground rupture in the pavement in the 1972 earthquake.

Another fault which has shown to be active in historic time is the Aeropuerto fault (NI-07 in Figure 2.9) running through the eastern part of the city and continuing in Lake Xonotlán with a NE-SW orientation. Palaeontologists have

detected historical events in the fault, the last one of which occurred sometime between 1650 and 1880.
All the faults in and around the Managua graben should be considered active; even the faults for which no historical event has been registered.

2.5 Seismic sources

There are three sources capable of creating seismic events in the Pacific Region of Nicaragua:

- The subduction zone
- The volcanoes
- The local faults

All sources are connected to the subduction process of the Cocos Plate beneath the Caribbean Plate.

2.5.1 The subduction zone

The Cocos plate is subducted beneath the Caribbean plate at a rate of about 8 cm per year. But it is not a constant process. Enormous stresses are built up until the local shear strength is reached. Then the elastic rebound takes place and releases the strain energy in the form of seismic shockwaves that travel through the crust in all directions. These ruptures occur in segments at a time, creating earthquakes in cycles. The earthquakes with focus in the subduction zone are often very powerful but luckily have to travel a long distance before reaching the surface and are attenuated before reaching populated areas. They are normally characterized by long-period surface waves, as the short-period components have been attenuated in the passage through the crust.

2.5.2 The volcanoes

The volcanoes may also create seismic events. Beneath the volcanoes the lithosphere is thinner. The time before a volcanic eruption takes place, the crust is in a state of increasingly high stress which may result in the elastic rebound of surrounding faults.

2.5.3 The local faults

The earthquakes that occur in the local faults in and around the Managua Graben are relatively small in magnitude, but because of the shallow focal depth they get much less attenuated before reaching surface. Also they will have a higher frequency content, probably with specific kinds of damages associated to it. The Earthquake of 1972 had the moderate magnitude of 5.6 but still succeeded in destroying the capital. 10.000 lost their lives, 20.000 were injured and 250.000 were left without a home (Incer Barquero et al., 2000).
The faults in the Managua area are highly active and are responsible for most of the seismic activity in the region (Parrales Espinoza and Picado Romero, 2001).

3 Geology

3.1 The geological setting of Managua

3.1.1 Geomorphology

A low plain known as the Nicaraguan depression dominates Western Nicaragua. It encompasses Lake Xolotlàn and Lake Cocibolca (also known as Lake Managua and Lake Nicaragua). The capital city of Managua lies on the southern shores of Lake Xolotlàn in the highly active Managua Graben.

The Nicaraguan depression is limited to the northeast by the Interior Highlands and to the southwest by the Pacific Ocean. South of Puerto Sandino begins the Cordillera del Pacifico, locally known as Las Sierras de Managua, forming a coastal mountain range separating the southern part of the depression from the Ocean.

The still active Central American Volcanic Front runs through the Nicaraguan

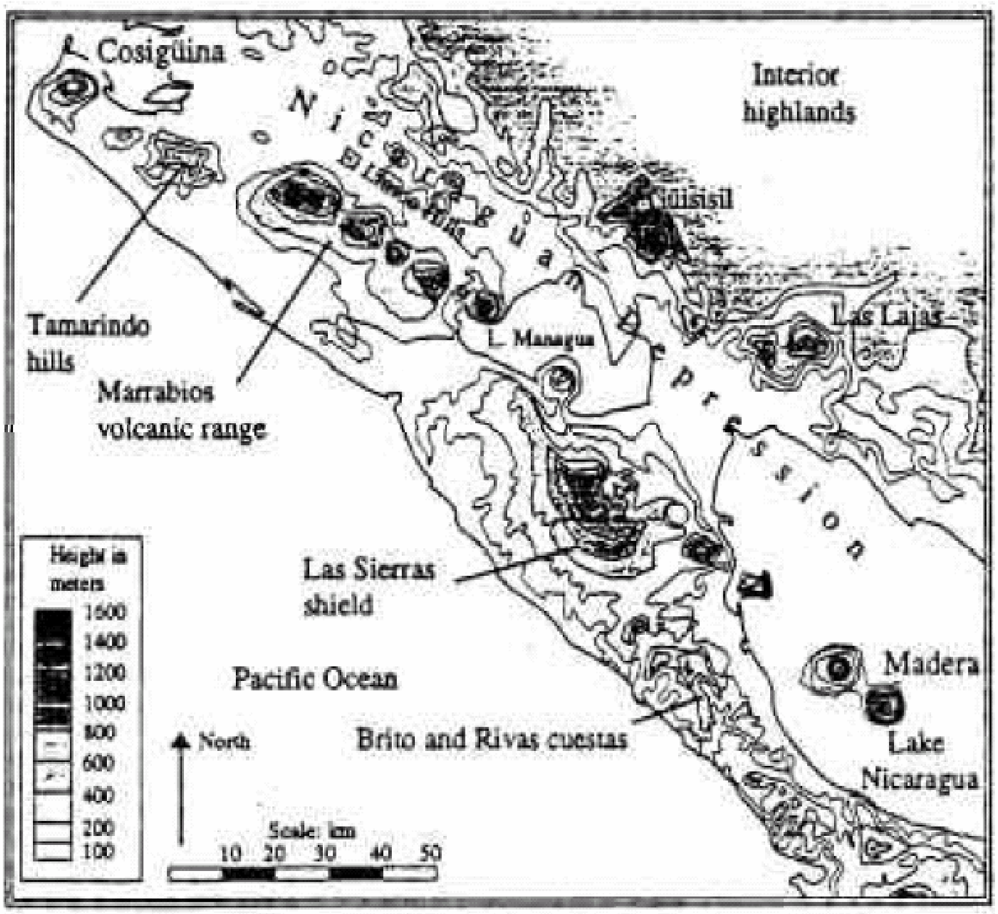

Figure 3.1 Geomorphological map of western Nicaragua (van Wyk de Vries, 1993).

Depression from the Cosigüina volcano in the northwest to the Maderas volcano in Lake Nicaragua. The whole volcanic front stretches all the way from Tacaná Volcano in Guatemala to Irazú in Costa Rica (van Wyk de Vries, 1993).

ERA	PERIOD		EPOCH		AGE	Million years	Abbreviation	Duration (Ma)
CENOZOIC	QUATERNARY		HOLOCENE			0.1	Hol	0.1
			PLEISTOCENE			1.6	Ple	1.5
	TERTIARY	Neogene	PLIOCENE	upper	PIACENZIAN	3.5	Pla	1.9
				lower	ZANCLIAN	5.2	Zan	2.3
			MIOCENE	upper	MESSINIAN	6.3	Mes	1.1
					TORTONIAN	10.2	Tor	4.9
				middle	SERRAVALLIAN	15.2	Srv	5
					LANGHIAN	16.2	Lan	1
				lower	BURDIGALIENSE	20	But	3.8
					AQUITANIAN	25.2	Aqt	5.2
		Paleogene	OLIGOCENE	upper	CHATTIAN	30	Cht	4.8
				lower	RUPELIAN	36	Rup	6
			EOCENE	upper	PRIABONIAN	39.4	Prb	3.4
				middle	BARTONIAN	42	Brt	2.6
					LUTETIAN	49	Lut	7
				lower	YPRESIAN	54	Ypr	7
			PALEOCENE	upper	THANETIAN	60.2	Tha	3.8
				lower	DANIAN	66.5	Dan	6.3
MESOZOIC	Cretaceous		upper	Senonian	MAASTRICHTIAN	74	Maa	7.5
					CAMPANIAN	84	Cmp	10
					SANTONIAN	88	San	4
					CONIACIAN	89	Con	1
					TURONIAN	92	Tur	3
					CENOMANIAN	95	Cen	4
			lower		ALBIAN	108	Alb	12
					APTIAN	113	Apt	5
					BARREMIAN	116.5	Brm	3.5
				Neocomian	HAUTERIVIAN	121	Hau	4.5
					VALANGINIAN	128	Vlg	9
					BERRIASIAN	134	Ber	6
	Jurassic		Malm (Late Jurassic)		TITHONIAN	139	Tth	5
					KIMMERIDGIAN	146	Kim	7
					OXFORDIAN	152	Oxf	6
			Dogger (Middle Jurassic)		CALLOVIAN	157	Clv	5
					BATHONIAN	166	Bth	9
					BAJOCIAN	171	Baj	5
					AALINIAN	179	Aal	8
			Lias (Lower Jurassic)		TORCIAN	186	Toa	7
					PLIENSBACHIAN	194	Plb	8
					SINEMURIAN	201	Sin	7
					HETTANGIAN	210	Het	9
	Triassic		Tr3		RHAETIAN	215	Rht	5
					NORIAN	223	Nor	8
					CARNIAN	231	Crn	8
			Tr2		LADINIAN	236	Lad	5
					ANISIAN	240	Ans	4
			Scythian		(3 stages)	250	Scy	10

Figure 3.2 The Geological Timetable, the Mesozoic and Cenozoic eras (Lapiedra).

ERA	PERIOD	EPOCH		AGE	Million years	Abbreviation	Duration (Ma)
PALEOZOIC	Permian	upper		TATARIAN	250	Tat	5
				KAZANIAN	255	Kaz	5
		lower		KUNGURIAN	260	Kun	10
				ARTINSKIAN	270	Art	5
				SAKMARIAN	275	Sak	5
				ASSELIAN	280	Ass	10
	Carboniferous	STEPHANIAN	GZELIAN	2 stages	290	Gze	5
			KASIMUVIAN	3 stages	295	Kas	8
		WESTPHALIAN	MOSCOVIAN	4 stages	303	Mos	8
			BASHKIRIAN	5 stages	311	Bah	12
		NAMURIAN	SERPUNKNOV.	4 stages	323	Spk	10
		VISEAN		5 stages	333	Vis	17
		TOURNAISIAN		2 stages	350	Tou	12
	Devonian	D3		FAMENNIAN	362	Fam	5
				FRASNIAN	367	Frs	10
		D2		GIVETIAN	377	Glv	4
				EIFELIAN	381	Eif	5
		D1		EMSIAN	386	Ems	4
				PRGIAN	390	Pra	6
				LOCHKOVIAN	396	Lok	12
	Silúrico	PRIDOLI			408	Prl	3
		LUDLOW		2 stages	411	Ldf	4
		WENLOCK		3 stages	415	Wen	15
		LLANDOVERY		3 stages	430	Lly	9
	Ordovician	Bala	ASHGILL	4 stages	439	Ash	4
			CARADOC	7 stages	443	Crd	21
		Dyfed	LLANDELO	3 stages	464	Llo	4
			LLANVIRN	2 stages	468	Lln	8
		Canadian	ARENIG		476	Arg	17
			TREMADOC		493	Tre	17
	Cambrian	Merioneth		2 stages	510	C3	7
		St David's		2 stages	517	C2	19
		Caerfai		3 stages	536	C1	34
PRECAMBRIAN					570		

Figure 3.3 The Geological Timetable, the Paleozoic era (Lapiedra).

3.1.2 Geological provinces of Nicaragua

Nicaragua can be divided into four geological provinces in terms of the origins of the bedrock (van Wyk de Vries, 1993). They run parallel to the Middle American Trench and the Pacific coastline.

1. **The Pacific Coastal Plain** is composed of tertiary (see geological timetable in Figure 3.2) marine sediments and ignimbrites of volcanic origin. The closeness to the subduction zone gives rise to folding of the tertiary marine rocks and a faulting that runs parallel to the Middle American Trench.
   The Brito and Rivas slopes (marked as B and R in Figure 3.4) are tertiary marine rocks lifted up by the intense compression from the colliding tectonic plates. They are highest to the southwest were deformation is greatest. Further northwest they are covered by the less tilted El Fraile formation

(marked as F in Figure 3.4). This in turn is limited to the north by undeformed rock of shallow marine, lacustrine and terrestrial sediments with interspersed ignimbrites, belonging to the Tamarindo formation (marked as T in Figure 3.4).

The Pacific Region has its origin in an offshore basin formed in The Miocene-Pliocene by the subduction process. In it the sediments that became the Rivas, Brito, Masachapa and El Fraile formations were deposited. The basin, now called the Nicaraguan Trough, rose from the Sea in the Pliocene-Pleistocene.

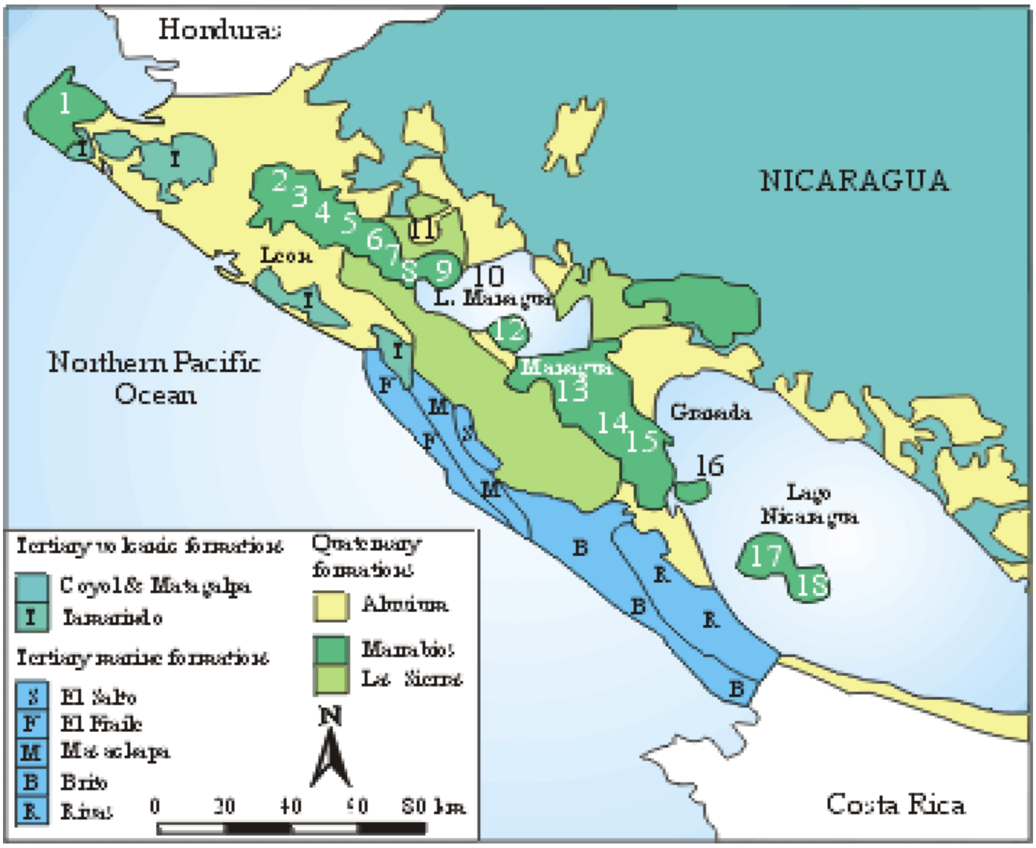

Figure 3.4 Geological map of western Nicaragua (van Wyk de Vries, 1993). Volcanoes: 1. Cosigüina, 2. San Cristobal, 3. Casita, 4. La Pelona, 5. Telica, 6. Rota, 7. El Hoyo, 8. Monte Galan, 9. Momotombo, 10. Momotombito, 11. Malpaisillo caldera, 12. Chiltepe, 13. Masaya/Las Sierras, 14. Apoyo, 15. Mombacho, 16. Zapatera, 17. Concepción, 18. Maderas.

2. **The Nicaraguan depression** is filled with quaternary volcanic deposits originating from the active volcanic chain running through it. The volcanic rocks are divided into two major groups: the Marrabios and Las Sierras formations. Below the quaternary deposits there is a basement of tertiary origin. The Nicaraguan Depression is described further in chapter 3.1.3.

3. **The Interior Highlands** has a Palaeozoic metamorphic basement. Except for the northern part of the area limiting to Honduras the metamorphic rock is covered by tertiary volcanic rocks. These originate from ancient volcanic fields in El Salvador, Guatemala and Honduras. The tertiary rock has then been overprinted by later ignimbrite eruptions. The El Coyol group bordering the Nicaraguan depression from Honduras to Costa Rica is one of the groups consisting of tertiary volcanic rock. The El Coyol rock also outcrops on the Solentiname and Puerto Diaz Islands in Lake Nicaragua and around Telica in the northwestern part of the Nicaraguan depression.

4. **The Atlantic Coastal Plain** is mostly alluvium from Miocene to quaternary origin.

3.1.3 The Nicaraguan Depression

The Nicaraguan depression runs through the length of Nicaragua along the pacific coast. It is filled with quaternary volcanic deposits created by eruptions from the active volcanoes running through it.

3.1.3.1 The volcanic chain

The volcanic chain begins at the Cosigüina volcano (1)[1] forming a peninsula in the northwest of Nicaragua. It is formed over an earlier quaternary volcanic centre, which in turn lies over tertiary volcanics and sediments.
The chain continues with the Cordillera Marrabios ranging from the San Cristobal volcano to the Momotombito volcano (2 to 10). From El Hoyo to Momotombito (7 to 10) the volcanoes are built on the ignimbrites of the Malpaisillo caldera (11), forming part of the Las Sierras group.
Further southwest the Chiltepe volcano (12) and the Nejapa alignment formed by the Masaya, Apoyo and Mombacho (13, 14 and 15) volcanoes lies on the Las Sierras ignimbrites, erupted from the Las Sierras caldera surrounding the Masaya volcano (13).
In Lake Managua lie the last three volcanoes of the volcanic front before entering in Costa Rica: Zapatera, Concepción and Maderas (16, 17 and 18).
Between the volcanoes sequences of alluvium and lacustrine sediment interlayer with tephra deposits (van Wyk de Vries, 1993).
The thickness of the quaternary rock is not accurately determined, but given that the tertiary basement outcrops at several locations within the Nicaragua depression it probably constitutes only a thin layer (van Wyk de Vries, 1993).
The Central American Volcanic Chain is segmented by zones of transverse faulting. These zones contain volcanoes with a tendency for explosive eruptions (van Wyk de Vries, 1993). One of the zones of transverse faulting cuts right through Managua (see Figure 2.8) and constitutes the main seismic source in the area.

[1] Numbers in parenthesis refers to the map in Figure 3.4.

3.1.3.2 The origin of the depression

The origin of the Nicaraguan depression is a subject of debate. It has been interpreted as a graben formed by coast-parallel strike-slip faulting in The Mateare fault zone, running along the north-eastern side of the Las Sierras hills, and the fault zone at the northeast depression boundary at Cuesta Coyol (as seen in Figure 2.8). These fracture zones are believed to be the result of the Cocos plate flexing the edge of the Caribbean plate with its unceasing pressure (Incer Barquero et al., 2000).

Van Wyk de Vries (van Wyk de Vries, 1993) however, argues that the adjacent fault zones cannot have caused a graben structure. The Mateare fault zone is only continuous for about 30 km. Furthermore the strata in the Las Sierras hills dip radially from an axis located in the Masaya Caldera, not westwards as would be expected if having caused the depression.

On the other hand the fault zone at Cuesta Coyol, forming the north-eastern boundary of the depression is a series of faults dipping toward the depression. However they are covered by undeformed Quaternary Las Sierras ignimbrites, indicating that they have not moved in the Quaternary period.

The alternative explanation suggested by van Wyk de Vries is that the land has sunk due to isostatic readjustment. This would be due to the massive deposition of volcanic material in the Interior Highlands during the Tertiary period. The thicker crust in the Interior Highlands would then cause isostatic readjustment of surrounding regions.

3.2 Stratigraphy in Managua

Managua is located on land sloping from the Cordillera de Pacifico down to Lake Xolotlán (Figure 3.5).

All cenozoic formations in the Managua area are of volcanic origin. The basement is a pyroclastic sequence called the Las Sierras group. Las Sierras is covered by deposits from recent volcanic activity.

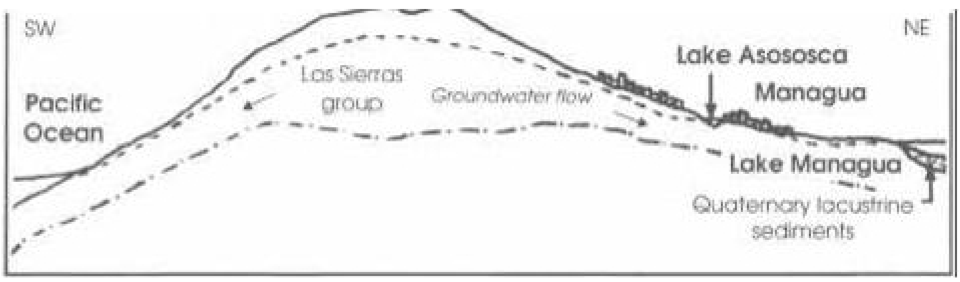

Figure 3.5 Cross-section of the geological structures near Managua (Anton, 1996).

3.2.1 The basement

The basement consists of the volcanic tuff of the upper Las Sierras group, locally known as "cantera". Tuff is consolidated pyroclastic materials from volcanic eruptions. It dates from early quaternary volcanism. Although in a geological context the Las Sierras Group forms the rock basement, geophysical studies have placed the halfspace at a depth varying between 2 and 9 meters (Ekholm and Norberg, 1998). This is because in earthquake engineering materials with a shear wave velocity above 700 m/s are considered basement.

In fact the stiffness of the soil increases gradually with depth and a clearly marked border between the basement and surface layers is not easily found.

3.2.2 The surface layers

The Las Sierras basement is covered by pyroclastic materials from the Holocene volcanism of the Central American Volcanic Front, interlayered by organic soils deposited in between the eruptions. The soils can be classified as mainly non-cohesive silt, sand and gravel with varying degree of consolidation and cementation (Ekholm and Norberg, 1998). Generally they have high porosity and low density.

The layers are well defined, but vary in thickness and compactation degree between different locations in Managua. There can be big differences even between sites very close to one another (Parrales Espinoza and Picado Romero, 2001). Figure 3.6 shows the stratigraphy but the depths are only examples as they can vary between sites. The following information on the layers is based on (Ekholm and Norberg, 1998).

The Retiro tuff is a layer of indurated, fine grained basaltic tuff.

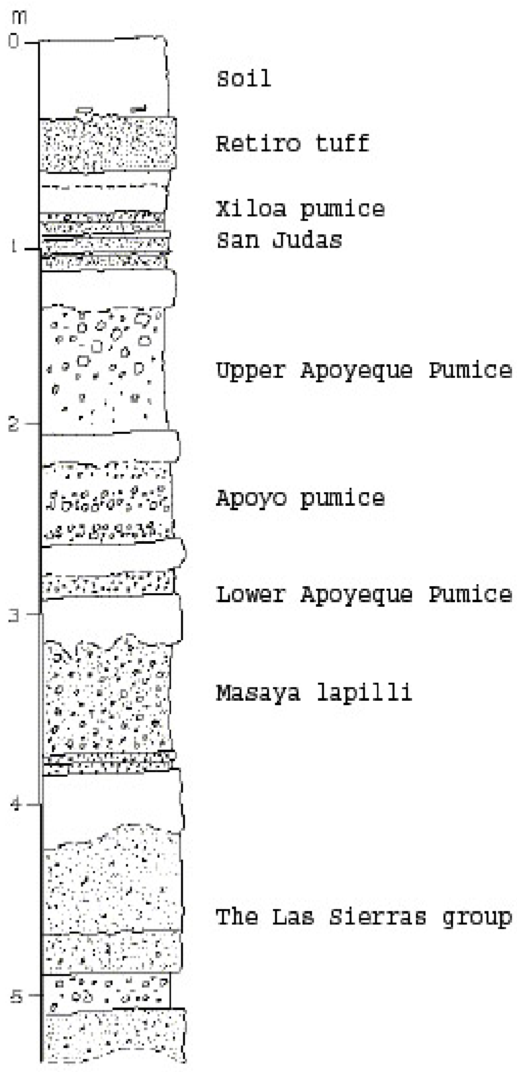

Figure 3.6 Typical stratigraphic column below Managua (Parrales Espinoza and Picado Romero, 2001)

The San Judas formation is a triple layer of indurated tuff, with lapilli and basaltic ash in between layers.

The Apoyeque pumice is pumice erupted from the Apoyeque volcano during the Holocene and late Pleistocene.

The Masaya lapilli is uncemented basaltic lapilli with contents of sand- and silt-sized ash, with origin from the activity of the Masaya volcano. Lapilli is gravel of concentrical spheres formed when the material from a volcano flies through the air.

The surface layers of Managua seem to be composed by stiff sequences interspersed between more compliant sequences. This will mean a stiffer over all behaviour, perhaps similar to that of steel laminated rubber used as attenuators in for example bridges. Compliant soil laminated by stiff soil would certainly result in less deformability than a homogenously compliant soil.

Figure 3.7 In this cut by the side of the road the layered structure can clearly be seen.

4 Site response

The purpose of the Spectrogram Evaluation Technique is to evaluate the site response in the case of an earthquake. In the passage through surface layers the seismic waves emitted from the earthquake will change their characteristics. Wave amplitudes may grow and cause a more destructive kind of movement than if they were transmitted directly through rock.
In the 1972 earthquake the most severe damages were seen in the city centre. The centre of the city was practically demolished (Figure 4.1).

Figure 4.1 Air foto from 1972 of the demolished city centre.

The intensities experienced by different parts of Managua can be seen in Figure 4.2. Marked in the figure is also the location of the accelerograph whose recordings are used for the risk evaluation later in this work.
High intensities were of course experienced over the Tiscapa fault where the rupture occurred, but another high intensity zone is seen right in the city centre, to the west of the fault. This may be due to the site response of the surface sediments.
The dynamic interaction between seismic waves, rock and soil will be clarified in this chapter. First the fundamental wave dynamics is treated, then the soil's dynamic properties, and finally the interaction between the two to create the resulting site response.

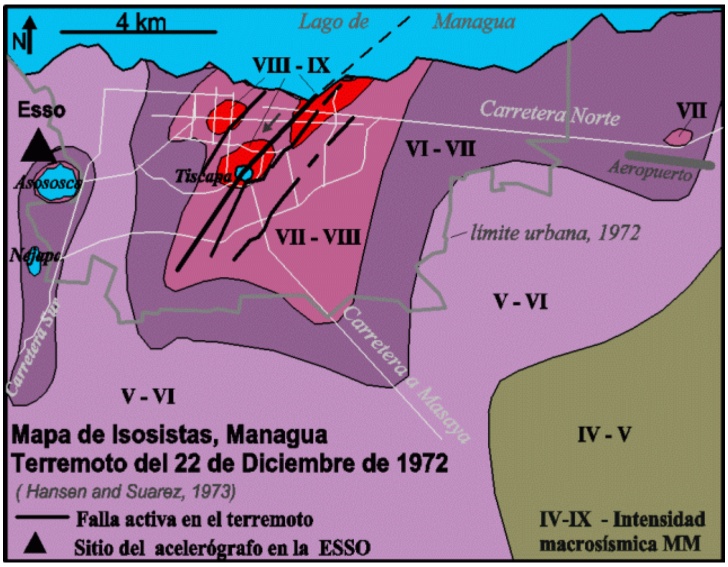

Figure 4.2 Intensities experienced in different parts of Managua in the 1972 earthquake.

4.1 Seismic wave propagation

The seismic waves propagate through an infinite space as body waves and through a semi-infinite space also as surface waves. That is, only close to a surface or an interface between two media the surface waves exist. It is important to remember that none of these waves implies the transport of matter. A wave is merely a propagating oscillation.

4.1.1 Body waves

When waves travel through an infinite space they propagate by means of compressional and dilatational forces or shear forces.

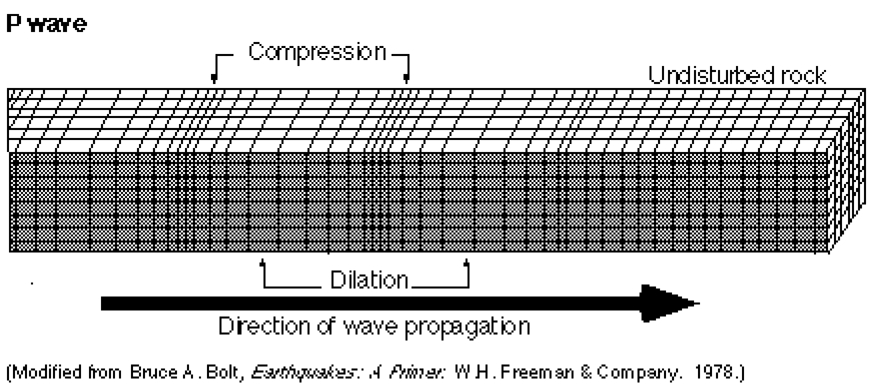

Figure 4.3 The P-wave (Anderson, 1998).

The compressional or longitudinal wave is a pressure wave that propagates through the elastic media. The particles oscillate longitudinally back and forth, with periodic compressions and dilatations as a result (Figure 4.3).
The compression wave has the highest propagation velocity and is therefore termed Primary wave or P-wave, as it arrives first at an observation point at a certain distance from the seismic source.
In the shear wave the particles oscillate transversely to the direction of propagation and transmit the movement by means of shear forces between one another (Figure 4.4). This implies that the shear wave does not exist in liquids or gasses because of them being unable to transmit shear forces. Shear waves are much slower than the compressional wave and therefore termed Secondary waves or S-waves.

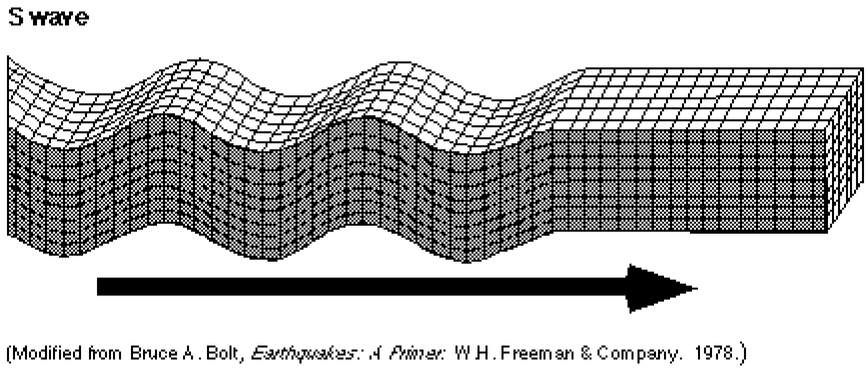

Figure 4.4 The S-wave (Anderson, 1998).

4.1.2 Surface waves

The surface waves occur in the surface of a material and are of two types. The Rayleigh wave travels along the surface of a material and it penetrates to a depth of about one wavelength. It propagates with an elliptical retrograde (counter-clockwise) particle motion (Figure 4.5). The velocity of the Rayleigh wave varies depending on the Poisson ratio between $0,92*V_S$ and $0.95*V_S$ (Richart et al., 1970). It is very similar to a water wave, except that a water wave propagates with a prograde elliptical particle motion.
The other type is the Love wave which occurs when a low velocity layer lies over a high velocity half space. Because of multiple reflections the layer acts as a waveguide retaining horizontal shear waves within the surface layer and creating a transverse rocking motion of the surface (Figure 4.6). It is slightly faster than the Rayleigh wave and has a velocity close to the S-wave velocity.
Surface waves are the result of interaction between P- and S-waves near the surface and do not represent physical waveforms but rather propagation modes.

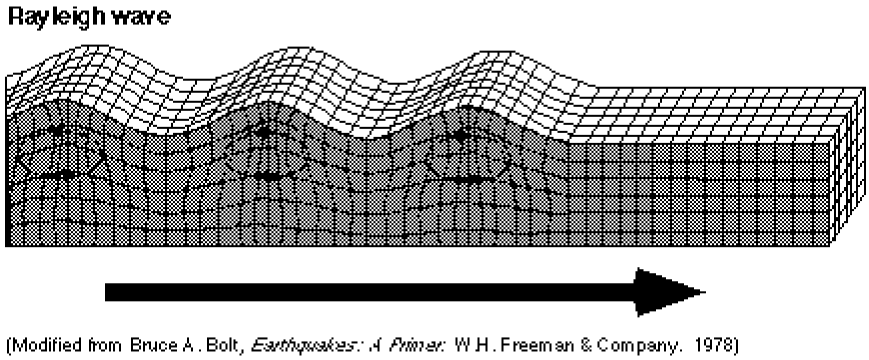

Figure 4.5 The Rayleigh wave (Anderson, 1998)

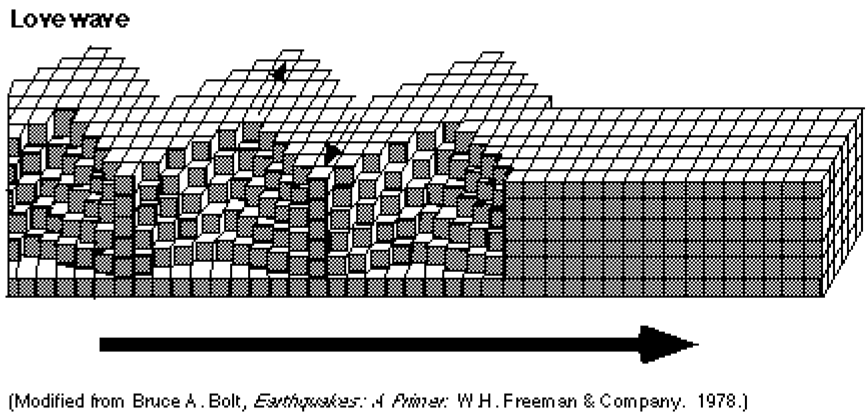

Figure 4.6 The Love wave (Anderson, 1998).

4.1.3 Passage from earthquake focus to surface

The energy released in the elastic rebound of a fault will be spread in all directions from the focal point in the form of seismic shockwaves. The seismic waves will propagate in the form of P-waves, S-waves and surface waves.

As the P-waves are the fastest they will be the first to arrive. Then comes a relatively quiet period leading up to the arrival of the S-wave and after that the surface waves arrive. The arrivals of the P-wave and the S-wave are referred to as the minor tremor while the arrival of the surface waves is called the major tremor (Figure 4.7). The major tremor is often the one creating the most extreme ground movements at the site.

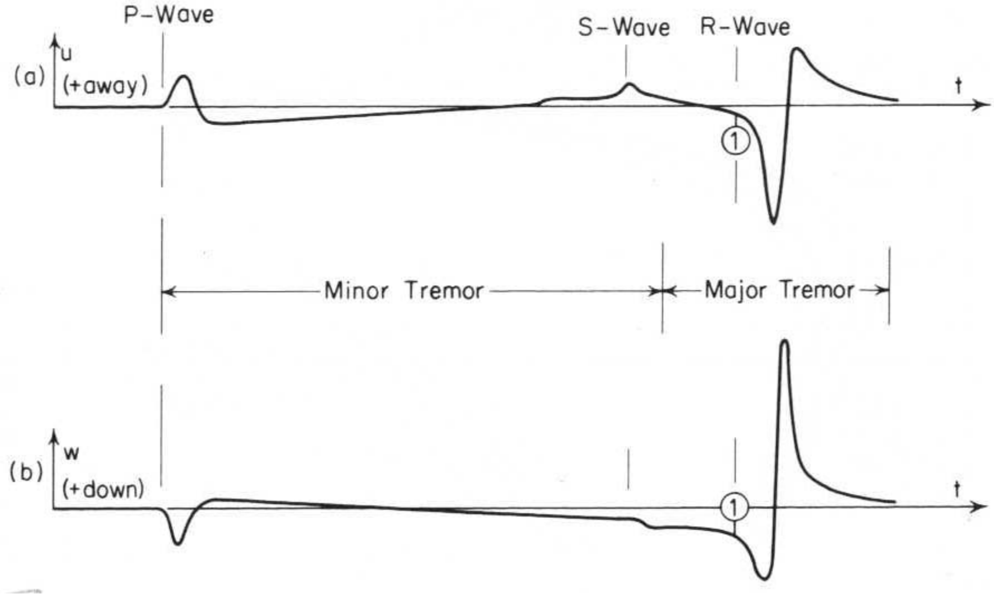

Figure 4.7 Arrival of the P-wave, S-wave and Rayleigh wave. (a) The horizontal motion and (b) the vertical motion (Richart et al., 1970).

As the seismic waves pass through the crust the high-frequency components will be damped to a higher degree than the low-frequency components and thus filtered out. The body waves are attenuated in proportion to 1/r, while the Rayleigh wave is attenuated in proportion to $1/\sqrt{r}$. Thus, being far from the focus of an earthquake, it is often the long-period Rayleigh waves that are most destructive at the site. On the other hand, in Managua, the most destructive earthquakes have occurred at shallow depth below or close to the city. Such earthquakes could result in a considerable part of short-period vibrations as well, originating from body waves.
The waves will pass through the crust and on through the surface layers where their characteristics will change (see paragraph 4.3.1). If the earthquake focus is close and the seismic waves travel through surface layers it could mean the amplification of short-period waves. The result would be short-period waves with large amplitudes, which could reveal itself very destructive.

4.1.4 Determination of earthquake epicentre

The epicentre is the earthquake focus projected to the surface. That is, the point on the surface directly above the focus. With a single seismograph registering the arrivals of the P- and S-waves from the earthquake focus, it is possible to determine the distance from seismograph to epicentre. Given that the velocities of the P- and S-waves through the crust are known, the time elapsed between the arrival of the P-wave and the S-wave will give the distance to the earthquake epicentre.
Having the data from two seismographs at different locations it is possible to narrow down to two points where the earthquake could have occurred. With three seismographs located at different sites it is possible to pinpoint where the earthquake

took place. Where the three circles drawn with the source distance as radii all coincide, is the epicentre of the earthquake.

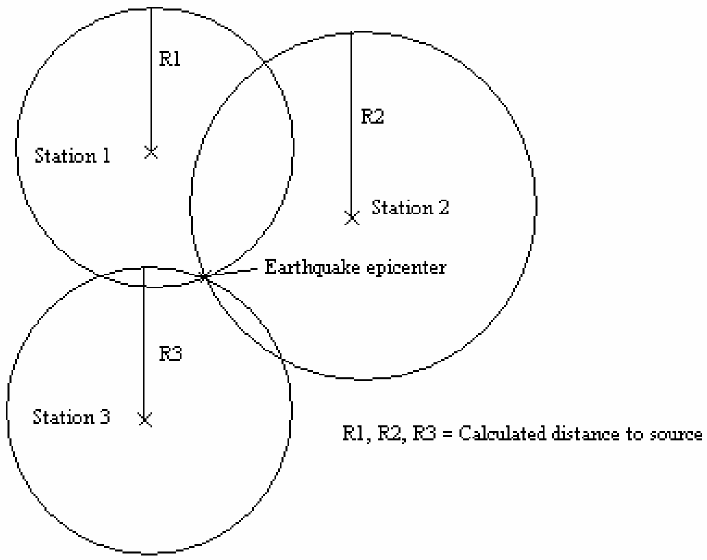

Figure 4.8 Pinpointing the earthquake epicentre.

4.2 Dynamic properties of soil

4.2.1 Soil properties and wave propagation velocity

The propagation velocity of a wave depends on the soil material parameters such as the Young´s modulus, the shear modulus and the Poisson ratio. They are all related parameters.

The Young's modulus E describes the elastic properties of a material when subjected to a compressive or tensile force. It is defined as the ratio of normal stress to normal strain.

The shear modulus G describes the elastic properties of the soil under the action of a transversal internal force. It is defined as the ratio of shear stress to shear strain. The shear modulus is related to the Young's modulus by

$$G = \frac{E}{2(1+\nu)} \qquad (4.1)$$

where the Poisson ratio ν is the rate of transverse contraction strain as a response to longitudinal extension strain. It is defined as the ratio of transversal strain to longitudinal strain.

The P- and S-wave velocities depend on the shear modulus and the Poisson ratio as follows:

$$V_p = \sqrt{\frac{G(2-2\nu)}{\rho(1-2\nu)}} \tag{4.2}$$

$$V_s = \sqrt{\frac{G}{\rho}} \tag{4.3}$$

How the equations (4.2) and (4.3) are derived from the equations of motion can be seen in (Richart et al., 1970). Because of the relation between Young's modulus and shear modulus in (4.1), equations (4.2) and (4.3) can be written:

$$V_p = \sqrt{\frac{(1-\nu)E_{dyn}}{(1+\nu)(1-2\nu)\rho}} \tag{4.4}$$

and:

$$V_s = \sqrt{\frac{E_{dyn}}{(1+\nu)2\rho}} \tag{4.5}$$

From these equations an expression for calculating the Poisson ratio can be derived:

$$\frac{V_P}{V_S} = \sqrt{\frac{1-\nu}{\frac{1}{2}-\nu}} \Rightarrow \nu = \frac{\left(\frac{V_P}{V_S}\right)^2 - 2}{2\left(\left(\frac{V_P}{V_S}\right)^2 - 1\right)} \tag{4.6}$$

Thus the ratio between P- and S-wave velocities is strictly determined by the Poisson ratio of the material. Knowing the P- and S-wave velocity the material's shear modulus, Young's modulus and Poisson ratio can be determined from equations (4.2), (4.3), (4.4), (4.5) and (4.6). Alternatively knowing the Poisson ratio and Young's modulus or shear modulus, the S- and P-wave velocities can be determined.

4.2.2 Impedance

The impedance of the soil can be compared with the stiffness of a spring. If mounting two springs with different spring constants to each other and compressing them, the one with the lower constant will have to deform more in order to balance the force exerted by the other.

The same goes for the passage of a wave from a stiff material to a compliant material. When the wave motion in the stiff material exerts its force on the compliant material, the compliant material will have to deform more in order to balance the force. It follows that wave amplitudes will grow as the medium deforms more.
The impedance is defined as the product between material density ρ and the wave velocity V in the material.

$$Z = \rho \times V \tag{4.7}$$

When a wave encounters a boundary which is neither completely rigid nor free, some of the wave will be reflected and part will be transmitted across the boundary. The amplitudes of the reflected and transmitted waves are determined as a function of the impedance change.

$$A_r = \frac{z_1 / z_2 - 1}{z_1 / z_2 + 1} \cdot A_0 \qquad A_t = \frac{2}{1 + z_2 / z_1} \cdot A_0 \tag{4.8}$$

The sum of the reflected and transmitted amplitudes can thus be higher than the original wave amplitude. This is due to the greater deformability of the low impedance material.

4.2.3 Attenuation

The wave amplitude decreases as the wave train propagate through an elastic medium. This attenuation takes place in the form of geometrical and material damping.
As the wave front propagates from the source the energy has to spread over a wider area and thus the amplitude decreases with an increased distance from the source. This is known as geometrical damping.
Material damping is caused by energy dissipated and transformed into heat within the soil skeleton. For cohesionless soil the dominating mechanisms of energy dissipation is the friction between particles and fluid flow losses because of the relative movement between the solid and the fluid phases (Rix et al., 2000).
Material damping causes the cyclic stress-strain curve to exhibit a hysteretic loop as shown in Figure 4.9.

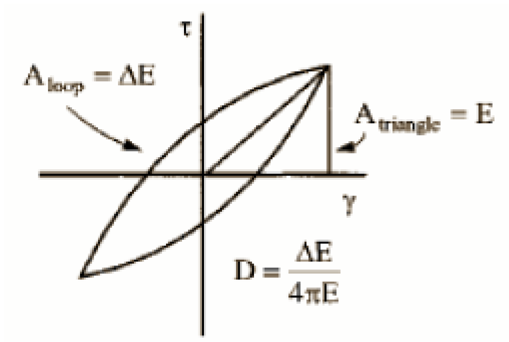

Figure 4.9 Cyclic stress-strain curve (Rix et al., 2000)

There exist many damping descriptors. The parameter traditionally used in geotechnical engineering is the *material damping ratio D.* It is defined as

$$D = \frac{\Delta E}{4\pi E} \tag{4.9}$$

Where ΔE is the energy dissipated during one cycle at the angular frequency ω and E is the maximum strain energy stored during the cycle. The dissipated energy ΔE is the area enclosed by the loop in Figure 4.9 and the stored energy E is the area of the triangle shown.

Seismologists often use the *quality factor Q*, by Knopoff called the “specific attenuation factor”, to describe attenuation. Its inverse is termed dissipation factor and defined as:

$$Q^{-1} = \frac{\Delta E}{2\pi E} = 2D \tag{4.10}$$

The damping ratio D is generally frequency dependent, but experiments have shown that it can be considered frequency independent for 0.1 < f < 10 Hz (Rix et al., 2000).

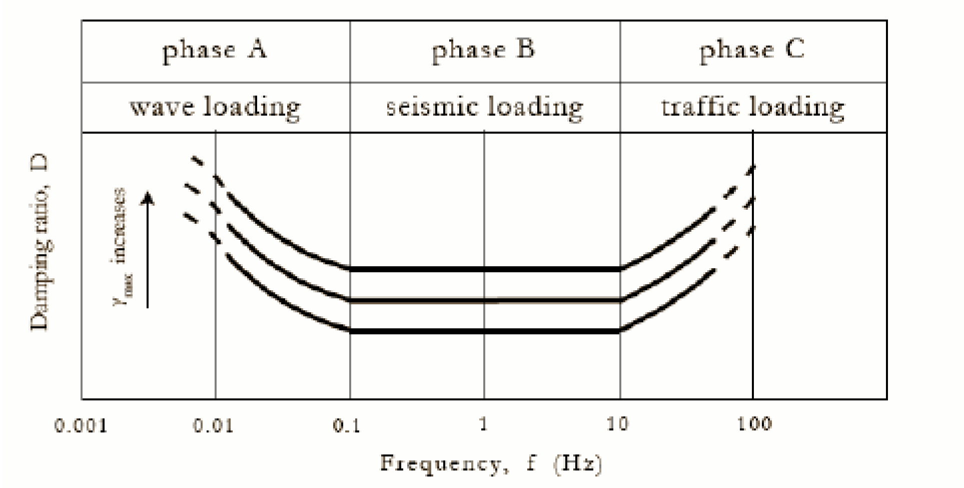

Figure 4.10 Frequency dependence of damping in soil (Rix et al., 2000).

Other measures of damping are the *attenuation coefficient α* and the *logarithmic decrement δ*.
They are related to the damping ratio by the expression

$$D = \frac{\alpha v}{\omega - \frac{v^2}{\omega}} = \frac{\delta}{2\pi} \frac{1}{\sqrt{1 + \left(\frac{\delta}{2\pi}\right)^2}} \tag{4.11}$$

where v is the seismic velocity and ω is the angular frequency. For small values of damping (D<10%) the second order terms become very small and can be ignored which results in the expression (Rix et al., 2000):

$$D = \frac{\alpha v}{\omega} = \frac{\delta}{2\pi} \tag{4.12}$$

If the seismic oscillation is in the linear domain of elasticity the attenuation of a harmonic signal is exponential. It may then be described as a *logarithmic decrement δ*. That is assuming that the decay is similar to that predicted by the theory for viscously damped free vibrations, although soils do not have a viscous behaviour (Richart et al., 1970). It is defined as the natural logarithm of two successive amplitudes of motion z_1 and z_2.

$$\delta = \ln \frac{z_1}{z_2} = \frac{2\pi D}{\sqrt{1-D^2}} \tag{4.13}$$

The logarithmic decrement is obtained experimentally, for example from the resonant column test. It sets a soil sample into steady-state forced vibration. When shutting off the driving power the decay of the amplitude with time is recorded.

The *attenuation coefficient α* measures the energy loss as a function of distance (Richart et al., 1970). For small damping values it is related to the logarithmic decrement by

$$\delta = \frac{2\pi v \alpha}{\omega} = L\alpha \tag{4.14}$$

where L is the wavelength, and to the dissipation factor by

$$Q^{-1} = \frac{2v\alpha}{\omega} \tag{4.15}$$

as can be seen from equation (4.12).

For modal damping based on frequency response it comes natural to measure the half-power bandwidth. In this method the width of the dynamic response curve around the resonance peak is measured. For small values the quality factor can be defined from the bandwidth by

$$Q = \frac{f_r}{(f_2 - f_1)} \tag{4.16}$$

where f is the resonance frequency and f_1 and f_2 are the frequencies at which the power has dropped to half of its peak value (Parrales Espinoza, 2004). That is when the amplitude is 0.707 times the amplitude at the resonance frequency (Figure 4.11). This is done for example with a resonant column or an impulse response test.

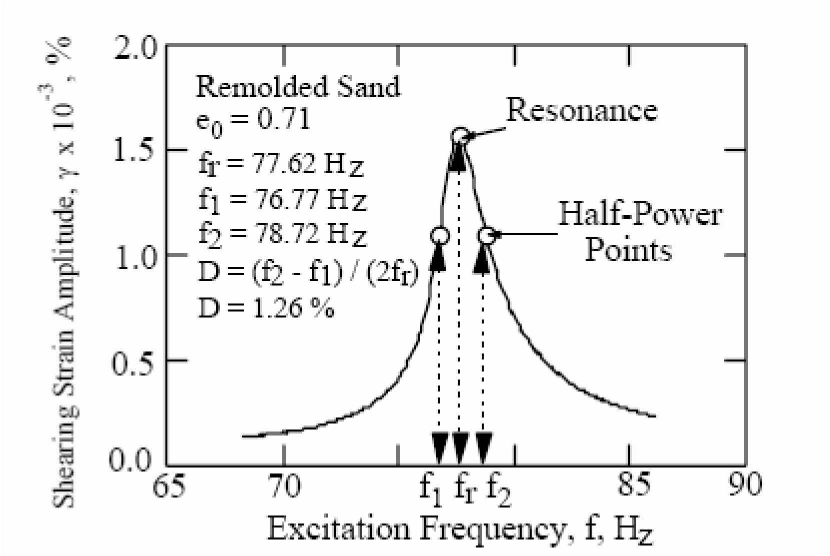

Figure 4.11 Damping measurement on sand using the half-power bandwidth method (Rix et al., 2000).

It follows from the relation between the quality factor and damping ratio (equation (4.10)) that the damping ratio is given from the bandwidth by

$$D = \frac{(f_2 - f_1)}{2f_r} \tag{4.17}$$

The material damping is a reducing factor counteracting the amplification caused by impedance changes and resonance effects in the surface layers. It is therefore highly interesting when talking about seismic risk.

4.3 Site effects

The seismic waves emitted from the earthquake focus are filtered by the different geological materials through which it passes. The superficial sediments at the site is the geological entity which can affect the frequency content and amplitudes the most and determine what kind of vibration will be felt on the site. The site effects include amplification of wave amplitudes through impedance change and resonance effects, but also positive effects that renders the site less earthquake-sensitive, like attenuation.

4.3.1 Amplification in surface layers

It has long been known that surface layers can amplify ground motion relative to bedrock. The amplification of a wave train passing through surface layers depends on various factors like the thickness of surface layers, the impedance contrast and the material damping.

Soil deposits will tend to amplify some components of ground motion and attenuate others. The strongest amplified components will be those at or near the characteristic frequency of the site. This characteristic frequency is a function of the stiffness and thickness of the soil deposit.

The contrast in impedance between geological materials causes the wave amplitudes to grow (see chapter 4.2.2) due to the condition of conservation of energy. The passage of a wave train from a stiff medium like rock with a high shear modulus, to a compliant medium like soil with a low shear modulus amplifies especially the S-wave. But also a stiff soil can increase the earthquake sensitivity of a site. If the earthquake focus lies close to the site, a compliant soil can have the effect of damping the acceleration felt on the surface. Instead a stiff soil would permit more of the earthquake energy to reach the site with stronger surface acceleration as a result.

4.3.2 Resonance

Resonance effects can occur where abrupt impedance contrast exists. Every soil profile has several resonant frequencies with different displacement modes.

The fundamental resonance frequency (marked as 1 in Figure 4.12) occurs when the wavelength is equal to four times the thickness of the soil deposit. Thus it can be calculated like:

$$f_r = \frac{v(2n-1)}{4h} \qquad (4.18)$$

where v is the velocity of the wave, h is the thickness of the soil deposit and n is the mode number. This is valid for a homogenous deposit with constant velocity.

Usually the surface sediments consist of various layers of different geological materials, as is the case of Managua, and

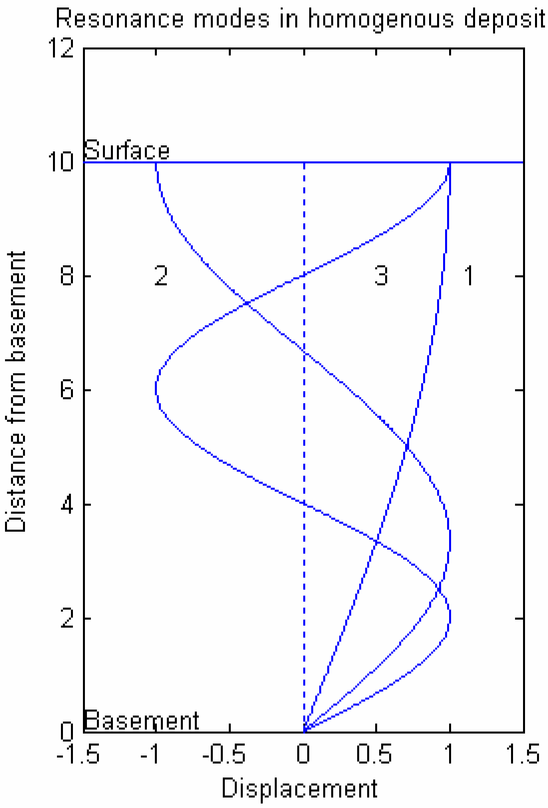

Figure 4.12 The first three resonance modes in a homogenous soil deposit. The maximum displacement is set to one.

therefore the picture becomes more complex. The thickness of the surface layers also varies from site to site.
Analytical solutions for resonance frequencies and modes in soil deposits with varying velocity gradient can be found in (Gazetas, 1982).

A rough estimate of the fundamental resonance frequency for structures as a function of the number of stories N is given by (Stål and Westberg, 1996):

$$f_r = \frac{10}{N} \tag{4.19}$$

If the basement vibrates at the same frequency for which there is resonance in the soil, energy will be pumped into the soil layers for each new oscillation of the basement. If in combination with this there is a low soil attenuation the result can be a build-up in vibration amplitudes for the duration of the earthquake. A building with a resonance frequency within the dominating frequency band of the resulting surface motion can further amplify the acceleration the structure is exposed to.

4.3.3 Nonlinear soil behaviour

At large strains the soil begins to yield and the site response enters into the nonlinear domain. This means that the damping will increase and reduce the surface layer amplification. Thus the surface layer amplification may be overestimated in the strong ground motion produced by larger earthquakes. Nonlinear soil behaviour can also create a shift in resonance frequencies.
The linear elastic behaviour is only an approximation, even at low strains. The question is at what point nonlinearity becomes important.
(Knopoff, 1964) claims that except for nonlinear behaviour near earthquake foci, seismic strains are small and seismic oscillations take place in the linear domain of elasticity. Experiments show that nonlinearity starts at strains in excess of 10^{-5} or 10^{-6}.
This indicates that the attenuation mechanism in solids is not the same as for liquids, where the attenuation factor varies as the square of frequency. In solids the attenuation factor varies as the first power of frequency.
There is however uncertainty as to whether the degree of amplification varies with the level of input motion. (Field et al., 1997) reports that ground motion amplification in the main shock of the 1994 Northridge earthquake was up to a factor two less than in the aftershocks and that resonance that were clear in the weak motion were absent in the strong motion.
As the level of strain increases a systematic shift in resonance peaks toward lower frequencies takes place. It may even bifurcate into two lower amplitude peaks, with a third peak growing up at a lower frequency. These effects originates in interaction between frequency components which shifts the energy distribution across the spectrum (Field et al.).

4.3.4 Dangerous ground motion

The collapse of a structure occurs when the carrying elements in it fails. This frequently happens when the weight of the structure acts outside the paths it is designed for. That is why especially horizontal or rocking oscillations are considered when evaluating the vulnerability of sites. These oscillations cause the displacements that make the structure's weight act outside the normal load distribution paths.
However, also vertical oscillation can cause dynamic loads that cause structure collapse, and should be accounted for. In the case of Managua, where earthquakes frequently occur at shallow depth close to or under the city, powerful vertical oscillations that can damage buildings are likely to occur.

5 Methodology

The Spectrogram Evaluation Technique utilizes the impulse response and its attenuation as a method to identify resonance frequencies inherent in the soil strata. Heavy vehicles are used to create a wide-band frequency impulse into the ground. In the ground response from the impact the acceleration will prevail at resonance frequencies.
The ground acceleration is measured with a combination of two sensors. These are a tri-axial accelerograph and a uni-axial accelerometer-A/D converter acquisition system. An original plan was to use a tri-axial accelerometer connected to a Geode recorder, but troubles were encountered with the DC-input in the connection. When it was discovered at arrival in Managua that CIGEO is the owner of a K2 tri-axial accelerograph the decision was made to use it instead as it provides three-component information of acceleration without connecting to any other apparatus than the laptop. The uni-axial accelerometer-A/D converter acquisition system is used as comparison because, if it provides viable results and the additional information from the K2 accelerograph proves redundant, measurements with a uni-axial accelerometer are cheaper and faster. Furthermore it provides higher resolution and has a wider bandwidth, although it doesn't reach as low down in the frequencies as the K2 accelerograph.

First in this chapter the Nakamura technique will be looked into as the method widely used to identify resonance frequencies and to evaluate the transfer function in surface layers. Then in section 5.2 the traffic impulse response used in the spectrogram evaluation technique will be discussed. In section 5.3 the field work procedures and strategy are treated, and in section 5.4 the data processing methods used for evaluation of the acquired data are explained. Finally, in section 5.5, the time-frequency hazard analysis, developed for this study for an objective evaluation of site response data, is explained.

5.1 The Nakamura technique

Nakamura's technique is a method that uses microtremors in the evaluation of surface layer amplification. It produces the fundamental frequency and the transfer function in the surface layers.
The method introduced by Nakamura in 1989 uses a single three-component accelerometer. The amplification of the soil can be calculated as the ratio between the vertical and horizontal frequency spectra as will be shown. The fundamental resonance frequency is where the amplification is strongest and thus where a peak can be seen in the H/V-ratio.
The theory of the technique presented here is taken from his paper (Nakamura, 2000) and the masters thesis of (Stål and Westberg, 1996).

5.1.1 Nakamura's theory

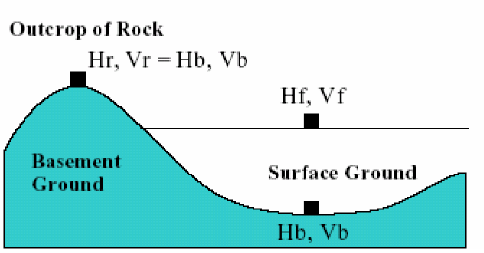

Figure 5.1 A sedimentary basin with vertical (V) and horizontal (H) wave amplitudes at basement (b), surface (f) and outcropping rock (r) (Nakamura, 2000).

The amplification of a wave train passing through the surface sedimentary layers can be written as the ratio between the wave amplitude at the surface and the amplitude at the rock basement.

If an accelerometer were to be placed at the surface and another at the level of the rock basement, the amplification could be estimated from the ratio of amplitudes. This can be done in a borehole and would be the most accurate method, however costly and time-consuming. It can also be done by comparing to an outcropping rock reference site if available, where the wave amplitudes can be said to represent those at the basement (Figure 5.1). The Nakamura technique offers a less complicated method.

The transfer function of the surface layers is defined by:

$$S_T = \frac{S_{HS}}{S_{HB}} \qquad (5.1)$$

Where S_{HS} is the spectra of horizontal motion at the surface and S_{HB} is the spectra of horizontal motion at the basement.

The S_{HS} spectra may be affected by surface waves as it is measured at the surface. Artificial noise is mostly propagated as Rayleigh waves. The content of Rayleigh waves can be removed from S_{HS} by introducing a correction factor.
Nakamura assumes that the vertical motion is not amplified by the surface layers, the nature of this assumption will be treated in paragraph 5.1.2.
Because the vertical motion is not amplified by the surface layers the effect of the Rayleigh wave can be seen by comparing the vertical motion at the surface with the vertical motion at the basement. Any extra frequency content that the surface vertical motion has with respect to the vertical basement motion would be due to Rayleigh waves. The ratio E_S gives the effect of Rayleigh waves on vertical motion.

$$E_S = \frac{S_{VS}}{S_{VB}} \qquad (5.2)$$

It is also assumed that the effect of Rayleigh waves is equal in vertical and horizontal components. Then the transfer function can be corrected by dividing it with the ratio E_S of Rayleigh wave effect.

$$S_{TT} = \frac{S_T}{E_S} \tag{5.3}$$

Inserting equations (5.1) and (5.2) into equation (5.3) we get:

$$S_{TT} = \frac{S_T}{E_S} = \frac{S_{HS}}{S_{HB}} \cdot \frac{S_{VB}}{S_{VS}} = \frac{S_{HS}}{S_{VS}} \cdot \frac{S_{VB}}{S_{HB}} \tag{5.4}$$

As the vertical and horizontal wave amplitudes are assumed to be nearly equal at the basement, and thus $\frac{S_{VB}}{S_{HB}} \to 1$, we are left with:

$$S_{TT} = \frac{S_{HS}}{S_{VS}} \tag{5.5}$$

which Nakamura calls the Quasi-Transfer Spectrum. It gives the amplification of horizontal motion in surface layers. In practice it is determined from tri-axial recordings as the resultant of the horizontal component amplitude spectra divided by the vertical component power spectrum (Teves Costa and Matias, 1995):

$$S_{TT} = \frac{\sqrt{NS(\omega)^2 + EW(\omega)^2}}{Z(\omega)} \tag{5.6}$$

where *NS* is the amplitude spectrum of the North-South oriented horizontal axis and *EW* is the amplitude spectrum of the East-West oriented horizontal axis.

5.1.2 Amplification of P- and S-waves

Nakamura does the assumption that no amplification of the vertical motion takes place in the surface layers. The theoretical background is not completely clear as to that assumption, but the method has proven to give good results.

As described in paragraph 4.2.2 the impedance change when passing from a stiff to a compliant material will force the waves to increase their amplitude in order to conserve the same amount of energy. The energy is namely proportional to the amplitude squared. This goes for P-waves as well as S-waves, and thus for both vertical and horizontal motion.

The basement can be expected to have a much lower Poisson ratio than the overlying surface layers. The ratio between S- and P-wave velocity is strictly determined by the Poisson ratio by the expression derived from equations (4.4) and (4.5):

$$\frac{V_P}{V_S} = \sqrt{\frac{1-\nu}{\frac{1}{2}-\nu}} \tag{5.7}$$

It can be seen from equation (5.7) that with a decreasing Poisson ratio, the ratio V_P/V_S increases. This implies that in the passage from consolidated basement material to an unconsolidated surface material the P-wave velocity will decrease to less degree than the S-wave velocity. The impedance change for the P-waves will then be smaller than for the S-waves and thus the amplification of the P-wave smaller.
In Managua the basement is volcanic tuff, and the surface layers consist of non-cohesive silt, sand and gravel with varying consolidation degree. Let us consider the passage of a wave train through the border between the Las Sierras group and the Masaya lapilli (see stratigraphy in figure 3.7). As an estimate the Las Sierras group would have a Poisson ratio similar to "lithic tuff from Howard Prairie Dam, Oregon" of 0.11 (Clark, 1966), and the Poisson ratio of lapilli would roughly be in the order of 0.4 (loose to medium sand (Craig, 1997)). The ratio of the P-wave velocity to S-wave velocity is then 1.51 in the tuff and 2.45 in the lapilli according to equation (5.7). That means that the impedance change for the S-wave is a factor 1.6 greater than for the P-wave, with greater amplitude amplification for the S-wave as a result.

Suppose the lapilli has a P-wave velocity of 1000 m/s and an S-wave velocity of 400 m/s (loose sand (Clark,1966)), and that the Las Sierras tuff has a P-wave velocity of 2160 m/s (volcanic tuff, New Zeeland (Clark,1966)) and an S-wave velocity of 1430 m/s (because V_p/V_s is 1.51). Taking the density for "lithic tuff from Howard Prairie Dam, Oregon" (Clark, 1966) on 1450 kg/m^3 and for the lapilli a density of roughly 1000 kg/m^3, the reflected and transmitted amplitudes become, according to the expressions in (4.8):

$$A_{p,r} = 0.52A_0 \quad A_{p,t} = 1.52A_0 \tag{5.8}$$

$$A_{s,r} = 0.68A_0 \quad A_{s,t} = 1.68A_0 \tag{5.9}$$

where the subscript r denotes reflected and t transmitted wave amplitude.
It should be pointed out that these calculated amplitudes are meant to demonstrate the phenomenon of wave amplification due to impedance changes in surface layers. The characteristics of the surface layers in Managua are much more complex with layers of varying impedance as seen in Figure 3.6 in the geology chapter.

In site response analysis generally the horizontal amplification is looked at. In a wave train coming in from below this is analogous to the S-wave, but incident waves from the earthquake can come in from other directions. The horizontal motion represents a more dangerous motion than the vertical for structures founded in the soil as explained in chapter 4.3.4.

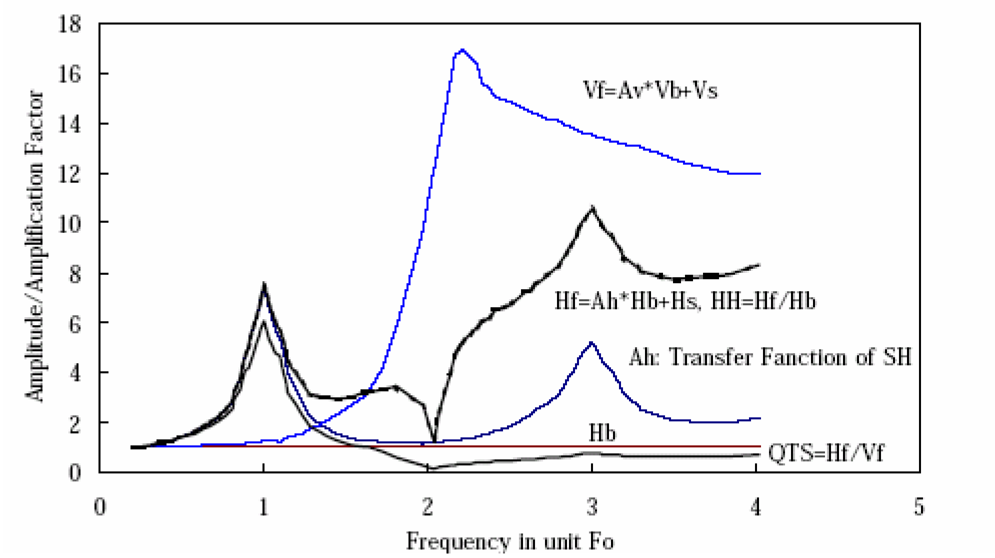

Figure 5.2 Example of vertical (Vf) and horizontal (Hf) acceleration at surface and the horizontal transfer function calculated by comparing them to an outcropping rock reference site. Also Nakamura's spectral ratio (QTS) is shown as comparison (Nakamura, 2000).

Generally it can be seen from the example given in this section that both vertical and horizontal motion can be amplified when passing through surface layers.

The assumption Nakamura makes that the vertical motion remains unchanged when it passes through surface layers should rather be viewed in the context of resonance amplification. As stated in section 4.3.2 the resonance of the P-wave, which is generally associated to vertical motion, occurs at a higher frequency than the resonance of the S-wave, due to its higher velocity.
As can be seen in Figure 5.2 this means that the amplification of vertical motion is close to one at the frequency where S-wave amplification is highest due to resonance.
In fact the Nakamura technique can only be used to estimate the amplification at the fundamental frequency of the surface layers, as the QTS spectral ratio will show no amplification, or even attenuation at the second resonance peak (see Figure 5.2). Of course this is not true. However, the technique is valid because the maximum amplification occurs at the fundamental resonance frequency.

5.2 The traffic impulse response

The idea behind the Spectrogram Evaluation Technique is to develop a method for fast identification of earthquake-sensitive sites. A critical point as to the speed in seismic methods is the kind of source used. Methods using ambient noise like for example the Nakamura technique are easy to use as the seismic sources already exists in the urban ambient. But the required observation times are long relative to the method suggested here.

Figure 5.3 The rear wheel axis of a bus gives a powerful and distinct impact.

In the traffic impulse response approach ambient sources are used to create impacts. The ground response to that impact is then recorded for evaluation.
The seismic source consists of a heavy vehicle crossing an obstacle on the roadway, which creates a downward impulse into the ground. Also a shear impulse polarized in the direction of travel will be generated. The obstacle used in this study is a cable protector of heavy-duty rubber and the vehicle typically would be a truck, trailer truck or a bus, but can be any heavy vehicle. In Managua city buses proved to give a strong and distinct signal due to their rebuilt rear ends (Figure 5.3). The long rear end loads the rear axis heavily, especially when the bus is loaded with people.
Beside the roadway, in a straight line from the obstacle, a tri-axial accelerograph is located to record the vibrations from the impact.

5.2.1 Dwarfing of ambient noise

It is the hypothesis that the vehicle axis passing over the cable protector will create an impact onto the ground strong enough to dwarf the ambient noise. That means that the dominant frequency content of the signal would be the ground response to the actual impact and not to the ambient noise.
It is important that the impact creates strong oscillation amplitudes over a wide band of frequencies, especially in the lower frequencies where earthquakes have their dominant frequency content. The bandwidth and power generated depends on the following properties:

- The stiffness of the road
- The stiffness of the vehicle suspension

- The speed of the vehicle
- The load on the vehicle axis

5.2.2 Waves generated

Figure 5.4 (a) shows the waves generated from the impact on a circular footing. The waves generated from the vehicle impact can be expected to exhibit a similar spreading pattern.

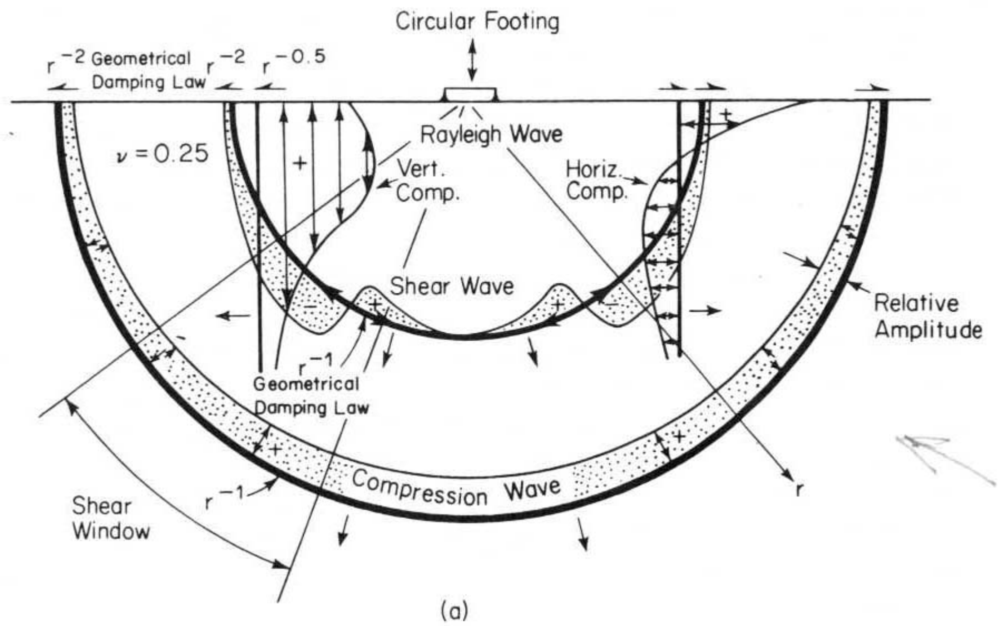

(a)

Wave Type	Per Cent of Total Energy
Rayleigh	67
Shear	26
Compression	7

(b)

Figure 5.4 (a) Waves generated from the impact on a circular footing. The P-wave propagates first in the form of a omni-directional pressurefront. Then comes the S-wave which also propagates along a hemispherical wavefront. Shortly after the S-wave comes the Rayleigh wave propagating in a cylindrical wavefront reaching to the depth of about one wavelength. (b) The percentage of energy spread in the form of P-waves, S-waves and Rayleigh waves (Richart et al., 1970).

The P-wave and S-wave are both spread along a hemispherical wave front, while the Rayleigh wave spread along a cylindrical wave front penetrating to the depth of about its wavelength. The shaded zones along the wave fronts in Figure 5.4 show the particle displacement. The particle motion of the P-wave is a push-pull motion parallel to the direction of propagation and the particle motion of the shear wave is a transverse displacement orthogonal to the direction of propagation. The region of the shear wave front where the largest amplitudes occur is referred to as the shear window. The vertical and horizontal components of the Rayleigh wave vary with the depth as shown in the figure.

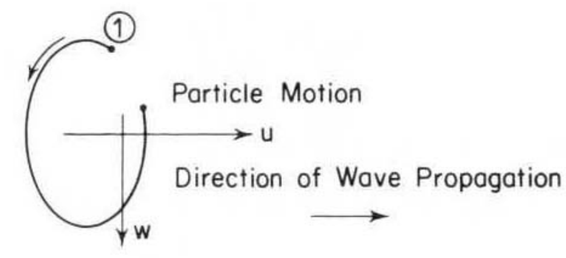

Figure 5.5 The Rayleigh wave particle motion (Richart et al., 1970).

The amplitude of the body waves decreases due to geometrical damping in proportion to 1/r, except for in the surface, where it decreases in proportion to $1/r^2$. The amplitude of the Rayleigh wave decreases in proportion to $1/\sqrt{r}$.

When the wheel pair passes over the obstacle it will create both forces in the direction of travel and downwards into the ground. As the wheels first hit the cable protector, it will create an impulse with a horizontal component in the direction of travel and a vertical component into the ground (Figure 5.6). The same directional components will be experienced when the wheels thump into the ground after the obstacle. It is expected that the downward directed impulse will be much greater than the shear impulse generated in the direction of travel.

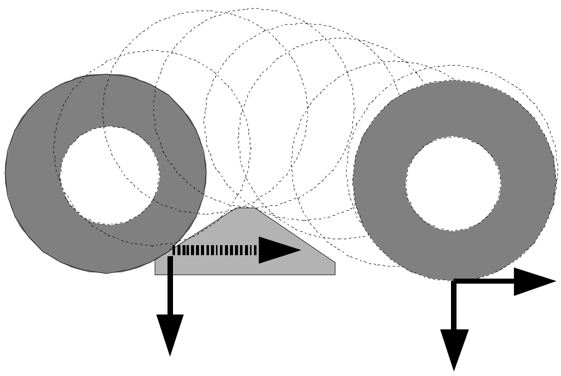

Figure 5.6 Forces excerted by the impacting wheel axis.

The rubber obstacle used in the field work (Figure 5.6) is about 20 cm wide. Theoretically the wheel will generate an impact of a time length corresponding to the time it takes for it to move up to the crest of the obstacle. If the vehicle impacts at a velocity of 60 km/h (16.7 m/s) the time length of the impact will thus be (0.1/16.7 s) 6 milliseconds. Figure 5.7 shows the bandwidth a 6 ms Gaussian impulse will give rise to. As seen it generates a relatively wide band impulse, which covers the low frequencies. In other words, the wheel impact should generate an impulse that stimulates a wide band of frequencies and do not miss the fundamental frequency of the surface layers.

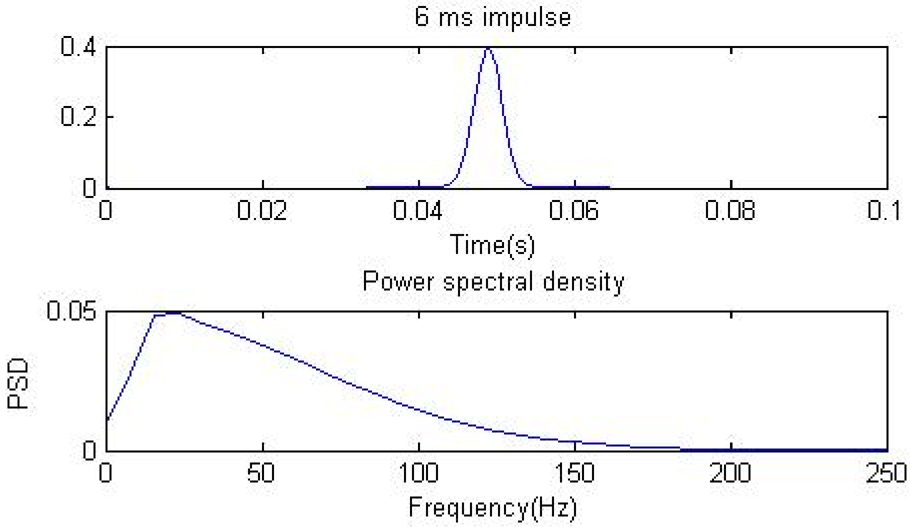

Figure 5.7 A 6 ms impulse and its bandwidth.

The downward directed impulse can be expected to generate a P-wave that travels in a hemispherical wave front from the point of impact. Furthermore it will generate a vertically polarized S-wave (SV) spreading in the same manner but with a lower velocity.
The impulse component in the direction of travel will generate a horizontal S-wave (SH) polarized in the direction of travel. No horizontal S-wave polarized perpendicular to the direction of travel is expected to be generated from the passage.
A Rayleigh wave is also generated that spreads in a cylindrical wave front from the source of impact.

The energy spread from the downward directed impact on a circular footing is distributed over the wave propagation modes as shown in Figure 5.4 (b). 67 % of the energy is spread in the form of Rayleigh waves, 26 % in the form of S-waves and only 7 % in the form of P-waves. The energy spread from the vertical impact of the vehicle wheel axis is probably distributed similarly over the propagation modes.

Apart from these waves created by the passage of the vehicle over the obstacle there will be other waves generated that cloud the picture. The surrounding traffic and the source vehicle itself emit noise from engines and wheels rolling over the pavement.

Because the sensors are located close to the source it is the hypothesis that both the impulse onto the ground and the response of the ground is registered. The impulse would be represented by the direct P-and S-waves arriving to the sensors, while the response is represented by indirect waves, having passed through the surface layers and been reflected at a layer interface or at the bedrock.

5.2.3 Source-inherent effects

The vehicle will give rise to unwanted effects in the passage over the obstacle. Its suspension will create an oscillating motion that is transmitted to the ground long after the time of impact with the ground after the obstacle.
The time between wheel axes impacts will stimulate a frequency correlating to that period. For a boggie of a truck with an axes distance of 1.5 meters travelling at the speed of 60 km /h, the time elapsed between wheel impacts will be 0.09 seconds. A frequency of around (1/0.09) 11 Hz will then be stimulated by the double impact.
Another frequency component will be stimulated by the double impact of a single wheel axis passing over the obstacle seen in Figure 5.6. That is, the initial impact with the obstacle, followed by the landing of the wheel axis on the other side of the obstacle.
For the trailer trucks motions of the vehicle such as pitch or roll rotation of tractor and/or trailer can stimulate certain frequencies.

5.3 Field work

The field work is carried out along the Pan-American Highway in a jeep provided by CIGEO. The work is organized so that the two data acquisition systems are connected and ready for use in the rear compartment of the vehicle (Figure 5.8).

Figure 5.8 The equipment ready in the rear compartment of the jeep.

As the vehicle advances along the route and a site is selected for measurement, only the sensors are lowered onto the ground (Figure 5.9). They are carefully levelled and arranged for good contact with the ground, and then the obstacle is placed on the road

Figure 5.9 The sensors are lowered from the rear compartment of the jeep at the arrival at the site. In this picture only the accelerograph has been placed on the sidewalk.

in a straight line from the sensors. After that the sensors are triggered manually at the passage of a suitable vehicle. Before leaving the site the coordinates are taken with a handheld GPS.

At all sites at least one traffic impulse record simultaneous on both sensors is made, and one noise record when no vehicles are passing. At most sites several traffic impulse and noise records are collected because of uncertainty as to the quality of the records. The simultaneous recordings are synchronized by triggering from both laptop keyboards simultaneously.

5.3.1 Equipment

The equipment used for this study consists of a road obstacle and two data acquisition systems as described in the following sections.

5.3.1.1 Cable protector road obstacle

The obstacle used to have passing vehicles generate an impulse is a cable protector of the type used in road works. It is sufficiently big to have the wheel axes of the vehicles create a distinct impulse, but at the same time sufficiently small to have the drivers, in the most cases, go past it without reducing their speed.

5.3.1.2 Tri-axial accelerograph

The tri-axial accelerograph is of the type Kinematrics K2. It is a digital recorder with an accelerometer of the type EpiSensor mounted to it. It is connected to a laptop, from which it is operated. It may also be left standing without a computer connection with a set trigger threshold for seismic event recording. In this study the possibility to manually trigger the accelerograph is wanted, and therefore it is connected to a laptop for operation. The most important characteristics of the accelerometer and recorder of the K2 are given in Table 5.1.

Figure 5.10 Cable protector and tri-axial accelerometer in their positions.

Accelerometer EpiSensor

Sensitivity:	5.0V/g / 0.510 V/m×s^{-2}
Measurement range:	±1g
Output range:	±2.5 V
Resonance:	not known
Dynamic range:	155 dB
Bandwidth:	less than 5 % error in range DC - 80 Hz

Recorder Kinematrics K2

Input range:	±2.5 V
Sampling rate:	100 - 250 Sa/s (set to 250 Sa/s)
Dynamic range:	114 dB
Bandwidth:	DC- 120 Hz

Table 5.1 Some important characteristics of the K2 accelerograph (Kinemetrics).

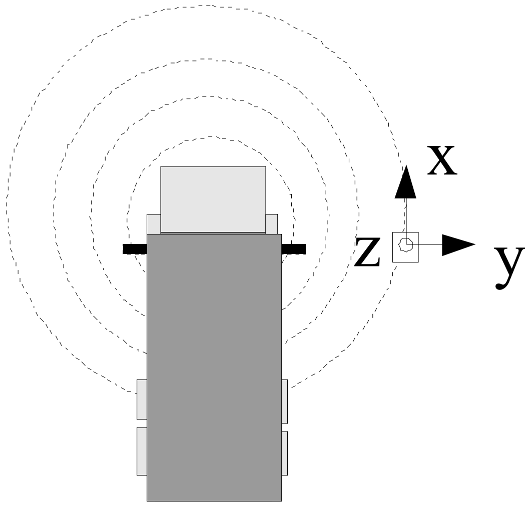

Figure 5.11 Waves spread from the impacting vehicle and recorded by the tri-axial accelerograph.

The accelerograph has three axes denominated x, y, and z, marked on the cover of the accelerograph. In all the recordings the x-axis is oriented in the direction of the traffic flow, the y-axis perpendicular to the traffic flow and the z-axis vertically (Figure 5.11). The accelerograph is carefully levelled by means of its three adjustable feet and with the aid of a spirit level.
The x-axis is expected to register the horizontal S-wave (SH_x) originating from the travel parallel impulse created by the wheel. It cannot experience any contribution from the Rayleigh wave generated by the traffic impulse as it is oriented perpendicular to the propagation direction of the Rayleigh wave. It may experience noise-inherent Rayleigh waves however.
The y-axis will register the horizontal component of the Rayleigh wave, and the direct P-wave. It may also register indirect horizontally polarized shear waves having been reflected in the surface layer boundaries.
The z-axis will register the P-wave, the vertically polarized S-wave (SV) and the vertical component of the Rayleigh wave.

As seen the accelerations detected on each axis of the accelerograph is not easily isolated as resulting from any particular propagation mode, except for the x-axis where the acceleration has to belong to S-waves parallel to the direction of travel (SH_x). The measured accelerations are best treated without bias simply identifying resonances and attenuation regardless of propagation mode.

Normally the data collected with the accelerograph is transferred to the laptop at the end of the field work day.

5.3.1.3 Uni-axial accelerometer-A/D converter data acquisition system

This data acquisition system consists of a uni-axial accelerometer connected to an A/D converter (analogue to digital converter), which in turn is connected to a laptop in order to save recorded data.
The data acquisition system has a uni-axial accelerometer of the type PCB 393A03 as sensor. The accelerometer gives a voltage output signal proportional to the ground acceleration. This is connected through an amplifier to the Lawson Labs 301 24-bit A/D converter, which converts the analogue signal to a digital in order to permit the laptop to read the data. In Table 5.2 some of the important characteristics of the data acquisition system can be seen.

Accelerometer PCB 393A03

Sensitivity:	1.0 V/g / 0.102 V/ m×s^{-2}
Measurement range:	±5g
Resonance frequency:	>10 kHz
Bandwidth:	less than 5% error in range 0.5 - 2000 Hz

A/D converter Lawson Labs 301

Input range:	±5.0 V
Sampling rate:	50 - 1000 Sa/s (set to 500 Sa/s)
Bandwidth:	DC - 0.262 * sampling rate

Table 5.2 Some important characteristics of the uni-axial accelerometer-A/D converter data acquisition system (Piezotronics, 2002).

5.3.2 Measurement Strategy

The Pan-American Highway was chosen as the route on which to evaluate the Spectrogram Evaluation Technique. It passes through the whole of Managua, first from east to west in the northern parts of the city close to Lake Xolotlán, then turning south just after the city centre going uphill to the higher ground of south-western Managua. The route was chosen for several reasons. Most of the heavy traffic passes through Managua on this route making it an ideal seismic source. It passes through the lowest part of Managua in the vicinity of Lake Xolotlán, were the thickest surface layers should be, due to the transportation of sediments by surface runoff (Figure 5.12). In the fault zones these sediment layers would be expected to be thickest. When the route turns south and goes uphill topographic effects can be seen. Furthermore the Pan-American Highway passes through the old city centre of Managua and the parts of the city that were demolished in the 1972 earthquake.

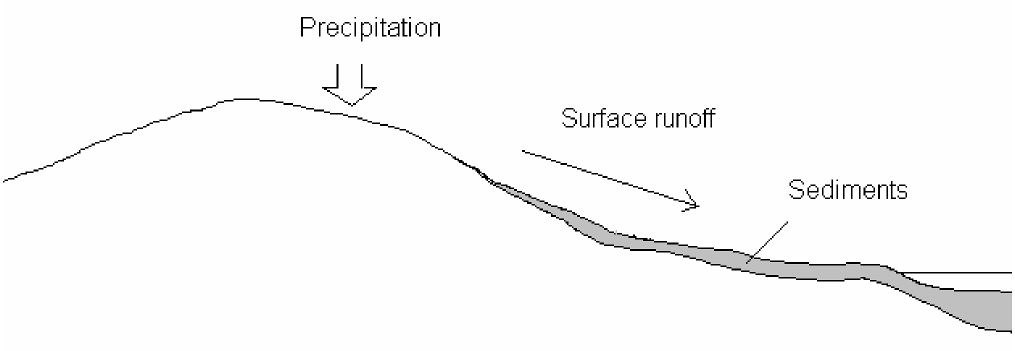

Figure 5.12 Surface runoff and expected sediment thickness in Managua.

The measurements are made as close to one another as possible, but not closer than 50 meters. Along certain segments of the route it is not possible to carry out measurements due to traffic lights with heavy queuing and resulting low velocities and unfavourable noise. Along other segments the impossibility to stop the vehicle due to security reasons leaves blanks in the data acquisition. An example of that is in front of the United States' embassy where a gap, which can clearly be seen in the map, had to be left open (Figure 5.13).

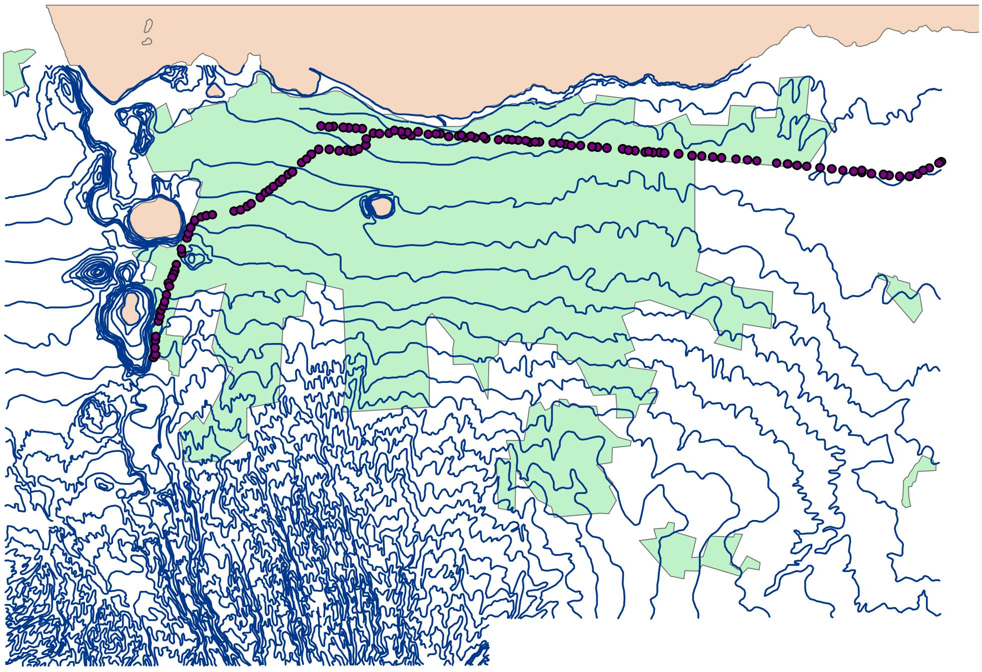

Figure 5.13 Topographic map of Managua with measurement sites marked as dots.

Where abrupt differences in surface layer thickness can be expected measurements are carried out in closer intervals if possible. That is in this case in the vicinity of suspected or documented faults, water channels or surface streams.

5.4 Signal processing

The collected data is analyzed with the use of Matlab. Mostly the analysis is made with respect to frequency content of the recorded ground response signal.
First in this chapter is a paragraph on the initial organisation of the data necessary for further processing. After that the transform of a signal from time to frequency domain, which is the basis for all frequency analysis, is shortly described.
Before moving on to the hazard analysis, a coherence analysis is made between the vertical and horizontal components of the accelerograph. Then a cross-correlation analysis is made to compare simultaneous recordings from the tri-axial accelerograph and the uni-axial accelerometer.
Finally in this chapter the theory behind the spectrogram is explained, which is the basis of the time-frequency hazard analysis explained in chapter 5.5.

5.4.1 Initial data treatment

Before evaluation events are picked visually from the recorded vehicle passages. First the recorded data is sorted and graded according to quality for each site. Then the best event in each record is screened by assigning a start sample point and an end sample point and applying a hanning window. The event is the impact of one wheel axis and the decaying oscillations experienced by the ground afterwards. The characteristics considered when choosing an event is the power of the signal and the amount of background noise. An ideal event has so much power as to dwarf sources of noise (paragraph 5.2.1). It also needs to have frequency components in a wide spectrum, especially in the lower frequencies were an earthquake has its dominating frequency content.

The average of the signal is subtracted from it, in order to remove the DC-component and have the signal oscillate around zero volt. The acceleration values given in the data files are in volts and have to be scaled according to the sensitivity of the accelerometers. The EpiSensor accelerometer of the K2 accelerograph has a sensitivity of 5.0 V/g or 0.510 $V/m{\times}s^{-2}$ (Table 5.1) and the PCB 393A03 uni-axial accelerometer has a sensitivity of 1.0 V/g or 0.102 $V/m{\times}s^{-2}$ (Table 5.2).

5.4.2 Transform from time to frequency domain

The mathematical basis of frequency analysis is the Fourier transform, i.e. the transform from time to frequency domain. The following explanation of the theory behind the Fourier transform is based on (Randall and Tech, 1987).

In the Fourier theory a signal is assumed to be composed of a number of sinusoidal or, if you wish, cosinusoidal components at various frequencies. Each of them has its own amplitude A and initial phase φ.

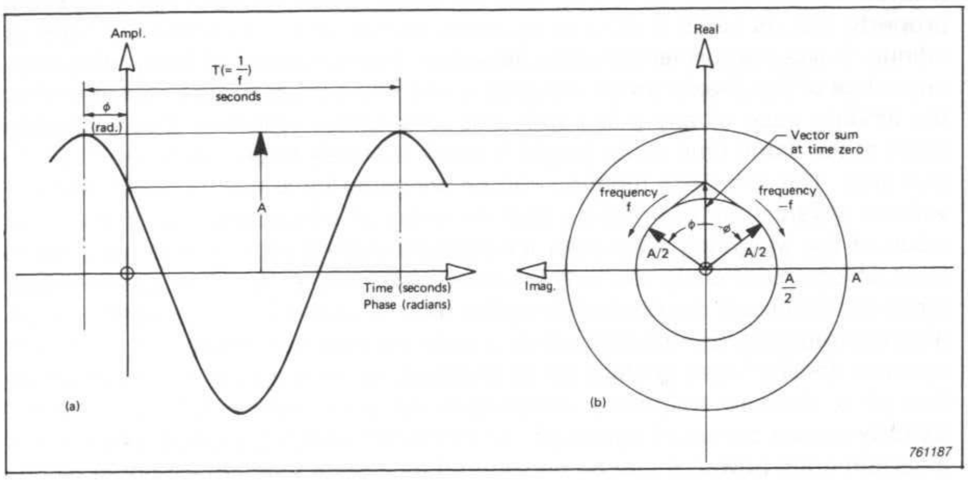

Figure 5.14 Complex representation of a sinusoidal component (Randall and Tech, 1987).

A sinusoidal component may be represented by two vectors with a real and an imaginary part, rotating in contrary directions. Each has the amplitude A/2. One has the initial phase angle φ and rotates with frequency f, and the other has the initial phase angle –φ and rotation frequency –f (Figure 5.14).

As the vectors rotate with time the imaginary parts will always cancel out and therefore the resultant will always be real. In the real plane the oscillation would look like on the left side of Figure 5.14 and have amplitude A. The mathematical identity can be written:

$$A\cos\theta = \frac{A}{2}(e^{j\theta} + e^{-j\theta}) \qquad (5.10)$$

$$where \quad \theta = (2\pi ft + \varphi) \quad and \quad j = \sqrt{-1}$$

If this function is multiplied by the factor $e^{-j2\pi ft}$ the rotation freezes and the function integrates to a finite value. This is the basis of the Fourier transform.
Let us say that we have a periodic function which according to the Fourier theory is a sum of sinusoidal components at equally spaced frequencies kf_1 *(harmonics)*

$$g(t) = g(t + nT) \qquad (5.11)$$

where T is the period and n is any integer.

Then the *k*th frequency component is given by:

$$G(f_k) = \frac{1}{T}\int_{-T/2}^{T/2} g(t)e^{-j2\pi f_k t}\,dt \qquad (5.12)$$

$$where \quad f_k = kf_1 \; and \quad f_1 = 1/T$$

Because the rotation freezes the component of frequency f_k will integrate to a finite value. All other frequency components will continue their rotation and integrate to zero (Figure 5.15).

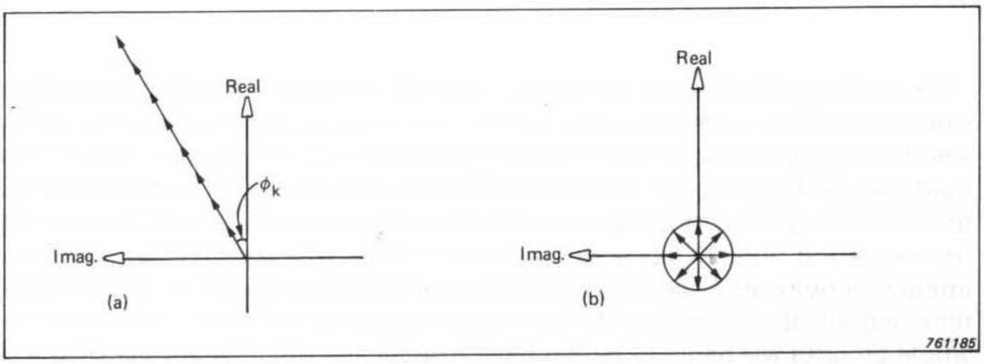

Figure 5.15 (a) Because the rotation stops the frequency component integrates to a finite value. (b) All other frequency components continue their rotation and integrates to zero (Randall and Tech, 1987).

Thus equation (5.12) will extract the frequency component f_k from g(t). It also freezes the phase angle as that existing at time zero. If we multiply the initial value $G(f_k)$ with the oppositely rotating unit vector $e^{-j2\pi ft}$ we will again obtain the actual position of each vector and return to the signal g(t).

$$g(t) = \sum_{k=-\infty}^{\infty} G(f_k) e^{j2\pi f_k t} \qquad (5.13)$$

In the Fourier transform equation (5.12) and (5.13) is extended to the general case by letting T go to infinity. The spacing between harmonics (1/T) then tends to zero and G(f) becomes a continuous function of f.

$$G(f) = \int_{-\infty}^{\infty} g(t) e^{-j2\pi ft} dt \qquad (5.14)$$

is known as the forward Fourier transform and

$$g(t) = \int_{-\infty}^{\infty} G(f) e^{j2\pi ft} df \qquad (5.15)$$

is the inverse Fourier transform. G(f) is the complex frequency spectrum.

In the case of a sampled signal the forward transform takes the form:

$$G(k) = \frac{1}{N} \sum_{n=0}^{N-1} g(n) e^{-j\frac{2\pi kn}{N}} \qquad (5.16)$$

where N is the number of time samples. The inverse transform takes the form:

$$g(n) = \sum_{k=0}^{N-1} G(k) e^{j\frac{2\pi kn}{N}} \qquad (5.17)$$

This is the Discrete Fourier Transform (DFT). To obtain N frequency components from N time samples requires N^2 complex multiplications. That is why in for example Matlab an algorithm called the “Fast Fourier Transform” or “FFT” which requires only N $\log_2 N$ operations is used. It gives the same result.
In this way one can change between the time domain acceleration signal and the frequency domain complex spectrum.

The complex representation of an oscillation with a real and an imaginary part can be interpreted as the interaction between potential and kinetic energy in a wave motion.

The square of the real part represents potential energy and the square of the imaginary part represents kinetic energy.
When the potential energy is at its maximum at the extremity of an oscillation the velocity is zero (i.e. the kinetic energy is zero) and all energy is in the form of internal strain energy.
When no strain energy exists at the centre of the oscillation, the velocity and the kinetic energy is at its maximum.

5.4.3 Coherence between vertical and horizontal components

The coherence analysis is made to create an idea of how the motions detected on the axes of the accelerograph are related.
The coherence gives a measure of the degree of linear dependence between the acceleration recorded on each accelerometer axis, as a function of frequency.

First the cross-spectrum of the two signals has to be calculated. It is done by multiplying the complex spectra of one signal with the conjugate of the other's. The cross spectrum from A to B is:

$$S_{AB}(f) = A^*(f) \cdot B(f) \quad (5.18)$$

The cross spectrum from B to A would have the same amplitude, but opposite phase.

The coherence is calculated like:

$$\gamma^2(f) = \frac{\left|G_{AB}(f)\right|^2}{G_{AA}(f) \cdot G_{BB}(f)} \quad (5.19)$$

where G_{AA} and G_{BB} is the autospectra of each signal.
In Matlab the function "mscohere" does the operation described. A coherence of "1" means a perfect linear relationship between the two signals at that frequency, while "0" means there is no linear relationship at all.

There are basically four reasons to why the coherence may be low between two signals *a(t)* and *b(t)* (Randall and Tech, 1987):

1. The presence of uncorrelated noise in *a(t)* and/or *b(t)* (Figure 5.16).
2. Non-linear relationship between *a(t)* and *b(t)*.
3. Leakage due to insufficient resolution, and/or wrong choice of window function. That is the power from discrete frequency components leaks into adjacent bands.
4. Time delay between the signals, where this is in the order of the length of record.

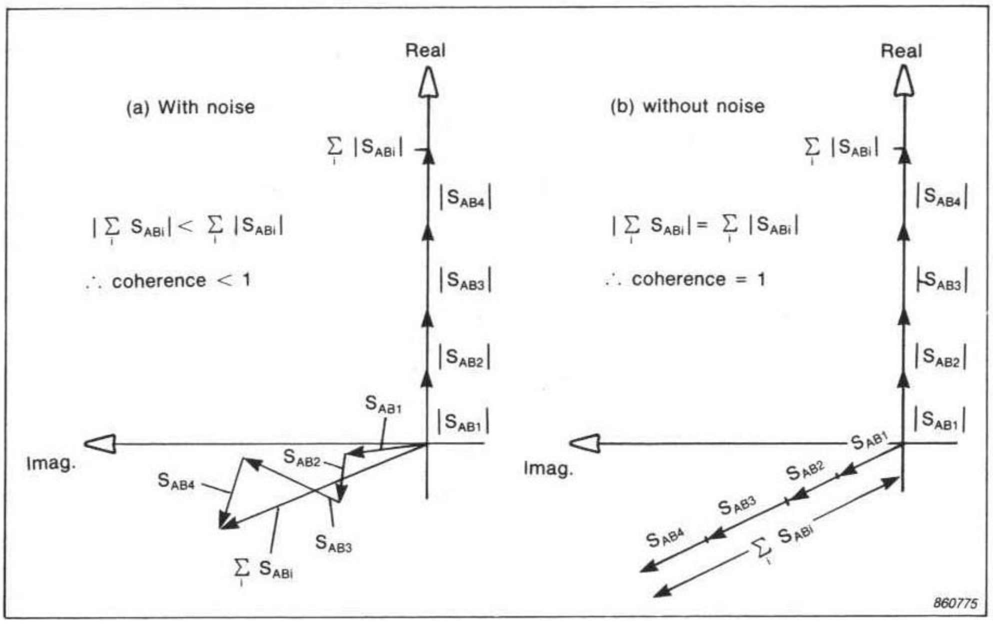

Figure 5.16 The effect of noise on coherence between signals (Randall and Tech, 1987).

5.4.4 Correlation between sensors

The cross-correlation function is used to see how accelerations registered on the vertical axis of the accelerograph correlates to those registered on the uni-axial accelerometer, as a function of time displacement between the two.
For transient signals the cross-correlation function is defined as:

$$R_{ab}(\tau) = \int_{-\infty}^{\infty} a(t)b(t+\tau)dt \qquad (5.20)$$

where τ is the time displacement.
If the signal recorded on the uni-axial accelerometer is the same as that recorded on the vertical axis of the accelerograph, it would be expected that the two signals are practically identical. However they will inevitably be displaced by a time τ_0, as the starting point of the events where not picked at exactly the same sample point. Then the cross-correlation of the two would be similar to the autocorrelation, but displaced with τ_0.

5.4.5 The Spectrogram

The spectrogram shows how the frequency content of a signal changes with time. It is presented in a diagram with one time axis and one frequency axis. The magnitude of each frequency at each time is represented on a colour scale. The spectrogram is calculated by splitting the signal into overlapping sections with a window function. Each window is then Fourier transformed to the frequency domain. This gives the short-term frequency content which is taken as representative for an instant in time. It is termed Short-Term Fourier Transform (STFT) (Gade and Herlufsen, 1994). The principle of applying the short-term Fourier transform is shown in Figure 5.17.

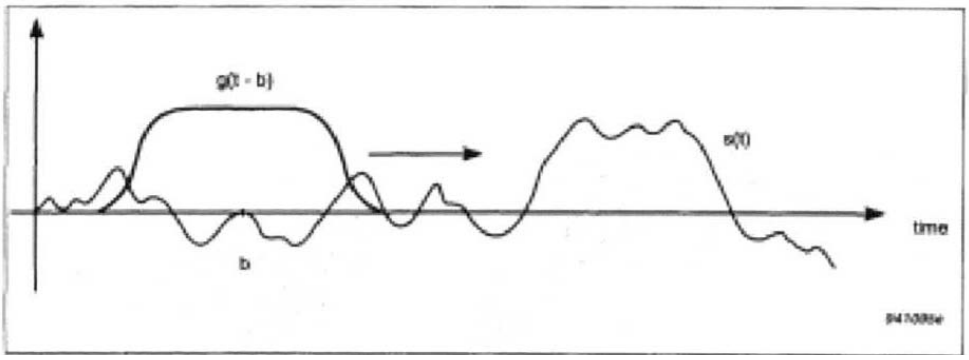

Figure 5.17 The short-time Fourier transform extracts spectral information from the signal around time b (Randall and Tech, 1987).

The idea behind analyzing the data with a spectrogram is to clearly see at what frequencies the signal remains longest. Such frequencies could be resonance frequencies of the surface layers. Another advantage is that the Rayleigh wave and the direct P- and S-wave will pass the sensors quickly after the generated impact, and their frequency content thus disappears from the spectrogram image. Left will only be the frequency content of standing P- and S- waves.

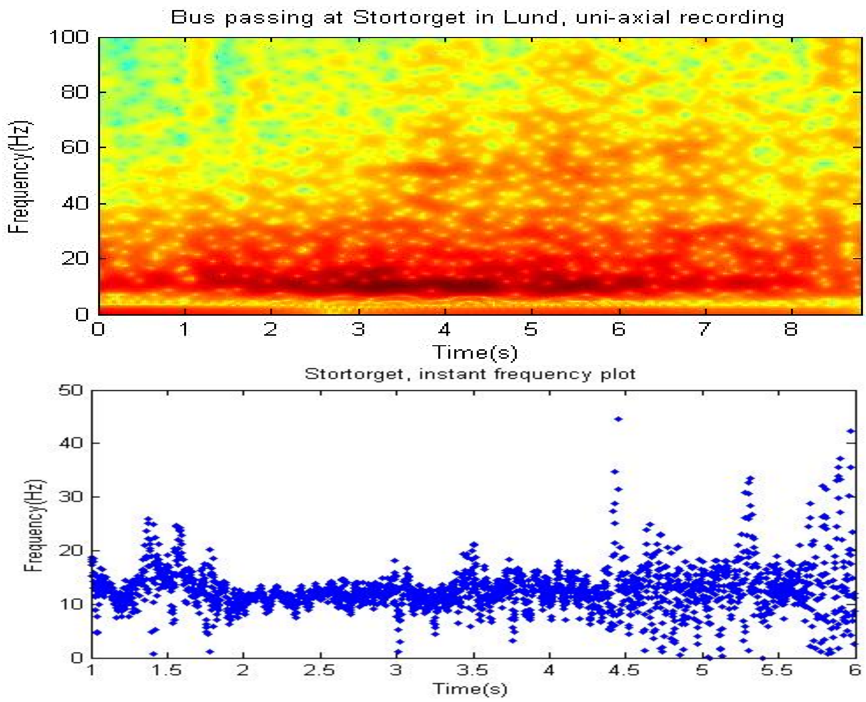

Figure 5.18 Top: Spectrogram representation of the ground impulse response from a bus at Stortorget in Lund. Bottom: Instant frequency of the same impulse response.

Measurements were carried out at Stortorget in Lund by Rainer Parrales and Peter Ulriksen, before the field campaign started in Managua. The spot was chosen because it was known to experience heavy vibrations at the passage of city busses. These measurements show a clear resonance frequency around 11 Hz prevailing in the spectrogram (Figure 5.18).

The instant frequency plot in the same figure shows that the frequency content of the signal narrows down around the resonance frequency immediately after impact and then regains its normal distribution slowly as the impulse response is attenuated. The instant frequency is calculated as the angular difference between to successive sample points in the signal. This gives the instant angular frequency which is then converted to Hz.

5.4.6 Implications of the short-term Fourier transform

Screening a signal with the short-term Fourier transform allows us to see the short-term frequency content of the signal, and how the frequency content changes with time. But it also means a limitation in the low frequencies, due to the short sampling period.

A 1 Hz oscillation has a period of 1 second. It will need at least a one second long window in order to be "detected" by the Fourier transform and identified as a 1 Hz frequency. Otherwise it will end up as DC. Thus the shorter the window function applied in the STFT is, the higher the frequency threshold in the spectrogram will be.

5.5 Time-frequency hazard analysis

The objective of the data processing is to evaluate the seismic risk along the Pan-American Highway. This is done by a time-frequency hazard analysis of the site response which will be described in the following sections.

5.5.1 Instantaneous risk

The earthquake-sensitivity of a site is the result of the combined effect of the earthquake input motion, surface layer response and structure response. In other words the earthquake signal filtered through surface layers and structure.

In the time-frequency hazard analysis the characterization of a site is made by convolving an earthquake signal with a local ground response signal and a building response signal. This will give an estimate of the combined resultant motion, i.e. the site response.

The *sensitivity spectrum* is the frequency content of the site response in one time instant. It is estimated by convolving the measured ground response, i.e. the site spectrogram, for a time instant t with an earthquake spectrum and a building response spectrum. Convolving signals is the same as multiplying their spectra in the frequency domain.

$$\overline{S} = \overline{E} \cdot \overline{R} \cdot \overline{B} \qquad (5.21)$$

where $\overline{S}$ is the sensitivity spectrum, $\overline{E}$ is the earthquake spectrum, $\overline{R}$ is the ground response spectrum and $\overline{B}$ is the building response spectrum. The spectra are all normalized so that the integral over all frequency components becomes one. The ground response spectrogram is normalized so that the integral of frequencies is one at impact, and then attenuates. In this way a general measure of site response is obtained that is not dependent on the power of the impact measured.

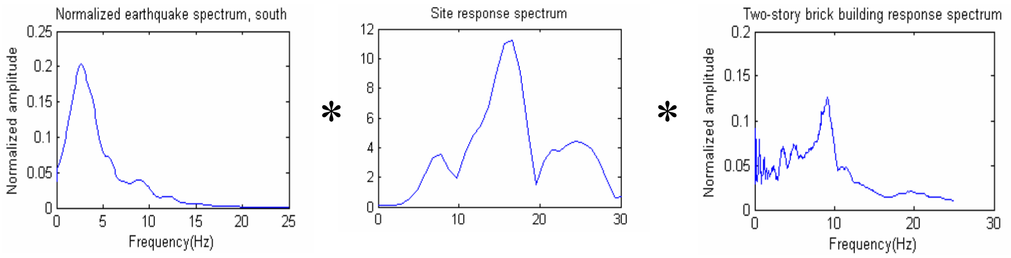

Figure 5.19 Convolving the earthquake spectrum with the site response spectrum and the building response spectrum gives us the sensitivity spectrum.

The earthquake spectrum is taken from seismograph recordings of the 1972 earthquake (Figure 5.20), provided by Orlando Hernandez Rubio from the Managua Municipality. It is from the main shock recorded at the Esso refinery the 23rd of December, 06.29 in the morning. Its location can be seen in Figure 4.2.

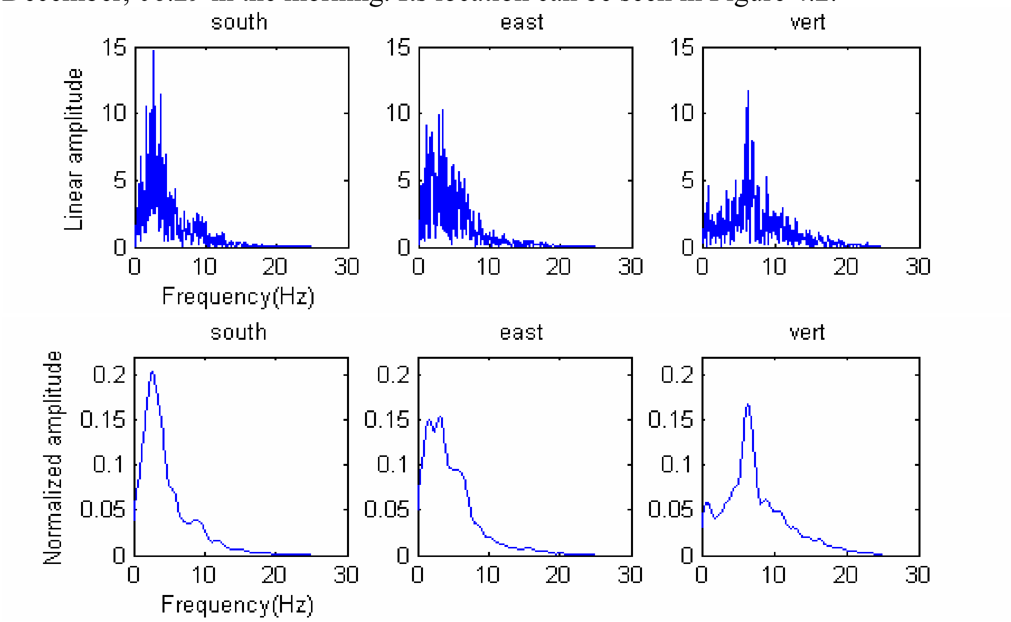

Figure 5.20 Spectra from the main shock of the earthquake that struck Managua the 23 December, 1972. Top: the rough Fourier transforms. Below: The smoothened and normalized spectra.

The acceleration has been recorded in the directions south, east and downwards. When evaluating the vertical site response the accelerogram measuring the downward acceleration is used. For horizontal site response evaluation both directions south and east are entered into the model in order to see if it results in any differences.

The building response spectrum is taken from recordings of the response to microtremors of a two-story brick house in Masaya (Figure 5.21), also carried out by Orlando Hernandez Rubio (Hernández-Rubio, 2005). The recordings were done by locating external sensors connected to the Kinemetrics K2 accelerograph close to the ceiling and oriented in the two principal directions of the building. A third sensor was located in a top corner of the building in order to register torsional motion. In this study one of the directional recordings is used when entered into the site response model. The recordings in both directions exhibit peaks at the same frequencies.

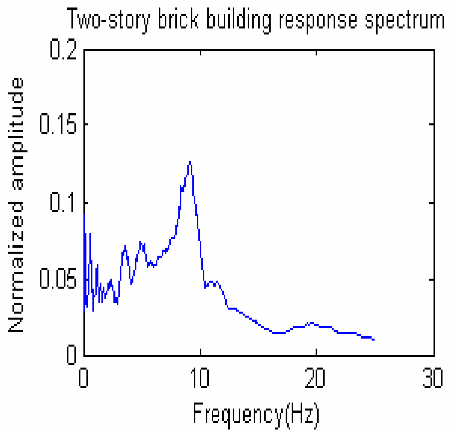

Figure 5.21 Response spectrum from microtremor recordings in a two-story brick building.

The building response spectrum shows a distinct peak around the frequency 9 Hz, which is the fundamental resonance frequency of the building. Another less distinct peak is present at 20 Hz.

By taking the integral of the sensitivity spectrum, i.e. the sum of amplitudes over all frequencies, a measure of the *instantaneous risk* is obtained.

$$I = \int A(f)df \qquad (5.22)$$

where $A(f)$ is the amplitude of frequency component f.

5.5.2 Local risk

The spectrogram provided by the traffic impulse response approach, convolved for each time instant with the earthquake spectrum and the building response spectrum, gives the time history of the instantaneous risk. As mentioned in the previous section the instantaneous risk is defined as the integral of the sensitivity spectrum. The instantaneous risk will then vary over time as the motion is damped (Figure 5.22). This can be interpreted as the damping of the total frequency energy content.
The removal of noise can be done at this stage by simply removing the noise floor left where the instantaneous risk curve stabilizes and no more effects from the event can be seen.

In an earthquake the motion of the bedrock will continue to pump in energy in the surface layers for some time. The damping will then be the factor that determines the magnitude of the energy build-up, if there is any. Thus the time-history of the instantaneous risk will be a direct measure of the earthquake sensitivity of the site, and the area enclosed under the instantaneous risk curve is a measure of the *local risk*. The local risk L is thus defined as:

$$L = \iint A(f)\,df\,dt \qquad (5.23)$$

That is, *the double integral of amplitude over frequency and time*, or put differently the volume enclosed under the convolved spectrogram.

As all the convolved spectra are normalized in this study to have the integral of frequencies as one, the local risk will attain a very small value. Therefore the local risk is multiplied by a factor of 1000 to give a local risk index.

$$Local \quad risk \quad index = 1000 \times \iint A(f)\,df\,dt$$

This is an index invented for this study but it does justly represent the local risk of a site, as it takes into account both resonance and attenuation of the site. It is an integrated measure of resonance and damping of surface layers.

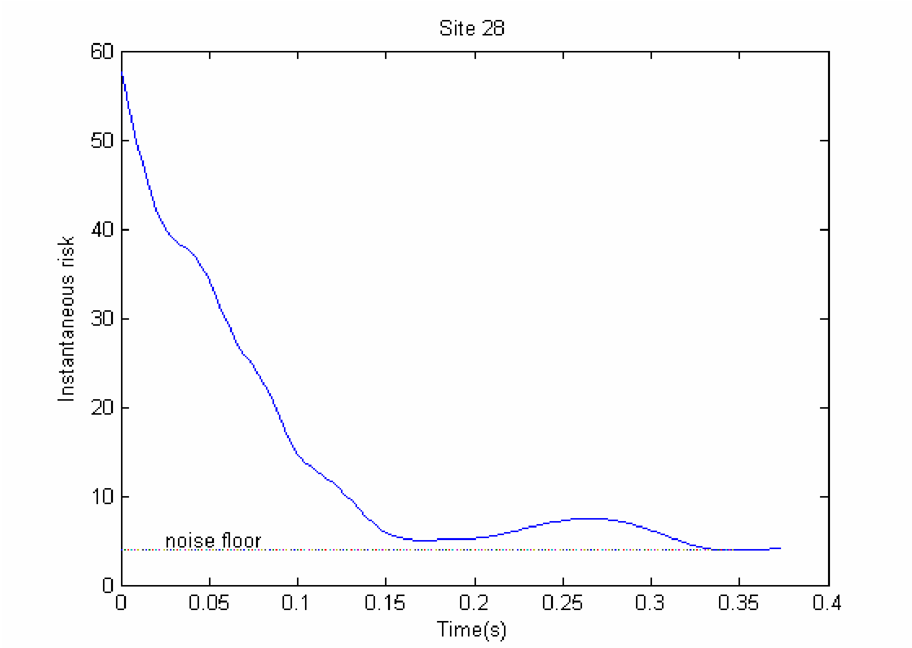

Figure 5.22 Instantaneous risk curve.

5.5.3 Constant background removal

In the traffic impulse response measurements a number of effects not inherent in the surface layer characteristics are likely to be present. These include effects from the cable protector, source vehicle, road fill and background noise. Especially the road fill can create characteristic frequencies and resonances that have nothing to do with the site response experienced by other structures on the ground. Some of the effects are global and can be removed by subtracting the average of all site response spectra from the site response spectrum. This would remove background effects that most sites have in common. It would also remove effects from geological characteristics that the sites have in common, and leaves us with only the site specific effects.

$$S_{med} = \frac{\sum \overline{R}}{N} \tag{5.24}$$

where N is the total number of sites. The site specific response spectra can then be written:

$$\overline{R}_{sitespec} = \overline{R} - S_{med} \tag{5.25}$$

6 Results

The measurements carried out along the Pan-American Highway are in all 128 points, running from the eastern city limit to the south-western city limit of Managua as seen in the map in Appendix 1. For the recorded site response of each site an analysis of coherence between axes and correlation of the recordings from the two sensors is made. After that an interpretation of the spectrograms regarding resonances and damping is attempted. Finally the time-frequency hazard analysis is undertaken in order to get an estimate of the earthquake-sensitivity of the site.

6.1 Coherence between the accelerograph axes

A coherence analysis is performed in order to see to what degree the motions detected by the different axes in the K2 accelerograph are related to one another. The coherence tells us to what degree two signals are linearly dependent at each frequency. Thus it clarifies if the acceleration on two axes gives the same information, or if they exhibit independent motion characteristics.

Some of the sites show very high coherence between axes, while others show very low coherence. A high coherence means that we will get little extra information from the second axis regarding the ground response to impact.

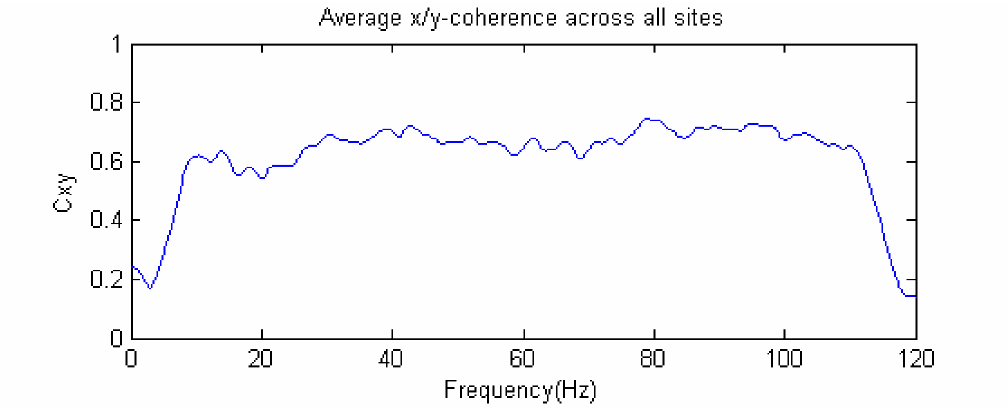

Figure 6.1 Average coherence between the accelerograph x- and y-axes

The average coherence between x- and y-axes across all the sites is seen in Figure 6.1. On the horizontal axis is the frequency and on the vertical axis the coherence as a function of frequency is shown.

The coherence between the horizontal x- and y-axes is intermediate. This is the result of some sites showing high coherence, while others exhibit low to intermediate coherence. Several sites exhibit a coherence close to unity over a wide band of frequencies as can be seen for example in the plotted coherence of site 37 in Figure 6.2. Other sites exhibit very low correlation between the x- and y-axis as for example site 10 seen in Figure 6.3.

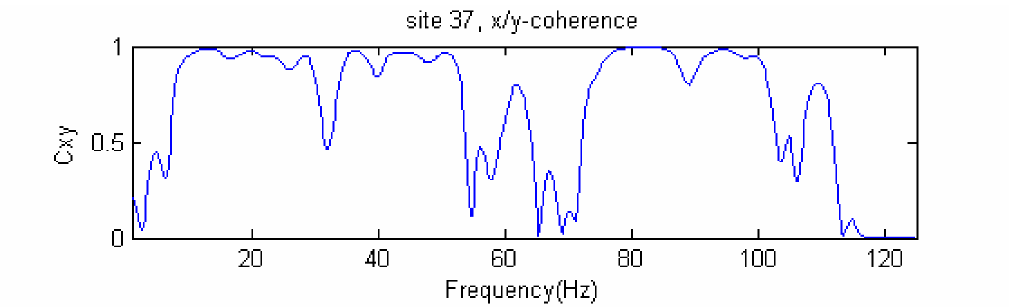

Figure 6.2 Coherence between x- and y-axis at site 37.

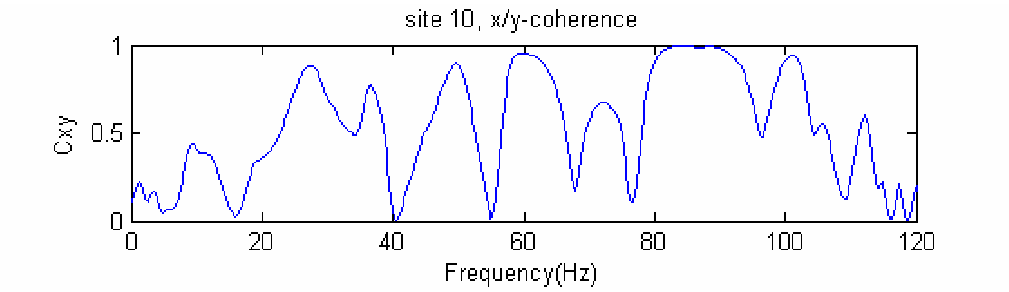

Figure 6.3 Coherence between x- and y-axis at site 10.

The coherence between x- and z-axis is of greater interest as it will show the linear dependence of vertical to horizontal motion. If the coherence between vertical and horizontal acceleration is high it means that an analysis of vertical acceleration on the uni-axial accelerometer can be used to estimate also resonances and attenuation in the horizontal direction. The average coherence between x- and z-axis is seen in Figure 6.4.

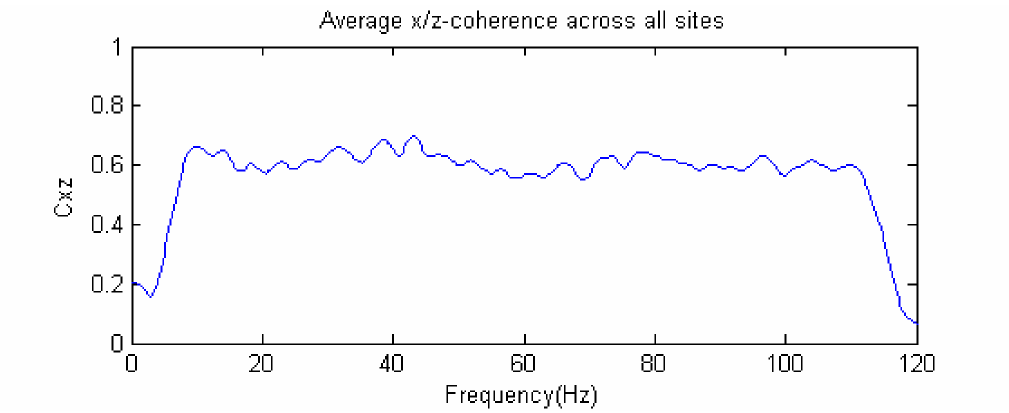

Figure 6.4 Average coherence between the accelerograph x- and z-axes

The average coherence over all sites is again intermediate. However, there are sites which exhibit coherence close to unity for a wide band of frequencies, especially up to 50 Hz. Again taking the case of site 37 this fact is seen (Figure 6.5). Others exhibit low coherence, like site 10 in Figure 6.6.

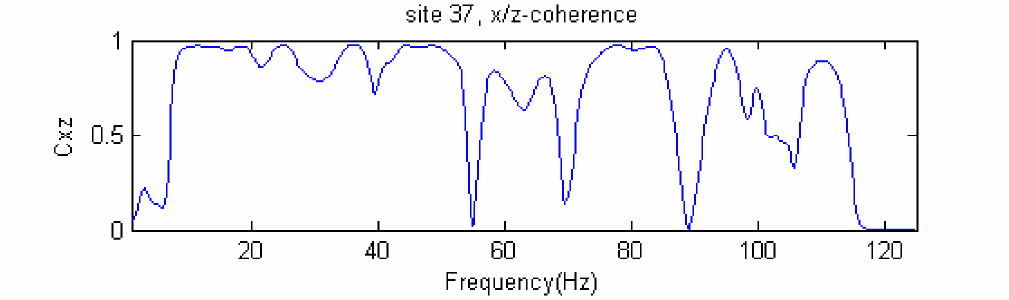

Figure 6.5 Coherence between x- and z-axis at site 37.

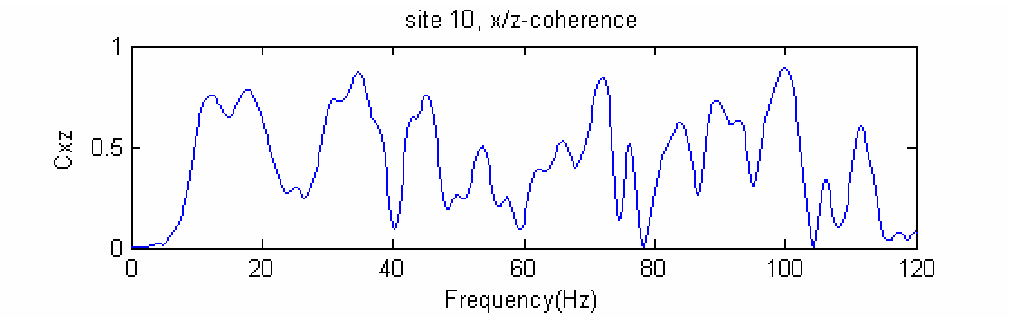

Figure 6.6 Coherence between x- and z-axis at site 10.

The average coherence between y- and z-axis is shown in Figure 6.7. The coherence curve shows a higher coherence below 50 Hz, which may be due to strong influence from surface waves that are detected as well on the y-axis as on the z-axis (see section 5.3.1.2).

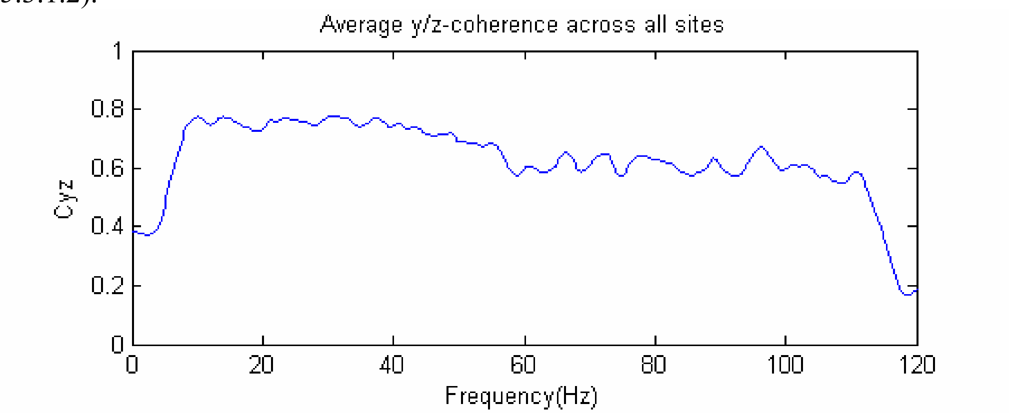

Figure 6.7 Average coherence between the accelerograph y- and z-axes.

Again some sites, like for instance site 37 show high coherence (Figure 6.8), while others like site 10 exhibit very low coherence (Figure 6.9).

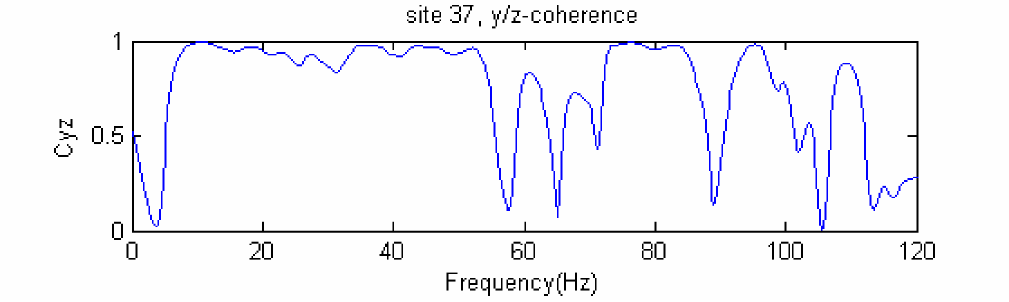

Figure 6.8 Coherence between y- and z-axis at site 37

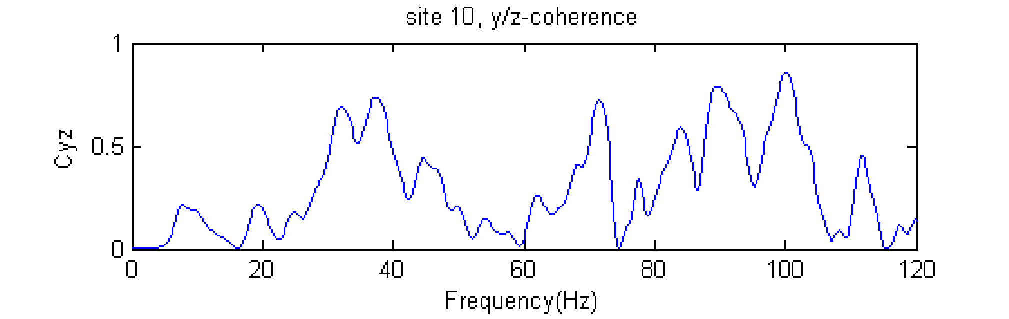

Figure 6.9 Coherence between y- and z-axis at site 10.

The intermediate coherence between horizontal and vertical components indicates that the vertical and horizontal acceleration is not enough related to perform an analysis of them as representatives of the same vibration response. As seen in section 4.3.2 the S-waves and P-waves are expected to experience resonance at different frequencies due to different propagation velocities. If P- or S-waves can be expected to be detected primarily on either one of the three axis, it would not be a good idea to treat them as the same response from that point of view either.
As mentioned in section 5.3.1.2 the acceleration measured on each axis of the accelerograph is not easily linked to a unique propagation mode, and the coherence analysis emphasizes that suspicion. The tri-directional information the accelerograph provides can be used to create a more complete picture of the ground response. No information on the type of waves emitted from the source and measured as impulse response can be derived from it by simply looking at the directional acceleration.

Generally it is seen from all the averaged coherence plots that the coherence is intermediate. As stated in section 5.4.3 the low coherence between axes that several sites exhibit may have many reasons.
The time displacement between the signals is depreciable as the signals are registered at the same time and position, and the start of the screened events has been picked at exactly the same sample point. Thus it can not be the reason for a low coherence. The resolution should be high enough not to create any low coherence due to leakage.

That leaves us with noise interference or nonlinear relation between vertical and horizontal motion as possible explanations to the low coherence.
The uncorrelated noise content of the signals affects the coherence negatively. In this case the recordings on all axes are made at the same time and at the same location and thus the noise would be expected to be well correlated between the axes.
The fact that some sites exhibit high coherence while others exhibit low, could mean that different kinds of vibrations are generated at different sites. Another probable explanation is that the distance to the source influences the coherence. If the sensors are located very close to the source the wave field may not yet be developed, and exhibit a more chaotic behaviour. This is not to be considered a flaw however, being that the most probable seismic source is located in the faults close to Managua. Such an earthquake is probable to exhibit a chaotic wave field rather than the developed wave field an earthquake in the subduction zone would give rise to.

The conclusion has to be that it is not safe to assume similar behaviour from the vertical and horizontal motion as the general case. The horizontal and vertical acceleration has to be treated as such, and not as different types of wave propagation. It should be noted, however, that in many of the measurements coherence close to unity between components is observed, in x/y-coherence, x/z-coherence and y/z-coherence alike. This can be observed for example from the coherence plot from site 37.

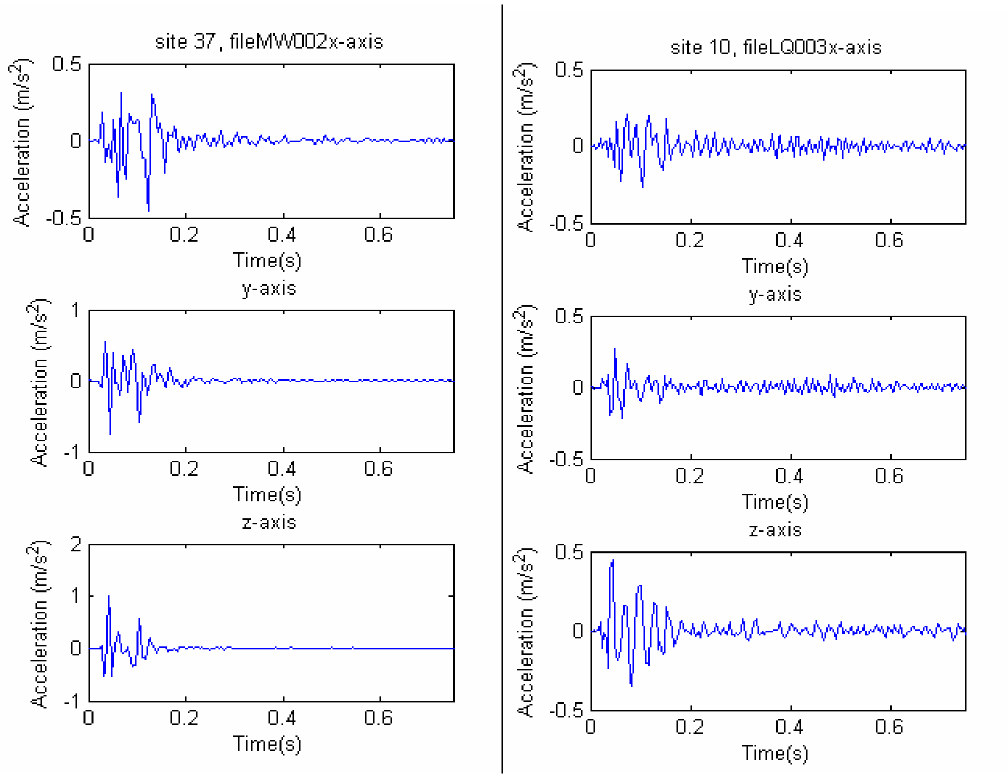

Figure 6.10 Response signals registered on x-, y- and z-axis at site 37 and site 10.

It may be the case that in sites with a high noise level relative to the impact, the coherence becomes lower. In this section site 37 has been taken as an example of high coherence between the components and site 10 as an example of low coherence. The coherence at site 37 and 10 is calculated from the impulse response signals shown in Figure 6.10.

It can be seen from the figures that the response signal of site 10 has less power and is also less distinct than the response signal of site 37. In other words it does not succeed as well in dwarfing the noise level. The noise after the impact probably comes from the vehicle's engine or suspension system. Worth is also noticing that the peak acceleration registered on the z-axis is higher than the one registered on the x-axis and y-axis. This is the general case in the recordings.

6.2 Correlation between the vertical axes of the sensors

The correlation analysis is carried out in order to see how well the response signals registered by the vertical axes of the two sensors match one another. That is, if the vertical axis of the accelerograph records the same motion as the vertical (and only) axis of the uni-axial accelerometer.

The uni-axial accelerometer recordings are down-sampled to half their original sample rate, in order to have the same sample rate as the accelerograph, which is 250 samples per second.

In the correlation analysis the signals are displaced one sample at a time with respect to one another, and the correlation is checked at each displacement according to equation (5.20). Thus the correlation is also used as a way of checking if the events picked from the two sensors correspond to one another. If the correlation peak is not distinct and unique, it is probable that the same event has not been chosen from the two sensors, or that the startpoint and endpoint of the events have been assigned differently.

After having corrected the event picking, the correlation analysis shows an over all good correlation between the sensors as seen in for example site 75 in Figure 6.11.

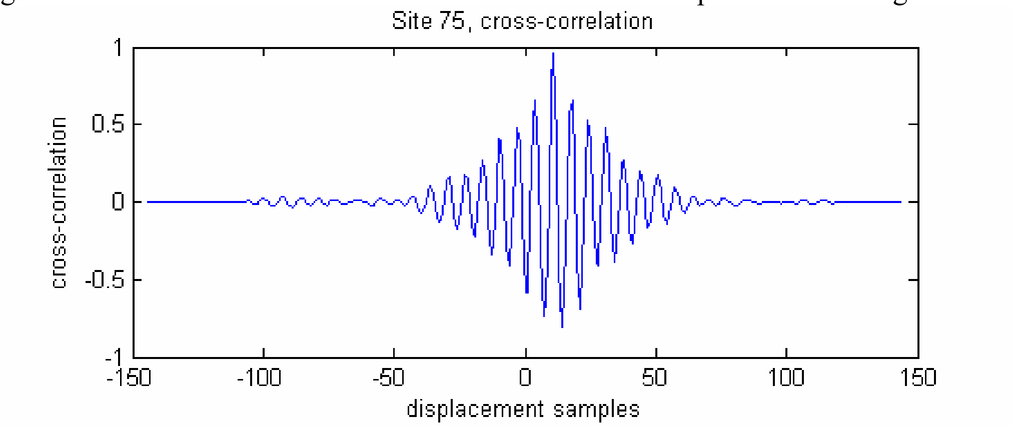

Figure 6.11 Cross-correlation between response signal of tri-axial accelerograph and uni-axial acclerometer

The autocorrelation of a signal at zero lag is one. Thus a correlation of one means

perfect positive correlation, while a correlation of -1 means perfect negative correlation. Zero correlation means there is no correlation at all between the signals.
With the exception of five sites the max correlation is close to unity in all the sites. Therefore the conclusion is that, from the same event, vertical acceleration recorded either on the tri-axial accelerograph or the uni-axial accelerometer can be used for further evaluation, without any considerable recorder bias.

6.3 Site spectrograms

The site impulse responses are now represented as spectrograms to see whether resonance frequencies can be seen directly from the plots as explained in section 5.4.5. It was an hypothesis before carrying out the field work that such resonances could be read directly from the spectrogram and even that the damping might be estimated with the half-power bandwidth method, or some other method for evaluating attenuation described in section 4.2.3.
A window length of 128 samples is chosen for the uni-axial accelerometer measurements and of 64 samples for the tri-axial accelerograph. The window lengths are chosen differently because the uni-axial measurements have double the sample rate of the tri-axial measurements. In time this represents a 0.25 second window, which means that frequencies down to 4 Hz can be detected (section 5.4.6). The window length is chosen considering both the lower frequency threshold and the time resolution. A 0.25 second window gives a reasonable resolution in time and still the lower frequency threshold is most probably below the surface layer resonance peak.
Most sites exhibit no clear prevailing frequencies. The impact from a truck at site 27 is taken to represent a typical spectrogram image from a good quality vehicle impact (Figure 6.12). The power is represented on a decibel scale of colours, with dark red representing highest spectral power and dark blue the lowest.

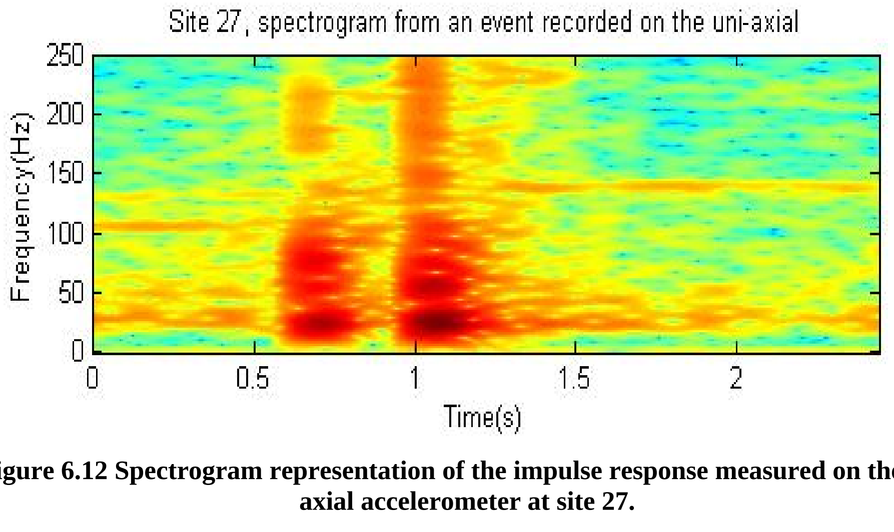

Figure 6.12 Spectrogram representation of the impulse response measured on the uni-axial accelerometer at site 27.

The impact is distinct and emits power in a wide frequency band all the way down to around 5 Hz, but no prevailing frequencies can be seen in the impulse response.

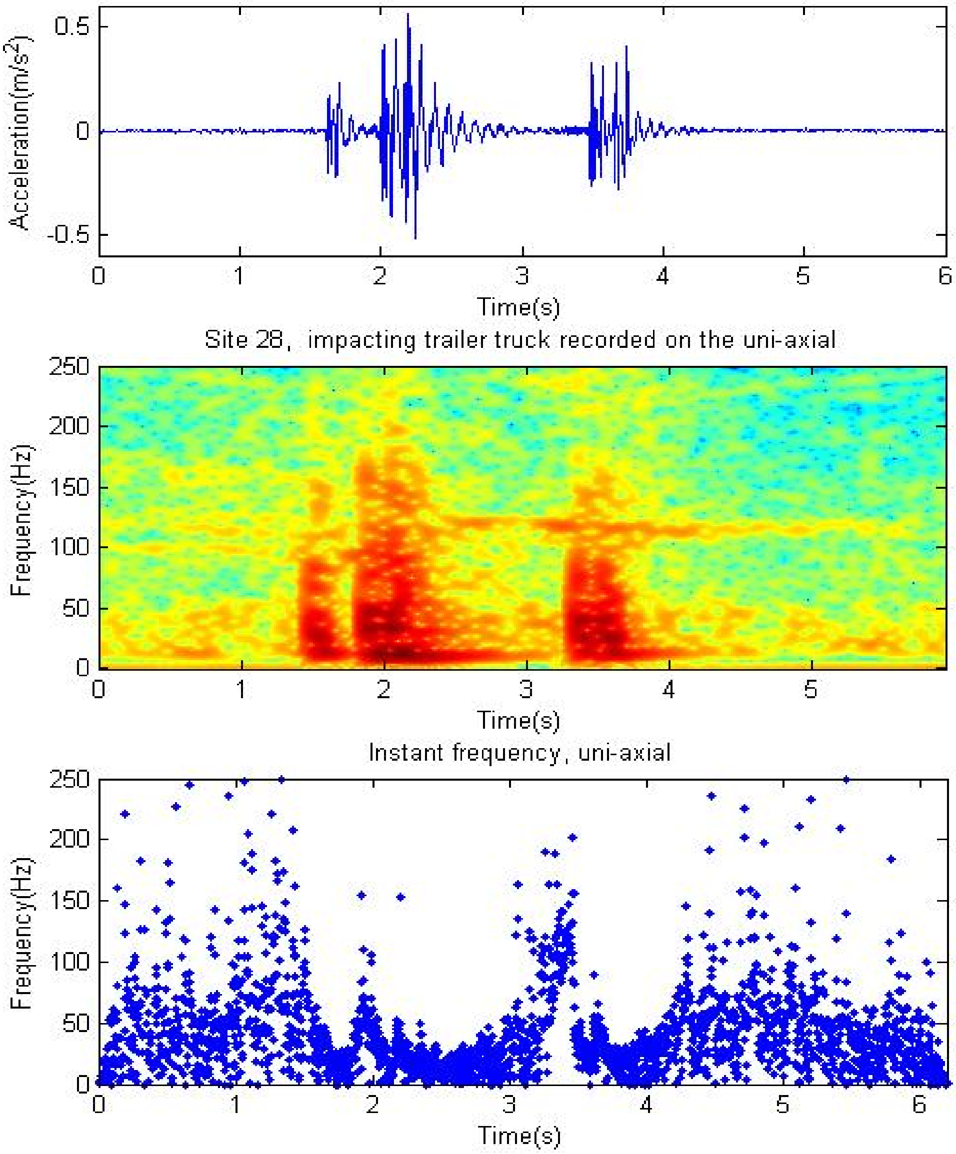

Figure 6.13 Top: Acceleration of the impulse response measured on the vertical axis at site 28. Middle: Spectrogram representation of the impulse response. Bottom: Instant frequencies of the impulse response history.

Some sites exhibit prevailing frequencies in the spectrogram representation of the impulse response, of which site 28 is the one showing the clearest prevailing frequency. The recording on the uni-axial accelerometer of a trailer truck impacting the obstacle at site 28 is represented as a spectrogram in Figure 6.13. The vehicle passage consists of the impact of the first axis of the tractor, then the double impact of the tractor boggie, and finally the boggie of the trailer. It is seen that around 10 Hz the impulse response clearly takes much longer time to be attenuated than at other frequencies in the impulse response, which implies a resonance frequency there.

The instant frequency plot in the same figure shows that the frequency content of the signal narrows down around the supposed resonance frequency immediately after impact and then regains its normal noise distribution gradually, as the impulse response is attenuated. As mentioned in section 5.4.5 on page 68 the instantaneous frequency is calculated from the angular difference between two successive sample points.

Picking out only the event produced by the tractor boggie of the trailer truck at site 28, which shows the strongest prevailing frequency in Figure 6.13, the spectrogram representation becomes like in Figure 6.14. The time lag between the signal and its spectrogram is due to that the frequency content calculated at a window position is assigned to the start sample point of the window. This will cause a time lag of approximately half a window length. In this figure the slow decay of spectral power due to resonance at the frequency 10 Hz is clear.

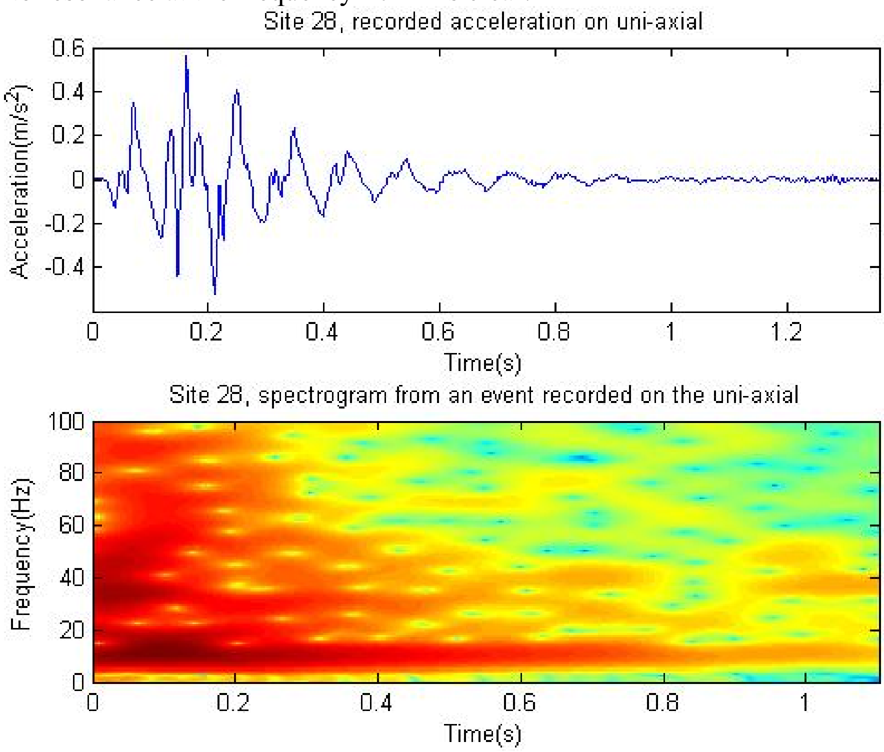

Figure 6.14 Spectrogram representation of a single event from site 28 and its aftermath. Top: Measured acceleration. Bottom: Spectrogram.

The same impulse response measured on the three axes of the accelerograph can be seen in Figure 6.15. These show more background noise, due to the accelerograph being more sensitive. On both the z-axis and the y-axis the same resonance frequency at 10 Hz is evident, although more pronounced on the z-axis.
The x-axis spectrogram shows less spectral power in the low frequencies and the prevailing signal in the area of 10 Hz is not seen (Figure 6.15). This can be seen in light of the less powerful signal generally registered on the x-axis. It is probably the

case that the dominating frequency power of the impact misses the resonance frequency.
In both the spectrogram obtained from the y-axis acceleration and the x-axis acceleration clear bands of ambient noise are present around the frequencies of 50 and 75 Hz.

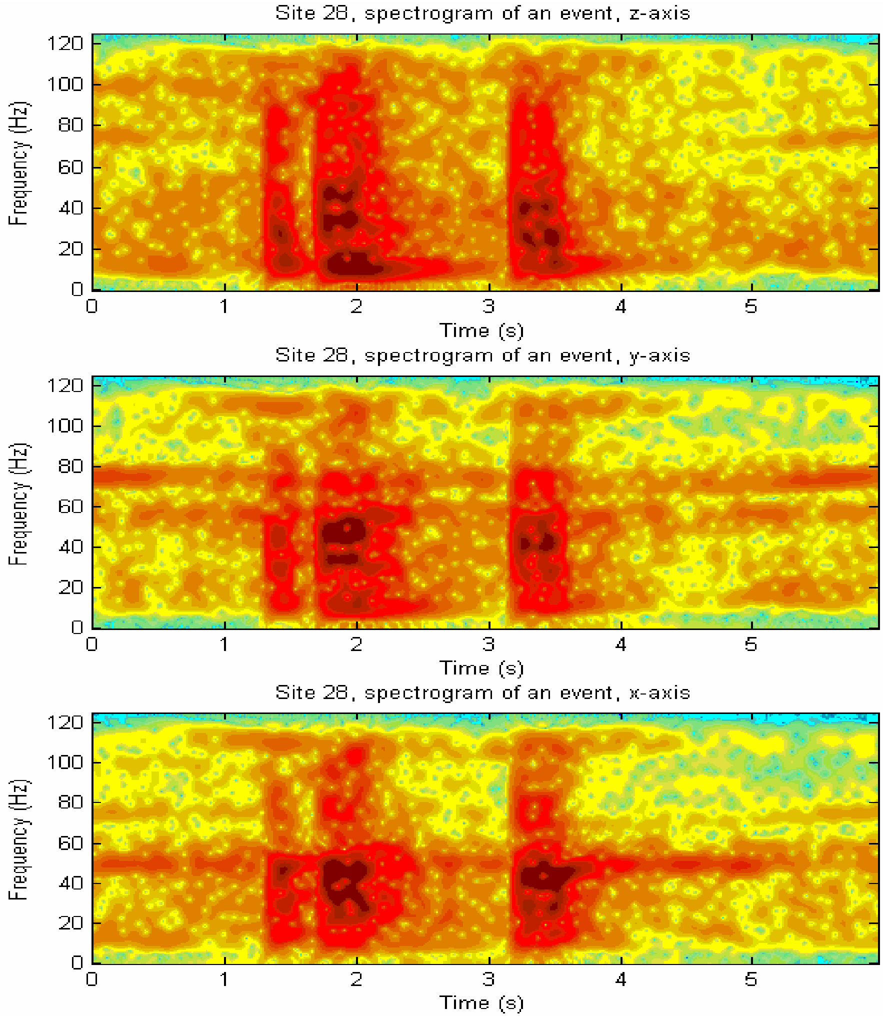

Figure 6.15 Spectrogram representation of the impulse response measured on the accelerograph at site 28. Top: z-axis. Middle: y-axis. Bottom: z-axis.

Figure 6.16 shows only the event produced by the tractor boggie. Notice the similarity between the recording on the accelerograph z-axis and the recording on the uni-axial accelerometer shown in Figure 6.14. This confirms the good correlation between sensors found in section 6.2. In this figure it is seen that the 10 Hz resonance shows clearest on the z-axis, while it is missing on the x-axis recording.
Other sites that exhibit a prevailing frequency around 10 Hz in the spectrograms, are site 87, 99, 115 and 116, although not as clear as is the case of site 28.

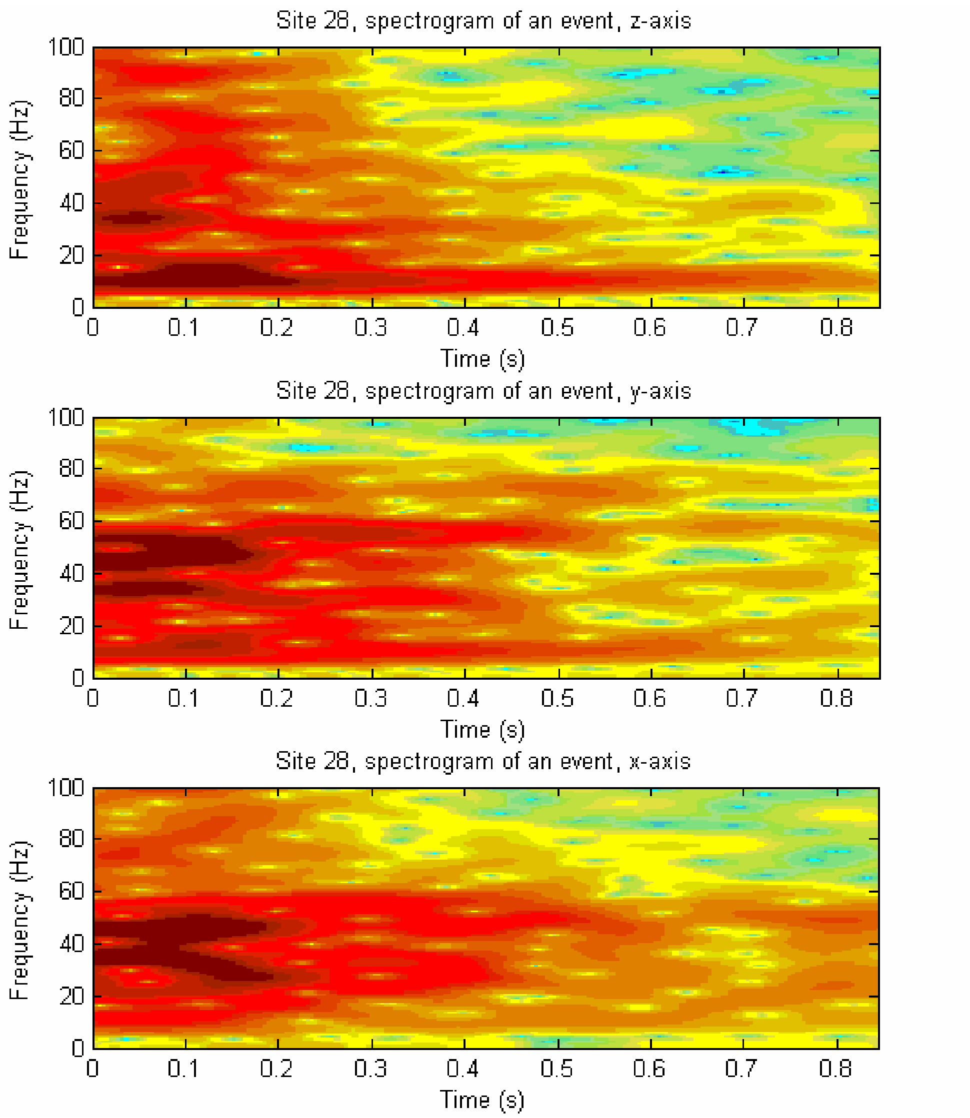

Figure 6.16 Spectrogram representation of a single event from site 28 recorded on accelerograph. Top: z-axis. Middle: y-axis. Bottom: x-axis.

If we look at the power spectrum over the entire event, i.e. the impact of a wheel axis and its aftermath, the dominant frequencies are perhaps easier identified. In Figure 6.17 the spectral power below 25 Hz of the impulse response at each frequency is shown, as we are advancing along the Pan-American Highway. On the horizontal axis is the frequency and on the vertical axis is the distance along Pan-American Highway. The spectral power of the impulse response is shown on a greyscale where black represents most power. The impulse response is low-pass filtered at 25 Hz before a Welsh spectral estimate is applied. This is to see what peaks are present in the frequency area where the earthquake contains considerable power (as seen in Figure 5.20). Anyhow the earthquake spectrum is limited at 25 Hz, due to the sample rate at

50 Hz which gives the Nyquist frequency 25 Hz[2]. The reason of one site exhibiting spectral power above 25 Hz in the figure is due to an error in assigning the sample rate of the signal analyzed.

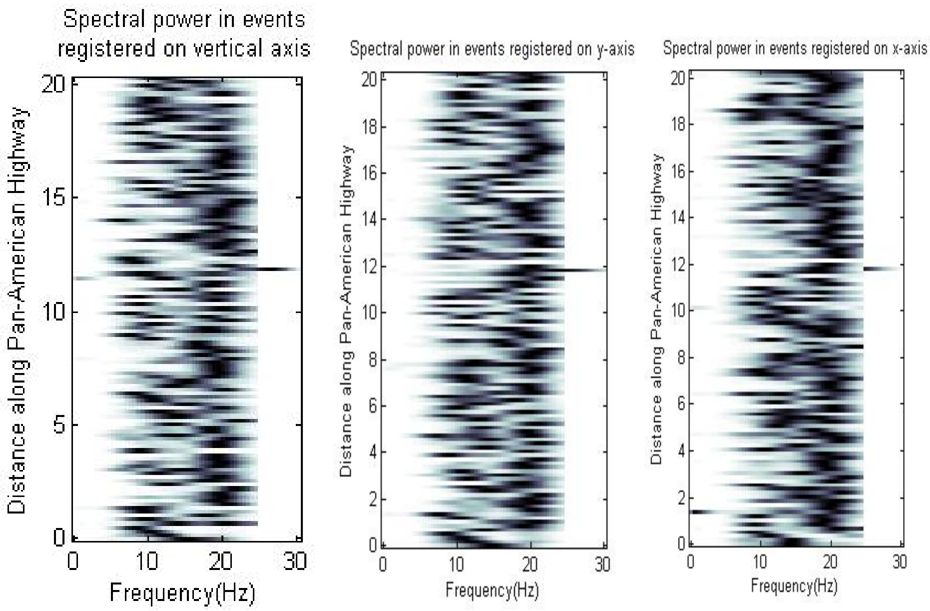

Figure 6.17 Normalized spectral power along the Pan-American Highway for vertical axis, y-axis and x-axis.

It can be seen from the figures that sites with a spectral peak of around 20 Hz dominates. Some sites exhibit peaks at lower frequencies down to 10 Hz and even lower. Compare this to the resonance frequency at 9 Hz of the building used as an example in this study.

The peaks appearing in these diagrams should not be taken directly as resonance frequencies as they reflect the spectral content of the event as a whole, which is therefore in part source-inherent. They do however give an idea on what predominant frequencies the surface layers along the Pan-American Highway give rise to.

Even if the spectrograms of most sites exhibit no resonances, five sites, of which site 28 is the clearest, show that the impulse response prevails at a frequency. This proves that resonance amplification will appear in the spectrogram. The soils of Managua are generally competent and the fact that no prevailing resonances can be seen in most spectrograms is probably because none occur.

Nonetheless, in view of the general absence of resonance in the spectrograms, the time-frequency hazard analysis has been developed for a non biased evaluation of the earthquake-sensitivity of a site.

[2] The Nyquist frequency is the upper detectable frequency with no risk of aliasing. For a description of aliasing see for example (Randall and Tech, 1997).

6.4 Seismic risk zonation along the Pan-American Highway

In order to evaluate the local risk the time-frequency hazard analysis is applied using the measured impulse responses along the Pan-American Highway. The theory behind it is explained in section 5.5.
First in this chapter is a section showing how resonances and attenuation affects the local risk. In section 6.4.2 an estimate of the local risk along the Pan American Highway is taken forth.

6.4.1 Resonance and attenuation

The time-frequency hazard analysis takes into account both resonance frequencies and attenuation of the surface layers, without having to rely on subjective interpretation. It measures the decay of the integrated amplitudes over the frequency spectra. That is, the attenuation of instantaneous risk for a specific building. As explained in section 5.5.1 the instantaneous risk is obtained from the sensitivity spectrum which is the convolved earthquake, site response and building spectra.
As it cannot be determined what wave types are registered on each axis, all of the axes are used in the hazard analysis. This will show how the results differ from one another. The x-axis in several cases shows bad signal to noise ratio as the accelerations registered are generally lower than on the y-axis and z-axis. This is due to a less powerful impulse given by the vehicles in that direction, as seen in section 5.2.2 and 6.1. But the impact generated horizontal shear wave it probably registers is interesting and thus an evaluation is attempted anyway.

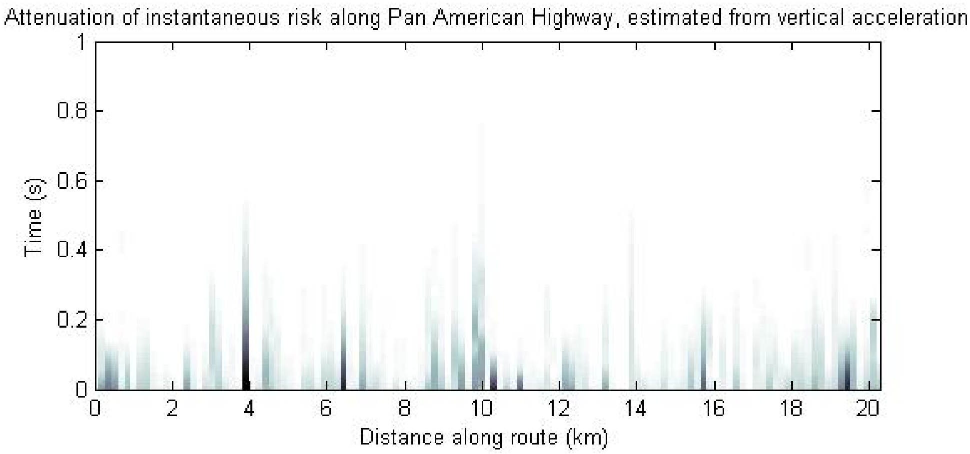

Figure 6.18 Attenuation of instantaneous risk estimated from vertical acceleration.

The attenuation of instantaneous risk estimated from the vertical axis is shown in Figure 6.18. On the horizontal axis is the distance along the Pan American Highway and on the vertical axis is the time elapsed since the impact peak. Km zero is where the first measurement site is, a little to the east of the international airport (see Appendix 1). The instantaneous risk is shown on a greyscale, where black represents high instantaneous risk and white low instantaneous risk.
It can be seen that around km 4 there is a very powerful instantaneous risk that takes a long time to die off. This is at site 28 in front of the supermarket "Palí" on carretera

norte (The part of Pan-American Highway from the city centre and eastwards), which was shown in section 6.3 to have prevailing oscillations around 10 Hz (Figure 6.13). Also around km 10 there is an area where the instantaneous risk takes a long time to be attenuated. Over all there are very local high instantaneous risks, perhaps in connection to water channels and faults. The connection with geomorphology will be treated in section 6.5.

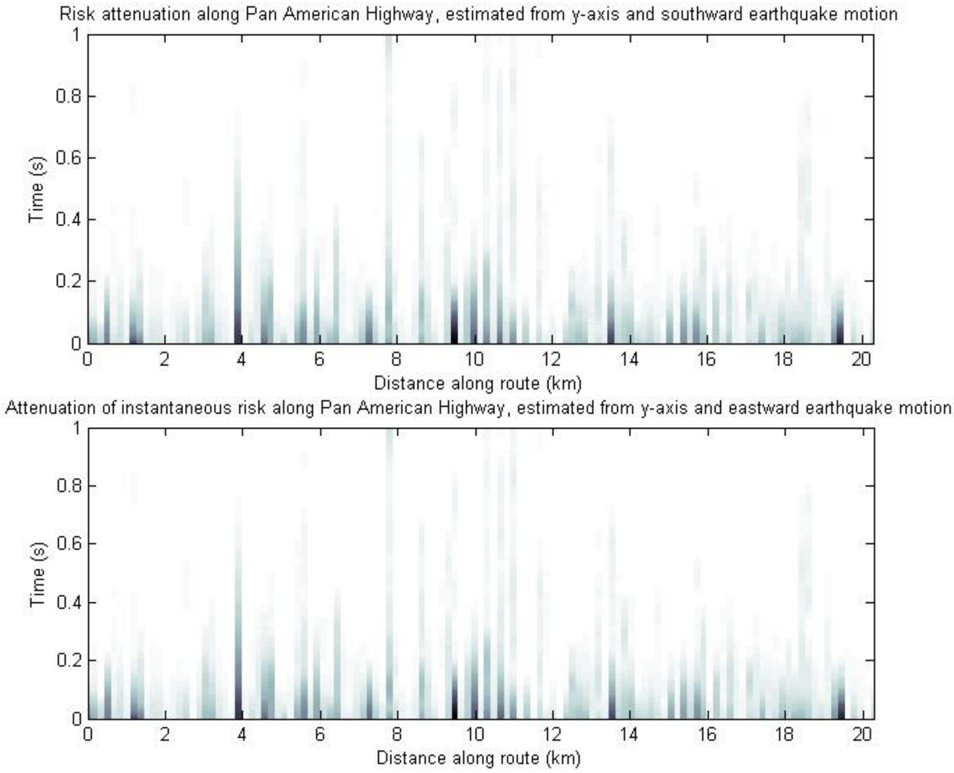

Figure 6.19 Attenuation of instantaneous risk estimated from y-axis and convolved with (above) southward earthquake acceleration and (below) eastward earthquake acceleration.

In the horizontal motion there are two earthquake input motions to choose from. The horizontal acceleration from the 1972 earthquake was measured in southward and eastward directions. In the analysis both are used to provide objectivity in the resulting hazard estimate. The instantaneous risk attenuation estimated from the y-axis from convolving with both southward and eastward earthquake acceleration is shown in Figure 6.19.

As seen the result from convolving with the acceleration measured in the two different directions is practically identical.

This picture shows a different pattern, although the high instantaneous risk with low attenuation at km 4 (site 28) remains. It does have a lower attenuation than that estimated from the vertical acceleration though. That the instantaneous risk attenuation is lower can be seen generally along the route.

Another area of high instantaneous risk and low attenuation can be seen from around km 9.5 to around km 11, which corresponds to the area where the former city centre was located. A zone of high instantaneous risk just after km 19 is present in both Figure 6.18 and Figure 6.19.

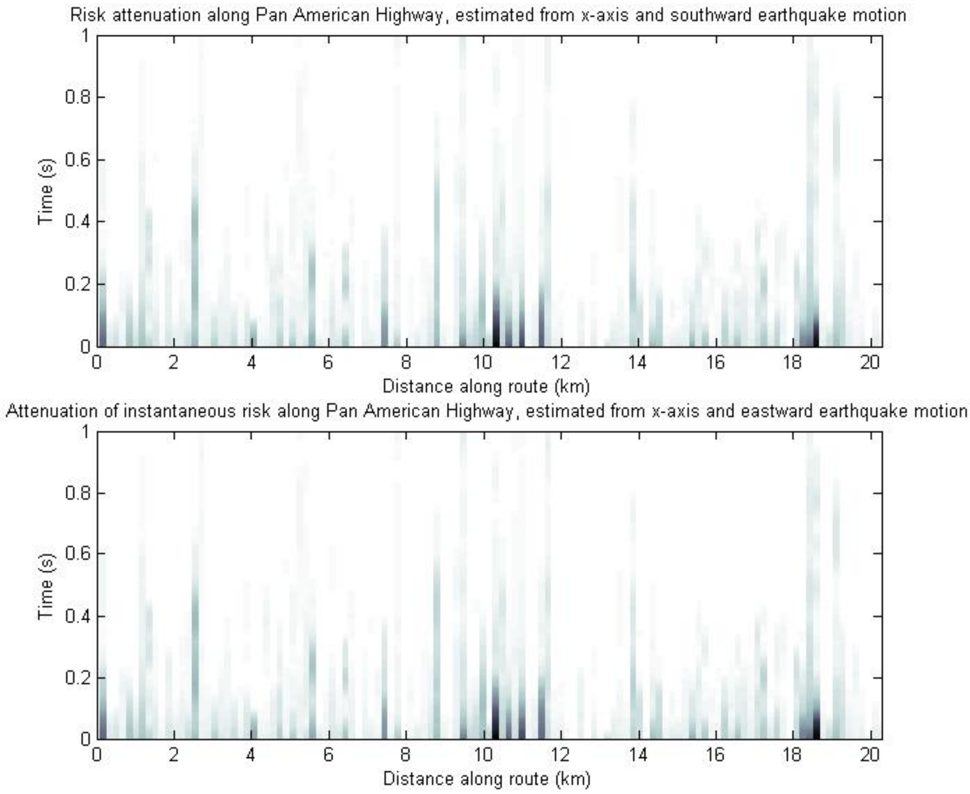

Figure 6.20 Attenuation of instantaneous risk estimated from x-axis and convolved with (above) southward earthquake acceleration and (below) eastward earthquake acceleration.

The instantaneous risk attenuation estimated from the x-axis is shown in Figure 6.20. The risk estimated from southward and eastward earthquake motion is practically identical, like in the case of the y-axis.
Again an area of high risk from around km 9.5 to 12, evident also in Figure 6.18 and Figure 6.19, can be seen. Another high risk area is present just after km 18.

Resonance causes the instantaneous risk attenuation to be lower, as does a low material damping. The lower the instantaneous risk attenuation is the more probable a build-up of wave amplitudes is in the case of an earthquake (section 4.3.2). Thus resonance in the surface layers in combination with low material damping causes high local risk.

6.4.2 Local risk

The local risk is here defined as the *double integral of amplitude over frequency and time:*

$$L = \iint A(f)\,df\,dt \qquad (6.1)$$

It is thus the integration of the instantaneous risk attenuation seen in Figure 6.18 to Figure 6.20, along the time axis. The local risk index is obtained by multiplying the local risk with a factor of 1000 (see section 5.5.2) in order to have figures more easily related to. It is a purely relative index of earthquake-sensitivity. The variation in local risk along the Pan American Highway, estimated from vertical acceleration is shown in Figure 6.21. On the horizontal axis is the distance along the Pan American Highway and on the vertical axis the local risk index can be read.

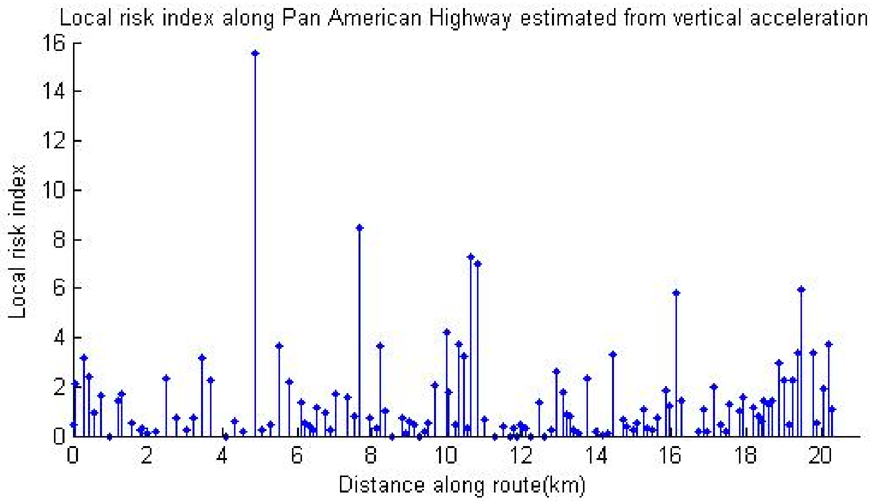

Figure 6.21 Local risk index along Pan American Highway.

Site 28 stands out around km 4 again. Then there is a zone of higher risk around the former city centre and another at the end of the route, close to the south western city limit. Other than that there are local high risk indices present.

The local risk estimated from the acceleration measured on the y-axis is shown in Figure 6.22. Only the local risk obtained from convolving with the southward measured earthquake acceleration is shown, as the one convolved with the eastward acceleration is practically identical, which was also seen in Figure 6.19. They can all be seen in Appendix 4.
The local peak of site 28 is again present. Then between km 6 to km 12 passing the city centre the values change between high risk indices and low risk indices with an area between 10 and 12 km with high local risk. This is in the area of the former city centre.

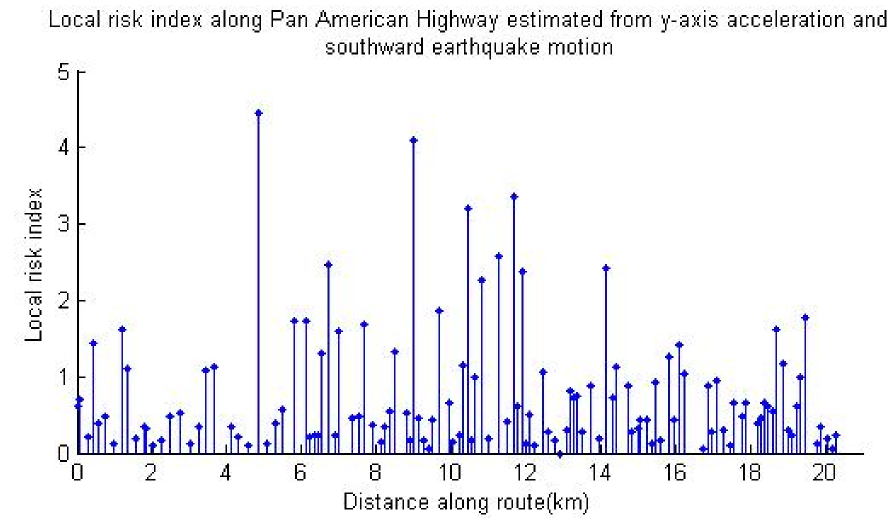

Figure 6.22 Local risk evaluated from y-axis acceleration, convolved with southward measured earthquake acceleration.

In Figure 6.23 the local risk estimated from the x-axis is shown. Care should be taken when interpreting these values as the signals registered are quite weak and the criteria of dwarfing ambient noise is poorly fulfilled. The peak present in the vertical axis and the y-axis corresponding to site 28 is not present. This was expected as the impulse response recorded on the x-axis on site 28 exhibits no prevailing frequencies, contrary to the z- and y-axis (Figure 6.16).

The area of high risk around the city centre is present also here however. At the end of the line is another high risk zone which is also seen in all the previous figures.

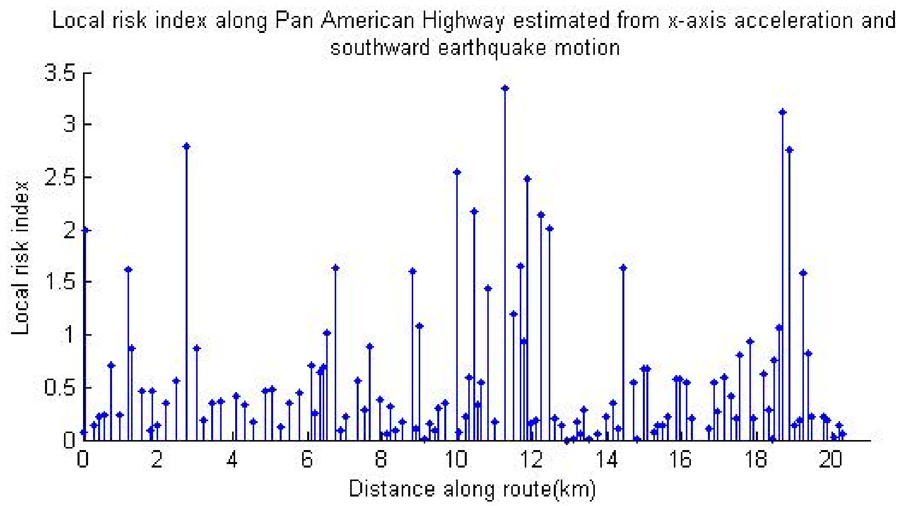

Figure 6.23 Local risk evaluated from x-axis acceleration, convolved with southward measured earthquake acceleration.

These pictures confirm the image given by the figures of instantaneous risk attenuation. There is a couple of very local high risk zones and then two larger high risk zones between km 10 to 12 in the city centre, and at the end of the route close to the south western city limit from around km 18 to km 20.

A more general estimation of local risk is obtained by averaging the local risk obtained from the impulse response measured on the different axes of the accelerograph (Figure 6.24).

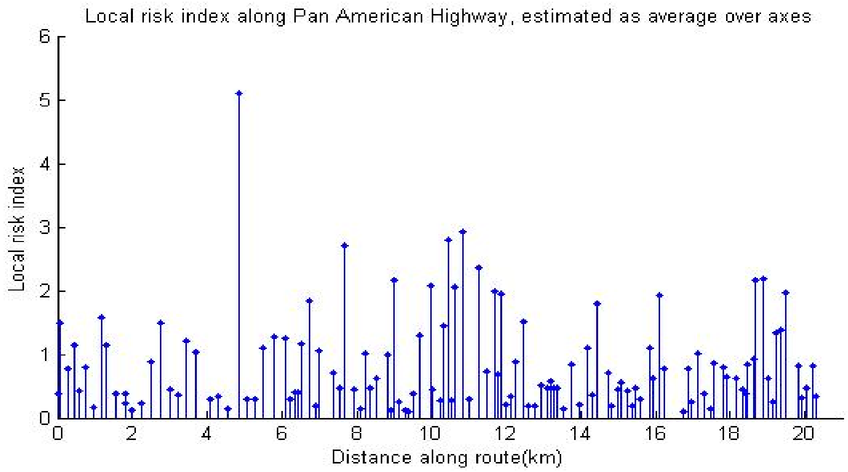

Figure 6.24 Local risk obtained as an average between directionally computed local risks.

Here we see the very local high risk obtained from the impulse response at site 28. The city centre between km 10 and 12 is a high risk zone and a segment after km 18 also give high risk indices. Outside these areas the local risk index varies with some very local high risk sites.

6.5 Correlation between results and geomorphology

It has been assumed before carrying out the field work that the most earthquake-sensitive sites is to be found close to Lake Xolotlán, where sediment thickness due to surface runoff would be greatest. It has also been a hypothesis that sediments would be thickest in the vicinity of faults, and where water flows. The presence of faults and water channels is probably related in most cases.

The local risk estimated from vertical impulse response and plotted as we go along the Pan-American Highway can be seen in Figure 6.25. The water channels and streams crossing the route are also traced out.

There seems to be a concurrence in where high risk is found and where water flows crosses the route, although the highest peaks are not where water flows are present.

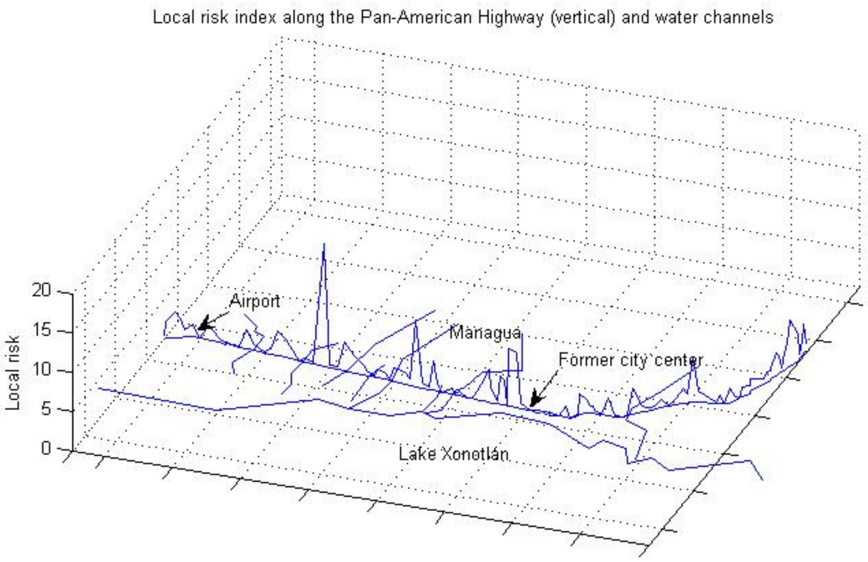

Figure 6.25 Local risk estimated from impulse response registered on the vertical axis plotted along the Pan-American Highway, with the tracing of water channels and streams marked.

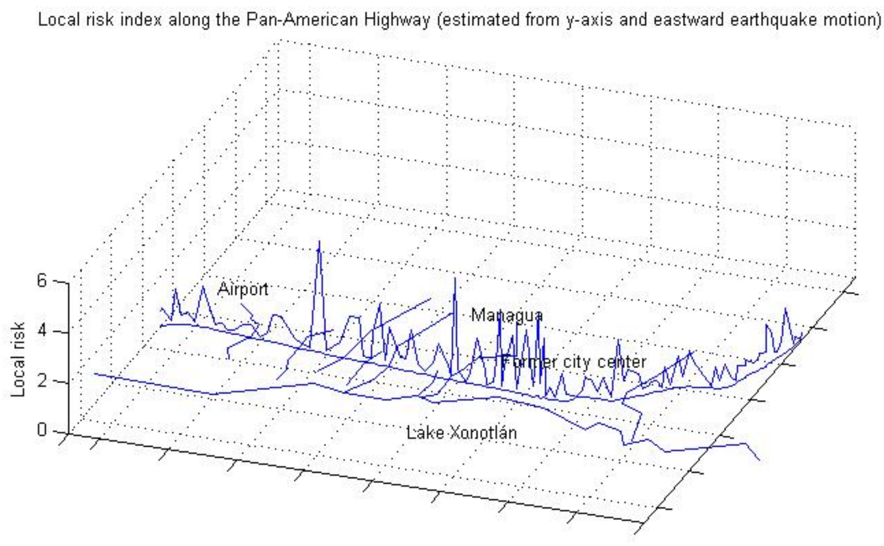

Figure 6.26 Local risk estimated from the impulse response registered on the y-axis plotted along the Pan-American Highway, with the tracing of water channels and streams marked.

In Figure 6.26 the local risk estimated from the impulse response of the horizontal y-axis is shown.

In this picture it is clearer that the peaks in local risk occur where the water flows are. Also worth noticing is high local risk in the city centre, close to the waterline of Lake Xolotlán.

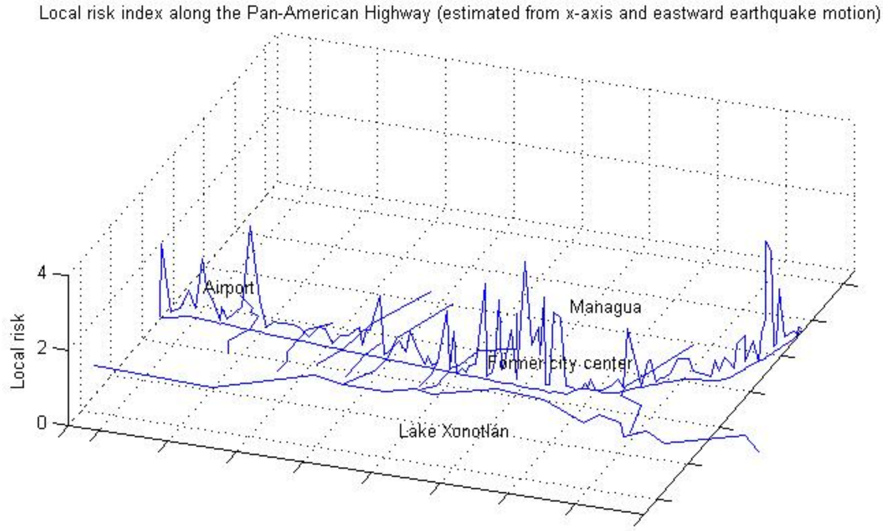

Figure 6.27 Local risk estimated from the impulse response registered on the y-axis plotted along the Pan-American Highway, with the tracing of water channels and streams marked.

The local risk estimated from the measured x-axis acceleration (Figure 6.27) confirms the high risk in the city centre, but exhibits a quite different pattern otherwise. Again peaks in local risk coincide with water flows.
It is repeated that the x-axis impulse response shows much weaker accelerations, and it is questioned if it fully succeeds in the criteria of dwarfing ambient noise.

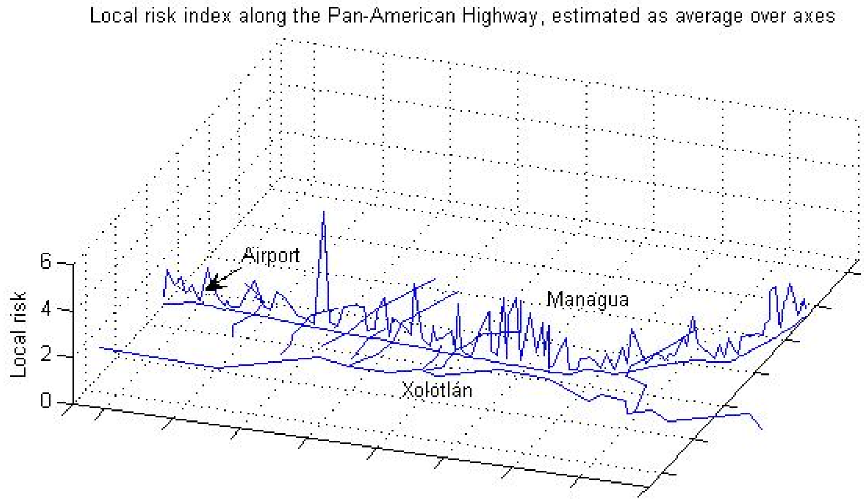

Figure 6.28 Averaged local risk plotted along the Pan-American Highway.

The average local risk is finally plotted along the route as shown in Figure 6.28.
Here it becomes evident that the local risk is greater in connection or close to water flows. The high local risk on the high ground at the end of the route may perhaps be explained by the fact that the road area is located in low ground passing between crests in the terrain. The surface runoff from the surrounding crests would then be concentrated here in its path towards Lake Xolotlán, with thicker sediments as a result.

7 Discussion

7.1 Assessment of the method

This study has been carried out to test the spectrogram evaluation of the traffic impulse response as a fast method of identifying earthquake-sensitive sites. It is emphasized that when these sites have been identified, more time-consuming techniques should be used for a better evaluation of the soil's dynamic parameters.

When analyzing the spectrograms only few sites show clear prevailing frequencies. The measurements at these sites, in combination with the ones carried out at Stortorget in Lund, prove that strong resonances will show in the spectrogram in the expected way.

A key issue is to assure measurements containing a strong impulse with low-frequency content and little ambient noise present. This is ideally a heavy vehicle coming in alone with no traffic around. A trailer truck or, in the case of Managua, a city bus loaded with people, provides good impulse characteristics. The single axis of the city bus provides a more distinct impact than the boggie of the trailer truck, and gives no risk of stimulating any particular frequency.

An excellent idea, which is attributed to Roger Blándon, is to carry out measurements early in the morning (four or five o'clock). At this time the truck drivers have already started their working day but few small vehicles traffic the streets.

Figure 7.1 Gate standing tall in the 1972 earthquake.

The use of the time-frequency hazard analysis results in a measure of local risk which should provide a correct estimate. The key issue is again that the impulses measured fulfil the criteria of dwarfing ambient noise and having low-frequency content. It is crucial that the impulses recorded all show good quality so that the impulse response can be considered non-biased and does not miss the fundamental frequency of the surface layers.

At several sites in this study it has been troublesome to obtain good quality records, due to high levels of ambient noise or little heavy traffic. This may affect the local risk obtained through the time-frequency hazard analysis.

This leads to a limitation of the technique. It has to be carried out along routes with high levels of heavy traffic, but with sufficiently low traffic levels to allow the vehicles pass at high speed. Again the ideal is to carry out the measurements in the morning hours when these criteria will be fulfilled and little microtremor is present.

A concern is that the impulses given by the vehicles have too little frequency content at low frequencies, and it may be the case that the impulse response measured misses the dominating frequency content of the earthquake as seen in Figure 5.20. But with the layered and rather competent structure of the surface layers it is not probable that they exhibit resonance peaks at such low frequencies. Furthermore the two-story building that is used as an example in this study exhibits a fundamental resonance frequency at 9 Hz. Almost all houses in Managua are single-story, and would not exhibit resonance peaks any lower than that. The bigger complexes may exhibit resonance peaks at lower frequencies.

Figure 7.2 This high-rise building has been raged by fire in the 1972 earthquake.

The accelerations measured on the different axes of the tri-axial accelerograph provide diverse information. The vertical axis and the y-axis show similar peaks, but the x-axis shows much lower peak acceleration.
The spectrograms obtained from the vertical axis and y-axis are also similar, while the ones obtained from the x-axis are much less clear.
When put into the time-frequency hazard model the instantaneous risk evaluated from the y-axis takes longer time to be attenuated than the vertical axis. The local risk obtained from them shows different patterns, while the x-axis concurs quite well with the y-axis in the local risk indices obtained. However, the quality of the x-axis acceleration records is generally too poor to be relied on.
The similarity in peaks of vertical and y-axis acceleration may suggest that their peak can be attributed mainly to Rayleigh wave content.
The x-axis is believed to register mainly S-wave content and its similarity to the risk attenuation and local risk estimated from the y-axis suggests that the impulse response measured on the y-axis can also be attributed largely to S-waves. This would render the acceleration on the y-axis the candidate for evaluation of shear wave resonance.
This conclusion is further enhanced by the fact that as to S-wave vertical resonances, the vertical axis is less apt as it is probable to register mainly standing P-waves. Vertically polarized S-waves registered on the z-axis are direct and do not create

resonance in the surface layers. The acceleration registered on the x-axis is simply to low to securely fulfil the criteria of ambient noise dwarfing.

It is seen from the above that the uni-axial accelerometer alone does not measure the complete impulse response. Shear waves are probable to be registered mainly on the two horizontal axis, and thus the uni-axial accelerometer will measure mainly Rayleigh wave content and P-wave resonances in the surface layers.

A source of uncertainty is the road fill overlying the surface layers. It is possible that horizontal Lamb wave resonances can occur in the road body. The lamb wave resonances are then incorrectly attributed to the impulse response of the surface layers. The lamb waves are surface waves propagating in thin media working as wave guides.

Another question raised is to whether the acceleration measured is both the impulse and the ground response or if it is just the ground response. It is not known whether the first peak in the spectrogram can be considered the frequency content of the impulse, and the decay of it the ground response. It is probable that this is so because of the closeness of the sensors to the source.
A way to be sure to register also the unfiltered impulse from the vehicle would be to locate another accelerometer inside of the rubber cable protector. This way the transfer function could also be determined by deconvolving the impulse spectrum measured by the cable protector mounted accelerometer from the ground response spectrum measured by the tri-axial accelerograph on the side of the roadway. For example the Piezotronics Model 3703G2FD3G tri-axial accelerometer first intended for this study could be used for this purpose, if made to work in connection with a recorder.

7.2 Further Studies

The data collected from the measurements recorded along the Pan-American Highway is far from exhausted. In this study the evaluation of noise recordings carried out at the same sites as the impulse response recordings is not done at all. If these can be said to consist of microtremors the Nakamura Technique can be applied to them and another independent estimate of resonance peaks and amplification of surface layer is obtained. This can be compared to the results from the spectrogram evaluation technique and its validity be tested.
As seen in the discussion on which type of waves are emitted from the vehicle impact, further investigation is needed.
The type of waves emitted can be looked at by locating an array of geophones at one of the measurement sites in straight lines parallel and perpendicular to the direction of traffic. Then Multi-channel Analysis of Surface Waves (MASW) can be done, and the content of different wave types in the impulse response clarified.

8 Conclusions

The conclusions that can be drawn regarding the Spectrogram Evaluation Technique are:

- Vehicles used as seismic source need to be heavy in order to create an impact with power in the low frequencies. The vehicles should be isolated with no other vehicles coming in at the same time in order to create a distinct impact that dwarfs the ambient noise. Multiple wheel axes may stimulate a frequency with period corresponding to the distance between axes. Using the impact from the last wheel axis is preferable, as the whole decay of the signal can be recorded and the noise floor, after the signal has died out, can be removed from the impulse response. The city busses of Managua meet these criteria excellently as they have a single, very heavily loaded, rear axis. Furthermore it is recommended to measure the impulse responses early in the morning (three, four or five o'clock) as there is a lot of heavy traffic but few smaller vehicles and little ambient noise present at these hours.

- If the above criteria are met, strong fundamental resonance peaks will be detected by analysing the traffic impulse response with the spectrogram method. The measurements on site 28 (Figure 6.13) and on Stortorget in Lund (Figure 5.18) proves this.

- A further understanding on the type of waves emitted from the source vehicle is needed. This can be investigated by for example placing an L-shaped array of geophones and analysing the waves measured with MASW (Multichannel Analysis of Surface Waves).

- Tri-axial measurements provide information on the vibration which uni-axial measurements do not contain. It is probable that a single vertical accelerometer detects mostly P-wave resonances.

Conclusions to be drawn regarding the time-frequency hazard analysis are:

- The time-frequency hazard analysis provides an integrate measure of resonances and attenuation, without any subjective interpretation.

- The best estimate on shear wave resonance is probably obtained from the horizontal y-axis of the tri-axial accelerograph.

- Special care should be taken as to whether the impulse response measured covers the relevant frequency band and do not miss the resonance frequencies in the surface layers. The impact measured must contain power at low frequencies in order to detect a fundamental resonance frequency.

- The method should be validated by carrying out microtremor analysis with the Nakamura method (or another suitable method) on some of the noise recordings that were done at each site, to see if the estimates on where the local risk is greatest concur.

Figure 8.1 Destruction in the city centre after the 1972 earthquake.

9 References

Anderson, G., "Lecture 11-Global Seismology", http://topex.ucsd.edu/es10/lectures/lecture11/lecture11.html.

Anton, D.J., "Ciudades Sedientas-Agua y ambientes urbanos en América Latina", http://web.idrc.ca/es/ev-9313-201-1-DO_TOPIC.html.

CIA, "Nicaragua (Shaded Relief)", http://www.infoplease.com/atlas/country/nicaragua.html.

Clark, S.P., 1966, "Handbook of physical constants": New Haven, Connecticut, The Geological Society of America.

Cowan, H., Machette, M.N., Amador, X., Morgan, K.S., R.L., D., and Bradley, L., "Map and Database of Quaternary Faults in the Vicinity of Managua, Nicaragua", http://pubs.usgs.gov/of/2000/ofr-00-0437/ofr-00-0437pamphlet.pdf.

Craig, P.F., 1997, "Soil mechanics", E & FN Spon, 485 p.

Ekholm, P., and Norberg, O., 1998, "SASW measurements in Managua, Nicaragua" [Masters thesis thesis]: Stockholm, Kungliga Tekniska Högskolan.

Field, E.H., Johnson, P.A., Beresnev, I.A., and Zeng, Y., 1997, "Nonlinear ground-motion amplification by sediments during the 1994 Northridge earthquake": Nature, v. 390, p. 599-601.

Field, E.H., Kramer, S., Elgamal, A.W., Bray, J.D., Matasovic, N., Johnson, P.A., Cramer, C., Roblee, C., Wald, D.J., Bonilla, L.F., Dimitriu, P.P., and Anderson, J.G., "Nonlinear site response", http://www.scec.org/instanet/newsletter/39nonlinear.html.

French, C.D., and Schenk, C.J., "Map Showing Geology, Oil and Gas Fields, and Geological Provinces of the Caribbean Region", http://certmapper.cr.usgs.gov/data/test/graphic/caribzoom.html.

Gade, S., and Herlufsen, H., 1994, "Digital Filter Techniques vs FFT Techniques for Damping Measurements", *in* Kjaer, B.

Gazetas, G., 1982, "Vibrational characteristics of soil deposits with variable wave velocity": International Journal for numerical and analytical methods in geomechanics, v. 6, p. 1-20.

Hernández-Rubio, O.U.-M., 2005, "Reevaluación del efecto de sitio en Managua, Nicaragua" [{unpublished} MSc thesis]: Managua, UNAN.

Incer Barquero, J., Wheelock Román, J., Cardenal Sevilla, L., and Rodríguez, A.C., 2000, "Desastres naturales de Nicaragua - Guia para conocerlos y prevenirlos": Managua, HISPAMER.

Kinemetrics, "Earthquake and Seismic Monitoring", http://www.kinemetrics.com/products.asp.

Kious, W.J., and Tilling, R.I., "This Dynamic Earth:The Story of Plate Tectonics", http://pubs.usgs.gov/publications/text/dynamic.html.

Knopoff, L., 1964, "Q": Reviews of Geophysics, v. 2, p. 625-660.

Lapiedra, J.M., "Utilities related to the world of geotechnics", http://www.jordimoreno.com/extras.htm#9.

Mahin, S.A., "An Interactive Course in Earthquake Engineering", http://peer.berkeley.edu/~jrodgers/.

Nakamura, Y., 2000, "Clear Identification of Fundamental Idea of Nakamura's Technique and its Applications".

Parrales Espinoza, R.M., 2004, "Different definitions of energy dissipation in geological materials".

Parrales Espinoza, R.M., and Picado Romero, M.J., 2001, "Análisis de espectros de respuesta en el área de la ciudad de Managua" [MSc thesis]: Managua, Universidad Nacional de Ingeniería.

Piezotronics, P., 2002, "Model 393A03 Piezoelectric Accelerometer-Installation and Operating Manual", PCB Piezotronics-Vibration Division.

Randall, R.B., and Tech, B., 1987, "Frequency analysis": Glostrup, Denmark, Brüel & Kjaer, 344 p.

Rey, P.F., 2003, "Faults, Folds and Mountain belts", School of Geosciences, Division of Geology & Geophysics, The University of Sydney, NSW

2006, Australia., http://www.geosci.usyd.edu.au/users/prey/Teaching/Geol-1002/Geol1002.htm.

Richart, F.E., Hall, J.R., and Woods, R.D., 1970, "Vibrations of Soils and Foundations": Englewood Cliffs, New Jersey, Prentice-Hall, 414 p.

Rix, G.J., Lai, C.G., and Spang, A.W., 2000, "In situ measurement of damping ratio using surface waves": Journal of geotechnical and geoenvironmental engineering, p. 472-480.

Stål, F., and Westberg, G., 1996, "Microzonation Study in Managua, Nicaragua" [M.Sc. thesis]: Stockholm, Royal Institute of Technology.

Teves Costa, P., and Matias, L., 1995, "Seismic behaviour estimation of thin alluvium layers using microtremor recordings": Soil Dynamics and earthquake Engineering, v. 15, p. 201-209.

USGS, "Plate Tectonics and Hot Spot Images", http://earthsci.org/geopro/platec/plate.html.

Walther, C.H.E., Flueh, E.R., Ranero, C.R., von Huene, R., and Strauch, W., 2000, "Crustal Structure across the Pacific margin of Nicaragua: evidence for ophiolitic basement and shallow mantle sliver": Geophysical Journal International, p. 759-777, www.ineter.gob.ni/geofisica/tect/struct/sonne96/walther-et-al-en.html.

van Wyk de Vries, B., 1993, "Tectonics and Magma Evolution of Nicaraguan Volcanic Systems" [Unpublished Ph.D. thesis]: Open University, Milton Keynes, UK., http://www.margins.wustl.edu/PDF/vanwykdevries.pdf.

Appendix 1: Map over measurement sites

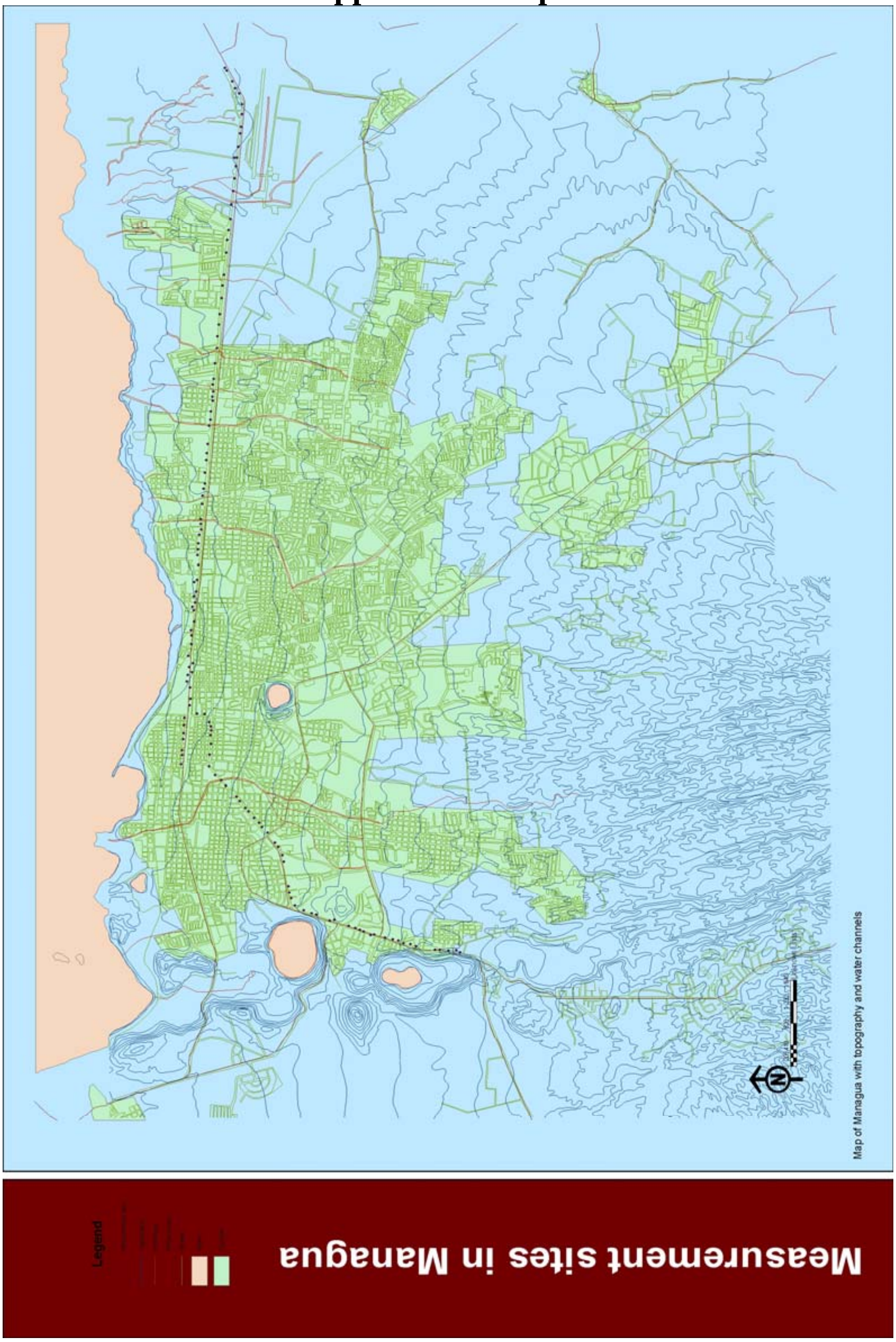

Appendix 2: Coordinates of measurement sites

SEQ_NO	SITE	COD	LOCATION	COORD_E	COORD_N	DISTANCE	CUM_DIST	NOTES	DIR__X
1	13	Jk2013	Zona Franca	591373	1342862	0	0		S43W
2	86	Jk2086	UNA - Fte Zona Franca	591325	1342832	57	57	en carretera	S51W
3	14	Jk2014	UNA	591114	1342728	235	292		S54W
4	87	Jk2087	UNA - Ent dormitorios	590984	1342678	139	431	en carretera	S60W
5	15	Jk2015	Fte Aeropuerto/UNA	590880	1342601	129	561	Acera opuesta	S61W
6	88	Jk2088	Fte Portón 10 Aeropuerto	590677	1342557	208	768	en carretera	S74W
7	16	Jk2016	Fte Portón 9 Aeropuerto	590480	1342552	197	965	Acera opuesta	Oeste
8	17	Jk2017	Hotel Las Mercedes	590249	1342570	232	1197	Antes del puente	S87W
9	89	Jk2089	Hotel Las Mercedes	590124	1342590	127	1324	en acera	N88W
10	18	Jk2018	Shell Aeropuerto	589868	1342618	258	1581	Fte Portón 6 Aeropuerto	Oeste
11	91	Jk2091	Fte entrada Fuerza Aerea	589659	1342683	219	1800	en carretera, al lado de cauce	N84W
12	90	Jk2090	Entrada Balneario Los Sábalos	589659	1342644	39	1839	en carretera, parada de Buses	Oeste
13	19	Jk2019	Esso Aeropuerto	589489	1342664	171	2010	Fte Club Fuerza Aérea	N86W
14	92	Jk2092	Muro blanco del Hotel Camino Re	589259	1342683	231	2241	en carretera, mucho viento	N84W
15	20	Jk2020	Puente Fuerza Aérea	589016	1342709	244	2485	Aproximac W	N87W
16	21	Jk2021	Entrada ppal Hotel Camino Real	588757	1342743	261	2747	Contg puente	N87W
17	22	Jk2022	Entrada serv Hotel Camino Real	588478	1342764	280	3026	Fte Portón 1 Aeropuerto	Oeste
18	93	Jk2093	Texaco	588264	1342792	216	3242	en carretera	N87W
19	23	Jk2023	Parada "Kentucky Las Mercedes"	588067	1342817	199	3441		N86W
20	24	Jk2024	La Subasta	587830	1342835	238	3678	Fte Comedor La Estancia	N88W
21	25	Jk2025	Fte Estac Policía La Subasta	587406	1342881	426	4105	Unos metros al oeste	Oeste
22	26	Jk2026	Salida SINTER/CONTEC	587201	1342903	206	4311		N87W
23	27	Jk2027	Fte EDT	586954	1342919	248	4559	Kativo, 50 m al este	N86W
24	28	Jk2028	Fte Palí Carret Norte	586646	1342949	309	4868	Acera opuesta	N89W
25	94	Jk2094	Corte Supremo	586450	1342969	197	5065	en acera	N86W
26	29	Jk2029	Entrada TANIC	586221	1342996	231	5296		S84W
27	30	Jk2030	Bocacalle Fte entrada Shell	586005	1343005	216	5512	Acera opuesta	N83W
28	31	Jk2031	Bahía parada de buses	585716	1343040	291	5803	Cruz Lorena, xx m al este	S84W
29	95	Jk2095	Pronica	585415	1343060	302	6105	en acera alta	N88W
30	32	Jk2032	Fte Island Taste	585308	1343074	108	6213	Fte Ant Mansión del Reggae	S88W
31	96	Jk2096	Fte Gemina	585177	1343073	131	6344	en acera alta	N84W
32	97	Jk2097	Fte Siemens	585073	1343084	105	6448	en acera	N87W
33	33	Jk2033	Frigoríficos de Carret Norte	585000	1343077	73	6521	Fte Laboratorios Ramos	Oeste
34	34	Jk2034	1a entrada Casa Pellas	584789	1343107	213	6735	Fte ENACAL	Oeste
35	98	Jk2098	Incesa	584638	1343120	152	6886	en acera	N84W
36	35	Jk2035	Unión Fenosa Portezuelo	584515	1343143	125	7011	Al pie del puente	S86W
37	36	Jk2036	Nabisco	584170	1343167	346	7357		Oeste
38	37	Jk2037	Oficentro Norte	583984	1343183	187	7544		N88W
39	99	Jk2099	Parmalat	583850	1343196	135	7678	en acera baja	W
40	38	Jk2038	Zona de parqueo Grupo Q	583608	1343218	243	7921		N86W
41	100	Jk2100	Coca Cola	583408	1343218	200	8121	en entrada al lado de carretera	N88W
42	39	Jk2039	Coca Cola	583306	1343246	106	8227		N89W
43	101	Jk2101	RARPE	583175	1343262	132	8359	en acera, al lado de cauce	S88W
44	40	Jk2040	Restaurante Rincon Chino	583016	1343269	159	8518	cerca cauce	S86W
45	41	Jk2041	Empresa Impasa	582724	1343290	293	8811	al lado de cauce	N88W
46	102	Jk2102	Antes de Polos de Desarollo	582630	1343290	94	8905	en acera	W
47	42	Jk2042	Programa Polos de Desaroll	582524	1343286	106	9011		N85W
48	103	Jk2103	Cifuentes Ferretería	582424	1343321	106	9117	en acera	S86W
49	43	Jk2043	ULAM	582260	1343333	164	9282	sensores en tierra	S86W
50	104	Jk2104	Ferretería Pastora	582139	1343340	121	9403	en carretera	N88W

Appendix 2: Coordinates of measurement sites

SEQ_NO	SITE	COD	LOCATION	COORD_E	COORD_N	DISTANCE	CUM_DIST	NOTES	DIR__X
51	44	Jk2044	Sistemas Aereos	582034	1343352	106	9508	en tierra	S88W
52	12	Jk2012	Estac Policía Ajax Delgado	581846	1343338	189	9697		S86E
53	11	Jk2011	Contg Aquatec	581569	1343359	278	9975	Dos tramos después	S88E
54	45	Jk2045	Frente Aquatec	581521	1343407	68	10043		N87W
55	10	Jk2010	Fte Ant La Perfecta	581339	1343375	185	10227	Acera opuesta	Este
56	46	Jk2046	Campo de Balloncesto de Co	581247	1343422	103	10331		W
57	9	Jk2009	Fte Ctro Esc Quinta Nina	581134	1343390	117	10448	Acera opuesta	S88E
58	47	Jk2047	Funeraria Oriental	581047	1343441	101	10549		S86W
59	8	Jk2008	Contg Ferret Bühler	580984	1343421	66	10615		S73E
60	7	Jk2007	Ferret Blandón Moreno	580766	1343408	218	10834	Siguiente casa	S77E
61	48	Jk2048	Frente "Pisos y Azulejos"	580599	1343467	177	11011		W
62	6	Jk2006	Final Dupla Norte	580336	1343461	263	11274	Paralela Carret Norte	Sur
63	49	Jk2049	Venta de Madera "Amistad"	580114	1343520	230	11503		S79W
64	5	Jk2005	Esq E Colegio Loyola	579965	1343432	173	11676	Callejón cerrado *	N84E
65	50	Jk2050	Loyola	579890	1343502	103	11779		S85W
66	4	Jk2004	Contg Bahía Colegio Loyola	579793	1343449	111	11890	*** *	N87E
67	51	Jk2051	calle frente ESSO, Loyola	579738	1343523	92	11982		N86W
68	52	Jk2052	Frente a Sede Petronic	579609	1343544	131	12112	sensores en acera	N85W
69	3	Jk2003	Fte Ant Cine Margot	579492	1343487	130	12243	Contg 2a Bahía La Paz *	Sur
70	2	Jk2002	Parque La Paz	579281	1343479	211	12454		N71E
71	1	Jk2001	Parada de buses	579151	1343491	131	12584	Detrás Palacio Nacional *	Sur
72	128	Jk2128	Cancelleria	578996	1343364	200	12785	en acera, fuegos artificiales y alta musica	N07E
73	127	Jk2127	Parque Luis Alfonso Velasquez Flores	578987	1343224	140	12925	en acera	N04E
74	126	Jk2126	Segunda curva Dupla Sur	578830	1343145	176	13101	en tierra en acera, cerca de semaforo	N77E
75	125	Jk2125	Curva Dupla Sur	578746	1343109	91	13192	en carretera	N61E
76	124	Jk2124	Colegio Monte de Sion	578668	1343099	79	13271	en tierra en acera	S84E
77	123	Jk2123	Dupla Sur	578580	1343117	90	13361	en tierra en acera	S86E
78	122	Jk2122	Bahia Dupla Sur	578416	1343107	164	13525	en carretera	S80E
79	121	Jk2121	Parqueo del Estadio	578205	1343137	213	13738	en tierra en acera	N81E
80	85	Jk2085	Estadio Nacional	577982	1343141	223	13961	en acera	N71E
81	60	Jk2060	Repuestos J. Zelaya	577811	1343035	201	14162	en acera, adoquines, vibraciones se sienten	S34W
82	84	Jk2084	Restaurante Rincon Español	577714	1342928	144	14307	en acera, adoquines	N57E
83	61	Jk2061	Ruta Maya	577613	1342845	131	14437	tierra en acera, adoquines	S38W
84	83	Jk2083	Luna Colchones	577410	1342656	277	14715	en acera	N57E
85	82	Jk2082	Frente Banco Caley Dagnall	577320	1342595	109	14823	tierra en acera	N60E
86	81	Jk2081	Frente BDF-Gonzalez Pasos	577193	1342492	164	14987	en acera	N60E
87	80	Jk2080	Plaza Brazil	577123	1342434	91	15078	en acera	N61E
88	79	Jk2079	La Fosforrera	576998	1342335	159	15237	en acera	N64E
89	78	Jk2078	Casa de Campaña PLC	576910	1342250	122	15360		N60E
90	77	Jk2077	Frente Hermoso y Vigil S.A	576821	1342192	106	15466	en tierra al lado, cauce al lado sur de car	N62E
91	76	Jk2076	Distribudor Mercedes	576715	1342100	140	15606	en acera, cauce al lado sur de carretera	N60E
92	75	Jk2075	Frente Shell Batahola	576524	1341959	237	15844	en acera, cauce al lado sur de carretera	N58E
93	74	Jk2074	Frente Talleres del Minist	576440	1341903	101	15945	en acera, cauce al lado sur de carretera	N57E
94	73	Jk2073	Frente "El Gigante"	576288	1341829	169	16114	en acera, cauce al lado sur de carretera	N85E
95	72	Jk2072	Barberia Bethel	576157	1341803	134	16247	en acera, cauce al lado sur de carretera	N84E
96	71	Jk2071	Aldea SOS	575687	1341718	478	16725	en acera, cauce al lado sur de carretera	N88E
97	70	Jk2070	Batahola sur	575557	1341702	131	16856	en acera, cauce al lado sur de carretera	N88E
98	69	Jk2069	Rotulos	575450	1341676	110	16966	en acera, cauce al lado sur de carretera	N76E
99	68	Jk2068	Frente Hospital Psiquiatri	575315	1341605	153	17119	en acera	N60E
100	67	Jk2067	Laguna Asososca con un hoy	575217	1341451	183	17301	en tierra al lado de la carretera	N34E

Appendix 2: Coordinates of measurement sites

SEQ_NO	SITE	COD	LOCATION	COORD_E	COORD_N	DISTANCE	CUM_DIST	NOTES	DIR__X
101	66	Jk2066	Laguna Asososca	575161	1341310	152	17453	en tierra al lado de la carretera	N32E
102	65	Jk2065	Laguna Asososca con un hoy	575137	1341220	93	17546	en tierra al lado de la carretera	N30E
103	64	Jk2064	Fte Bahía Buses Las Piedrecitas	575018	1340985	263	17809		N27E
104	63	Jk2063	Frente Enitel Las Piedrecitas	575033	1340900	86	17896	tierra en acera	N22E
105	62	Jk2062	Hospital Fernando Velez Paiz	574917	1340644	281	18177	en tierra al lado de la carretera	N28E
106	105	Jk2105	Cybercafé Las Piedrecitas	574878	1340521	129	18306	en tierra al lado de carretera	S02W
107	106	Jk2106	Rypsa Pinturas	574843	1340437	91	18397	en acera	S06W
108	107	Jk2107	Ceprodel	574815	1340371	72	18468	en acera	S02W
109	108	Jk2108	Sinapred	574743	1340250	141	18609	en acera	S03W
110	109	Jk2109	Librería Hispanic	574756	1340181	70	18679	en acera	S03W
111	110	Jk2110	ESSO del km siete sur	574697	1339993	197	18876	en acera, pendiente (camiones van lentos co	S06W
112	120	Jk2120	Almuerzo Casero	574661	1339853	145	19021	en carretera	N34E
113	119	Jk2119	Fte Iglesia San Francisco	574634	1339747	109	19130	en acera, cerca cauce	N32E
114	118	Jk2118	Fte Indicosa	574587	1339656	102	19233	en concreto al lado de carretera, cerca cauce	N30E
115	117	Jk2117	Restaurante Oriental Express	574569	1339533	124	19357	en adoquines al lado de carretera	N32E
116	116	Jk2116	Fte Sala de Belleza Stilo's	574528	1339435	106	19463	en concreto al lado de carretera	N24E
117	115	Jk2115	Las Acacias	574465	1339095	346	19809	en tierra al lado de carretera	N12E
118	114	Jk2114	Carne Asada Kilocho	574461	1339009	86	19895	en tierra al lado de carretera	N12E
119	113	Jk2113	Fte Veterinaria San Patricio	574443	1338855	155	20050	en tierra al lado de carretera	N12E
120	112	Jk2112	Fte Ferreteria 8 1/2	574454	1338709	146	20197	en concreto al lado de carretera	N02W
121	111	Jk2111	Jardines S.A.	574416	1338642	77	20274	en tierra al lado de carretera	N20E

Recording sites on Dupla Norte parallel to 121-126 on Dupla Sur.

SEQ NO	SITE	COD	LOCATION	COORD_E	COORD_N	DISTANCE	CUM_DIST	DIST_BRKPT	NOTES	DIR_X
123	53	Jk2053	Palacio de las Communicaci	578913	1343583	367	13292	0	sensores en la carretera	N85W
124	54	Jk2054	Enitel-Casa Teran	578772	1343594	453	13553	141	en tierra	N85E
125	55	Jk2055	San Antonio	578621	1343605	508	13779	293		N79W
126	56	Jk2056	Frente Instalaciones Salaz	578504	1343609	498	13858	410	en la carretera	W
127	57	Jk2057	Frente Hogar Conrad Hilton	578291	1343629	537	14062	624	en carretera	N87W
128	58	Jk2058	Frente Hogar Conrad Hilton	578195	1343626	489	14227	719	en carretera	W
129	59	Jk2059	ESSO	578024	1343645	172	14399	891	en carretera	W

Appendix 3: Site records

Site	Grading	Type	K2	K2_Start	K2_Stop	Uni-axial	Uni_Start	Uni_Stop	veh_start	veh_stop	Note
1	4	I	LB012	1445,0	1555,0						OBS! Sr: 200
	1	I	LB013	1232,0	1450,0						OBS! Sr: 200
	5	I	LB014	1285,0	1355,0						OBS! Sr: 200
	2	I	LB015	1505,0	1992,0						OBS! Sr: 200
	3	I	LB016	1610,0	2665,0						OBS! Sr: 200
	10	I	LB017	-	-						
	10	I	LB018	-	-						
	10	I	LB019	-	-						
	10	I	LB020	-	-						
	0	N	LB021								1 min with rubber band
2	10	I	OT001								truck
	1	I				2.1.txt	969	1300	200	2700	trailer truck, small truck
	2	I	OT002	1505,0	2050,0	2.2.txt	919	1400	0	1750	tractor
	3	I	OT003	1500,0	1700,0						dumper
	0	N	OT004								
	10	I	OT005	2940,0	2980,0	2.3.txt	390	1360	0	1500	truck
	10	I	OT006	3230,0	3275,0	2.4.txt	235	650	100	1900	trailer truck
	0	N	OT007								
3	10	I	LG008	-	-						
	10	I	LG009	-	-						
	10	I	LG010	-	-						
	10	I	LG011	-	-						
	10	I	LG012	-	-						
	10	I	LG013	-	-						
	10	I	LG014								
	2	I	LG015	765,0	1345,0						2 trailer trucks
	1	I	LG016	3315,0	3600,0						trailer truck
	3	I	LG017	1230,0	1355,0						trailer truck
	10	I	LG018	-	-						
	10	I	LG019	-	-						
	10	I	LG020	-	-						
	10	I	LG021	-	-						
	10	I	LG022	-	-						
	0	N	LG023								1 min with rubber band
4	1	I	LH001	4220,0	5729,0						trailer trucks
	3	I	LH002	1565,0	1652,0						
	2	I	LH003	380,0	610,0						truck
	0	N	LH004								1 min without rubber band
5	10	I	LI001	-	-						
	10	I	LI002	-	-						
	10	I	LI003	-	-						
	1	I	LI004	1760,0	2672,0						truck
	2	I	LI005	375,0	520,0						bus
	0	N	LI006								1 min without rubber band
6	2	I	LJ001	1625,0	1780,0						
	3	I	LJ002	3388,0	3510,0						
	1	I	LJ003	550,0	1025,0						
	0	N	LJ004								1 min with rubber band

Grading: 1 represents best quality event, 10 is not even considered.

Type: I – impact recording
N – noise recording

SMALL DICTIONARY		
English	**Spanish**	**Axes**
truck	camion	3
trailer truck	furgón, rastra	5
tractor	cabezal	3
farming tractor	tractor	2
dumper	volquete	3
pick-up	camioneta	2

Appendix 3: Site records

SEQ_NO	SITE	COD	LOCATION			COORD_E	COORD_N	DISTANCE	CUM_DIST	NOTES	DIR__X
7	4	I				7.1.txt	1840	3130	570	3000	bus
	10	I				7.2.txt	520	1080	380	2100	tractor
	10	I				7.3.txt	1900	2500	520	3300	bus, 2 cars
	5	I				7.4.txt	1620	2530	600	2500	bus
	0	N	LN001								noise, pick-up on opposite lane
		E	LN002								accidental trig!
	3	I	LN003	1717,0	1845,0						bus
	10	I	LN004		???	7.5.txt	1390	2390	150	2200	bus - accelerating
	10	I	LN005								truck
	10	I	LN006								bus - coward driver!
	1	I	LN007	1750,0	1960,0	7.6.txt	965	1600	200	2000	truck
	2	I	LN008	1774,0	2400,0	7.7.txt	1060	2000	470	2000	small truck
	0	N	LN009								noise, mc
	0	N	LN010								noise, pick-up on opposite lane
8	1	I	LO001	1842,0	2100,0	8.1.txt	1373	2000	550	2300	bus
		I	LO002								bus
	3	I	LO003	2040,0	2190,0	8.2.txt	1275	1950	470	2500	bus
	0	N	LO004								noise, pick-up moving in
	4	I	LO005	3774,0	4000,0	8.3.txt	8590	9460	7200	10000	bus - the coward breaks
	0	N	LO006								noise, bike and Lada
	2	I	LO007	5830,0	8925,0	8.4.txt	2170	2930	1450	3000	bus
	0	N	LO008								
9	1	I	LP001	2020,0	2760,0	9.1.txt	1302	1780	750	1800	bus, car
	10	I				9.2.txt	370	868	250	1500	bus, car
	0	N	LP002								
	3	I	LP002	6332,0	6537,0	9.3.txt	180	580	160	1400	trailer truck
	10	I	LP003	607,0	750,0						
	2	I	LP004	2330,0	2520,0	9.4.txt	1230	1830	700	2000	bus, car
	0	N	LP005								
10	3	I				10.1.txt	790	1470	450	1500	trailer truck
	2	I	LQ001	1825,0	2075,0	10.2.txt	670	1010	350	1050	bus
	0	N	LQ002								
	1	I	LQ003	1710,0	2350,0	10.3.txt	500	1510	180	1400	bus
	0	N	LQ004								
	10	I	LQ005	1940,0	2150,0	10.4.txt	450	820	430	1350	bus, car
	0	N	LQ006								
	3	I	LQ007	2475,0	2610,0	10.5.txt	1760	2430	60	790	bus, small truck
11	2	I	LR001	2095,0	2250,0	11.1.txt	1030	1680	590	1700	bus
	1	I	LR002	1765,0	2180,0	11.2.txt	800	1500	540	1550	small truck
	4	I	LR003	1775,0	1885,0						small truck
	0	N	LR004								
	3	I				11.3.txt	990	1360	500	1600	bus
	10	I	LR006	2010,0	2140,0	11.4.txt	1080	1530	660	1750	truck, car
	0	N	LR007								noise, van

Appendix 3: Site records

Site	Grading	Type	K2	K2_Start	K2_Stop	Uni-axial	Uni_Start	Uni_Stop	veh_start	veh_stop	Note
12	1	I	LS001	1880,0	2337,0	12.1.txt	740	1350	400	1500	truck
	0	N	LS002								
	2	I	LS003	2300,0	2430,0	12.2.txt	1800	2760	870	2700	bus
	4	I				12.3.txt	250	650	120	1600	2 buses
	3	I				12.4.txt	1150	1500	440	1700	bus, car
	0	N	LS004								
	0	N	LS005								
	10	I	LS006	480,0	630,0	12.5.txt	340	1790	0	1700	military truck, car
13	2	I	LX001	1755,0	2130,0	13.1.txt	330	1510			2 trailer trucks (first one)
	3	I	LX001	3285,0	3250,0	13.1.txt	3400	4350	2700	4400	second trailer truck
	0	N	LX002								
	1	I	LX003	2124,0	2260,0	13.2.txt	1200	1500	430	1700	trailer truck, cars
	0	N	LX004								
	0	N	LX005								
14	1	I	LY001	1560,0	1650,0	14.1.txt	170	400	0	1000	trailer truck
	2	I	LY002	1600,0	1650,0	14.2.txt	390	870	250	1000	truck
	0	N	LY003								
	3	I				14.3.txt	169	590	0	800	truck
15	1	I	LZ001	2060,0	2300,0	15.1.txt	1275	1800	1100	2200	bus, truck
	0	N	LZ002								
	2	I	LZ003	1695,0	1870,0	15.2.txt	340	1050	160	1000	bus
	0	N	LZ004								
16	0	N	MA001								
	1	I	MA002	18750,0	18870,0						
	3	I	MA002	28830,0	29630,0	16.1.txt	757	1350	170	1900	trailer truck 120 full seconds
	0	N	MA003								
	2	I	MA004	1750,0	1935,0	16.2.txt	420	900	80	1550	trailer truck
17	1	I	MB001	1650,0	2400,0	17.1.txt	480	1000	280	1040	bus
	2	I	MB002	1860,0	1955,0	17.2.txt	661	873	450	1100	truck, car
	3	I	MB003	1670,0	1845,0	17.3.txt	300	530	140	1700	IFA truck
	0	N	MB004								short noise recording
	4	I	MB005	820,0	985,0						
	0	N	MB005								
18	10	I				18.1.txt	1000	1480	320	2400	trailer truck
	1	I	MD001	1900,0	2620,0	18.2.txt	783	2140	400	2200	trailer truck
	10	I				18.3.txt	646	850	260	2300	trailer truck
	0	N	MD002								
	3	I	MD003	1800,0	2015,0						truck loaded with "piedra cantera"
	0	N	MD004								
	2	I	MD005	3810,0	3915,0	18.4.txt	804	1420	240	1800	trailer truck, half aside rubber band
	0	N	MD006								noise, mc passes in the beginning
19	1	I	ME001	1860,0	2050,0	19.1.txt	703	900	470	1300	truck
	10	I	ME002	1970,0	3000,0	19.2.txt	930	1550	360	2250	SIL truck (crosses obstacle with one wheel)
	0	N	ME003								

Appendix 3: Site records

Site	Grading	Type	K2	K2_Start	K2_Stop	Uni-axial	Uni_Start	Uni_Stop	veh_start	veh_stop	Note
20	10	I	MF001	1895,0	1970,0						trailer truck
	10	I	MF002	1455,0	1545,0						trailer truck
	0	N	MF003								
		E	MF004								
	10	I				20.1.txt	560	1300	0	1900	trailer truck
	1	I	MF005	2060,0	2760,0	20.2.txt	140	800	0	900	truck
	0	N	MF006								
21	1	I	MG001	1960,0	2420,0	21.1.txt	445	1000	200	1200	bus, tractor
	2	I	MG002	1280,0	1435,0	21.2.txt	1430	1840	440	2200	trailer truck
	0	N	MG003								
	3	I				21.3.txt	270	580	60	700	bus
		E	MG004								
	0	N	MG005								
22	1	I	MH001	1855,0	2700,0	22.1.txt	855	1460	360	2450	trailer truck
	0	N	MH002								
	10	I	MH003	1915,0	2080,0	22.2.txt	1350	1780	180	2300	truck, half trailer truck
	2	I	MH004	1860,0	2010,0	22.3.txt	980	1250	300	2000	trailer truck
	0	N	MH005								noise, jonas is dragging rubber band, Lady passing
23	1	I	MI001	1830,0	2050,0	23.1.txt	850	1300	450	2200	trailer truck, bus
	0	N	MI002								
	0	N	MI003								
	3	I				23.2.txt	466	680	350	1000	small truck
	4	I				23.3.txt	2670	3180	1200	3800	trailer truck
	2	I	MI004	1790,0	2130,0						truck
24	10	I	MJ001	1675,0	1740,0	24.1.txt	630	820	320	1270	bus
	0	N	MJ002								
	2	I	MJ003	1275,0	1460,0						trailer truck, breaks!!
	3	I	MJ004	1485,0	1570,0	24.2.txt	380	720	0	1000	trailer truck, 2 cars
	0	N	MJ005								
	1	I	MJ006	1780,0	2300,0	24.3.txt	1032	2138	600	1550	bus
	0	N	MJ007								
25	4	I	MK001	1785,0	1880,0	25.1.txt	650	1000	300	1500	truck
	0	N	MK002								
	0	N	MK003								
	3	I	MK004	1585,0	1650,0	25.2.txt	47	217	40	520	bus
	2	I	MK005	2137,0	2350,0	25.3.txt	920	1330	330	1850	trailer truck
	1	I	MK005	1265,0	1660,0						
26	0	N	ML001								
	2	I	ML002	1750,0	1945,0	26.1.txt	819	1020	560	1800	bus
	3	I	ML003	2745,0	2940,0						2 trailer trucks
	4	I	ML003	21350,0	21570,0	26.2.txt	2080	2510	800	3100	2 trailer trucks
	0	N	ML004								
	1	I	ML005	1784,0	2080,0	26.3.txt	367	970	150	850	bus
	10	I	ML006	1715,0	1915,0	26.4.txt	656	954	300	1800	KAMAZ truck

Appendix 3: Site records

Site	Grading	Type	K2	K2_Start	K2_Stop	Uni-axial	Uni_Start	Uni_Stop	veh_start	veh_stop	Note
27	1	I	MM001	1730,0	2047,0	27.1.txt	570	1200	370	1150	truck
	10	I				27.2.txt	800	1040	340	1500	bus
	0	N	MM002								
	10	I	MM003	2590,0	2680,0	27.3.txt	695	1077	310	1450	truck with boards
	0	N	MM004								
	10	I	MM005	2175,0	2358,0	27.4.txt	1845	2070	480	2600	trailer truck with scrap
	0	N	MM006								
28	2	I	MN001	2635,0	2830,0	28.1.txt	410	800	250	1200	truck
	10	I	MN002	2130,0	2380,0						trailer truck
	0	N	MN003								
	10	I	MN004	1875,0	2000,0	28.2.txt	506	900	400	1700	tractor
	10	I				28.3.txt	430	760	150	1400	truck
	0	N	MN005								
	0	N	MN006								
	1	I	MN007	2290,0	2600,0	28.4.txt	1072	1600	720	2400	trailer truck
29	0	N	MO001								
	1	I	MO002	1580,0	1850,0	29.1.txt	390	968	230	850	trucks
	10	I	MO003	1965,0	2190,0	29.2.txt	520	740	350	1400	trailer trucks
		E	MO004			29.3.txt	290	540	80	650	truck
	10	I				29.4.txt	670	900	260	1800	trailer truck (half crossing band)
	10	I	MO005	2295,0	2500,0	29.5.txt	1930	2470	1700	3200	trailer truck, bus
	0	N	MO006								
30	2	I	MP001	1465,0	1800,0						truck
	10	I	MP002								truck
	0	N	MP003								short noise recording
	3	I	MP004	1755,0	1950,0	30.1.txt	770	1710	150	2000	trailer truck
	0	N	MP005								
	1	I				30.2.txt	2419	3000	2000	3200	trailer truck
	10	N	MP006								
31	1	I	MQ001	1770,0	1980,0	31.1.txt	926	1400	580	2250	trailer truck, pick-up
	10	I				31.2.txt	1460	1840	140	2100	trailer truck
	10	I				31.3.txt	1120	1760	250	1950	trailer truck
		E	MQ002								
	10	I	MQ003								
	0	N	MQ004								short noise recording
	0	N	MQ005								short noise recording
	0	N	MQ006								noise
32	0	N	MR001								
	2	I	MR002	1700,0	1775,0	32.1.txt	536	733	330	1500	small truck with trailer
	1	I	MR003	1603,0	1900,0	32.2.txt	690	1340	470	1400	small truck with trailer
	0	N	MR004								
33	10	I	MS001								bus
	10	I	MS002								small truck
	0	N	MS003								
	1	I	MS004	1690,0	2500,0	33.1.txt	647	1200	400	1400	tractor
	10	I	MS005								farming tractor (really bad)
	2	I	MS006	1780,0	2100,0	33.2.txt	460	900	230	1300	GMC truck

Appendix 3: Site records

Site	Grading	Type	K2	K2_Start	K2_Stop	Uni-axial	Uni_Start	Uni_Stop	veh_start	veh_stop	Note
34	2	I				34.1.txt	1080	1600	280	1600	trailer truck
	0	N	MT001								noise (Coca Cola truck)
	10	I	MT002								tractor (screaming breaks)
	1	I	MT003	2710,0	3230,0	34.2.txt	260	1000	0	1000	2 simultaneous trucks
	10	I	MT004								trailer truck
	0	N	MT005								
	0	N	MT006								
	10	I	MT007	1755,0	1955,0	34.3.txt	870	1260	100	2000	trailer truck and truck simultaneously
	0	N	MT008								
35	10	I	MU001								tanker
	0	N	MU002								
	0	N	MU003								bad noise recording
	0	N	MU004								
	10	I	MU005	1430,0	1545,0	35.1.txt	150	940	0	1100	bus (bad one)
	10	I	MU006								trailer truck, minibus, trailer truck
	0	N	MU007								
	1	I	MU008	1490,0	1980,0	35.2.txt	400	1250	0	1500	bus
36	10	I				36.1.txt	840	1500	230	1550	
	1	I	MV001	1685,0	1980,0	36.2.txt	440	950	170	1200	
	10	I				36.3.txt	440	980	0	1000	
	10	I	MV002	-	-	36.4.txt	890	1430	400	2000	
	10	I	MV003			36.5.txt	460	790	240	1000	
	10	I	MV004								
	10	I	MV005								
	10	I				36.6.txt	413	1350	180	1300	
37	3	I				37.1.txt	446	750	0	1600	bus, truck, bus (first bus)
	10	I				37.1.txt	2800	3120	1800	3300	bus, truck, bus (truck)
	10	I	MW001								tractor
	1	I	MW002	1640,0	2020,0	37.2.txt	725	1200	360	1300	truck
	10	I	MW003								trailer truck
	10	I	MW004								truck
	10	I	MW005	2350,0	2535,0	37.3.txt	845	1140	390	2500	trailer truck
	0	N	MW006								
	2	I	MW007	1630,0	1710,0	37.4.txt	846	1200	100	1450	2 trailer trucks
	10	I				37.5.txt	627	980	130	1350	truck
	0	N	MW008								
38	2	I				38.1.txt	730	900	430	1500	truck
	1	I	MX001	1710,0	2000,0	38.2.txt	355	1000	100	1050	tractor
	10	I	MX002								bus, cab
	0	N	MX003								
	10	I	MX004								tanker
	0	N	MX005								
	10	I	MX006	2275,0	2440,0	38.3.txt	2005	2505	680	3000	trailer truck
	10	I	MX007								trailer truck

Appendix 3: Site records

Site	Grading	Type	K2	K2_Start	K2_Stop	Uni-axial	Uni_Start	Uni_Stop	veh_start	veh_stop	Note
39	0	N	MY001								
	10	I				39.1.txt	830	1140	400	1530	truck, mc
	10	I				39.2.txt	432	780	180	1050	truck
	2	I				39.3.txt	605	960	300	1200	bus
	10	I	MY002	1915,0	2060,0	39.4.txt	460	760	0	1050	trailer truck
	1	I	MY003	1625,0	1930,0	39.5.txt	630	1270	260	1500	KAMAZ truck, car
	0	N	MY004								
40	10	I				40.1.txt	800	1050	0	1600	bus,car,bus
	10	I	MZ001								truck (loud music)
	1	I	MZ002	119,0	350,0						truck
	10	I	MZ003								truck
	10	I	MZ004	2115,0	2150,0	40.2.txt	2720	3400	1460	3600	tanker
41	10	I	NA001	2155,0	2230,0	41.1.txt	1390	1690	350	2300	trailer truck loaded with scrap
	1	I	NA002	1655,0	2045,0	41.2.txt	406	1190	50	1200	Toyota truck
	10	I	NA003	2070,0	2250,0	41.3.txt	1285	1670	230	2300	trailer truck
	0	N	NA004								
	2	I	NA005	1805,0	1885,0	41.4.txt	400	680	170	1200	small IFA truck
	10	I				41.5.txt	975	1360	170	2070	unloaded trailer truck (honking)
42	0	N	NB001								
	2	I	NB002	26190,0	26260,0	42.1.txt	700	1040	260	2300	trailer truck, car
	1	I	NB003	1960,0	2600,0	42.2.txt	710	1370	200	1750	truck w. tiny trailer
	0	N	NB004								
43	1	I	NC001	1475,0	1700,0						bus (Lawson error)
	3	I	NC002	1860,0	2135,0						trailer truck (Lawson error)
	2	I	NC003	1610,0	1735,0						bus (Lawson error)
	10	I									tanker (Lawson error)
44	10	I				44.1.txt	813	1145	230	1300	bus
	2	I	ND001	1655,0	1720,0	44.2.txt	445	700	270	1200	small truck, car
	0	N	ND002								
	1	I	ND003	1800,0	2479,0	44.3.txt	531	1170	60	1600	tanker
45	10	I	NE001	-	-	45.1.txt	3092	3250	2000		truck, trailer truck, truck
	2	I	NE002	1620,0	1900,0	45.2.txt	210	700			MACK truck, Lawson Labs behaving curiously, samples at lower
	10	I	NE003	1635,0	1770,0	45.3.txt	555	700			tanker, Lawson Labs behaving curiously, samples at lower rate
	10	I	NE004								dumper
	0	N	NE005								
	1	I	NE006	1630,0	1750,0	45.4.txt	210	600	0	1200	bus
	10	I	NE007	1600,0	1650,0	45.5.txt	404	600	0	1300	garbage truck
46	0	N	NF001								
	0	N	NF002								
	10	I				46.1.txt	1070	1400	400	2000	truck, accelerating
	1	I				46.2.txt	570	1500	0	1500	trailer truck (rubber band flipped over)
	2	I	NF003	1795,0	2100,0	46.3.txt	600	1000	0	1600	bus
	10	I	NF004	1730,0	1800,0	46.4.txt	460	800	0	1500	trailer truck

Appendix 3: Site records

Site	Grading	Type	K2	K2_Start	K2_Stop	Uni-axial	Uni_Start	Uni_Stop	veh_start	veh_stop	Note
47	10	I				47.1.txt	1310	1600	430	2200	trailer truck, bus
	10	I				47.2.txt	370	600	180	1000	KAMAZ truck
	0	N	NG001								jonas kicking the rubber band
	10	I	NG002	360,0	415,0	47.3.txt	1338	1720	0	2100	farming tractor w. Trailer
	3	I	NG003	1600,0	1750,0	47.4.txt	235	400	0	1200	Mercedes truck
	0	N	NG004								
	4	I	NG005	1735,0	1890,0	47.5.txt	517	700	220	1700	trailer truck
	1	I	NG006	1705,0	1868,0	47.6.txt	510	824	330	1000	Volvo truck
	2	I	NG007	1420,0	1645,0	47.7.txt	0	400	0	750	KAMAZ truck (recorded too late with Lawson Labs)
	0	N	NG008								
48	3	I				48.1.txt	670	900	370	2000	trailer truck, fast
	1	I	NH001	1700,0	1870,0	48.2.txt	460	1100	0	1500	trailer truck, fast + car
	10	I	NH002								IVECO truck
	0	N	NH003								noise?
	2	I	NH004	1710,0	1830,0	48.3.txt	850	1100	520	2000	tanker
	0	N	NH005								
49	0	N	NI001								long and profound silence
	4	I				49.1.txt	900	1200	240	3000	trailer truck, slow
	3	I				49.2.txt	386	600	80	1800	truck, car
	2	I				49.3.txt	206	500	0	1100	bus, 2 mc:s
	0	N	NI002								
	1	I	NI003	1635,0	2060,0	49.4.txt	600	1160	0	1500	trailer truck
	10	I	NI004	1620,0	1680,0	49.5.txt	100	300	0	1250	garbage truck (half off)
	10	I	NI005	1640,0	1780,0	49.6.txt	490	800	250	1400	tractor
	10	I	NI006	1850,0	2000,0	49.7.txt	1290	1600	470	2300	trailer truck, small truck
50	0	N	NJ001								
	10	I				50.1.txt	970	1400	160	2300	trailer truck
	1	I	NJ002	1400,0	2060,0	50.2.txt	375	916	150	1200	crane
	2	I				50.3.txt	558	700	270	1100	Coca Cola truck
	0	N	NJ003								
	10	I	NJ004								tanker (half off)
	10	I	NJ005								trailer truck (half off)
	10	I	NJ006								truck, car
	10	I	NJ007								truck
51	0	N	NK001								noise(?)
	10	I				51.1.txt	640	900	330	1600	bus
	10	I				51.2.txt	654	900	0	1400	trailer truck, mc
	4	I	NK002	1720,0	1845,0	51.3.txt	460	770	180	1200	dumper, 2 cars
	2	I	NK003	1580,0	1690,0	51.4.txt	560	850	350	1150	truck, 2 cars
	10	I				51.5.txt	385	600	100	1100	fast bus, small truck
	10	I	NK004	1665,0	1730,0	51.6.txt	305	400	0	1200	KPA3 trailer truck
	10	I	NK005	1865,0	2000,0	51.7.txt	1060	1300	330	2000	trailer truck, van
	10	I				51.8.txt	376	480	120	1200	truck
	0	N	NK006								
	1	I	NK007	1535,0	1919,0	51.9.txt	438	980	230	1200	MACK truck
	3	I	NK008	1645,0	1770,0	51.10.txt	744	1000	200	1400	tanker, 3 cars
	10	I				51.11.txt	374	500	0	1500	bus

Appendix 3: Site records

Site	Grading	Type	K2	K2_Start	K2_Stop	Uni-axial	Uni_Start	Uni_Stop	veh_start	veh_stop	Note
52	0	N	NL001								
	1	I	NL002	1525,0	1700,0	52.1.txt	315	750	100	1000	dumper, car, mc
	3	I	NL003	1925,0	2005,0	52.2.txt	585	700	200	1050	trailer truck, car (band turned over by car)
	2	I	NL004	1645,0	1790,0	52.3.txt	515	700	300	1000	tanker, Mercedes truck, 3 cars
	4	I				52.4.txt	290	400	60	1100	tanker, cars
	10	I	NL005								tanker
	0	N	NL006								
	10	I	NL007								tanker
53	10	I	NM001	10760,0	10920,0	53.1.txt	1053	1500	150	1700	trailer truck, 2 cars, truck
	10	I	NM002	1770,0	1975,0	53.2.txt	1100	1800	0	2200	2 trailer trucks with scrap (good one)
	10	I				53.3.txt	230	800	0	1300	truck
	10	I	NM003	41980,0	42020,0	53.4.txt	4250	4500	3900		trailer truck, tractor (tractor)
	0	N	NM004								
	1	I	NM005	2400,0	2580,0	53.5.txt	1100	1350	160	2700	trailer truck, 3 cars
54	2	I	NN001	1720,0	1780,0	54.1.txt	658	900	300	2200	dumper
	0	N	NN002								long noise sample
	1	I	NN003	2055,0	2300,0	54.2.txt	1070	1450	80	1500	trailer truck, car
	3	I	NN004	10360,0	10470,0	54.3.txt	420	800	100	1450	bus
				11780,0	11880,0						
				18980,0	19080,0						
	0	N	NN005								
55	2	I	NO001	1785,0	1840,0	55.1.txt	988	1250	360	1900	trailer truck (half off), car
	0	N	NO002								
	10	I	NO003								dumper
	0	N	NO004								noise with mc
	0	N	NO005								
	10	I	NO006								farming tractor
	1	I	NO007	1700,0	1890,0	55.2.txt	829	1200	220	2600	trailer truck (good one)
56	0	N	NP001								
	1	I	NP002	1500,0	1650,0	56.1.txt	340	750	150	1200	MACK truck
	0	N	NP003								
	2	I	NP004	1740,0	1855,0	56.2.txt	1000	1600	300	2300	trailer truck, car
57	10	I	NQ001								trailer truck
	10	I	NQ002	1870,0	1995,0	57.1.txt	16663	1900	370	2500	tanker
	0	N	NQ003								noise with ambulance arriving
	1	I	NQ004	1635,0	1860,0	57.2.txt	445	1000	200	1000	truck, 2 cars
	2	I	NQ005	1775,0	1985,0	57.3.txt	770	1300	100	1400	trailer truck, mc, car, small truck
	0	N	NQ006								

Appendix 3: Site records

Site	Grading	Type	K2	K2_Start	K2_Stop	Uni-axial	Uni_Start	Uni_Stop	veh_start	veh_stop	Note
58	10	I	NR001								bus, car
	0	N	NR002								
	1	I	NR003	24470,0	25180,0	58.1.txt	382	1000	120	1000	truck
	2	I	NR004								trailer truck
	0	N	NR005								
59	1	I	NS001	1680,0	1900,0	59.1.txt	590	1000	120	1200	truck
	3	I				59.2.txt	0	300	0	800	truck
	0	N	NS002								
	10	I	NS003	1720,0	1865,0	59.3.txt	436	700	0	1200	truck
	0	N	NS004								
	2	I	NS005	1545,0	1700,0	59.4.txt	890	1200	460	2500	trailer truck
	0	N	NS006								very short noise recording
60	10	I				60.1.txt	768	1400	0	2000	trailer truck
	10	I	NT001	1530,0	1890,0	60.2.txt	471	1000	200	1900	dumper
	0	N	NT002								
	10	I				60.3.txt	410	900	100	1600	truck
	10	I				60.4.txt	1070	1400	200	2600	trailer truck, mc, car
	1	I	NT003	1540,0	1800,0	60.5.txt	426	800	160	1150	bus, car
	10	I	NT004	1700,0	1970,0	60.6.txt	1895	2300	0	1350	truck, dumper, 3 cars
	10	I	NT005	1480,0	1540,0	60.7.txt	700	900	360	1460	truck, car
	10	I				60.8.txt	500	1100	70	1700	tanker
	10	I	NT006	1545,0	1640,0	60.9.txt	230	600	0	1800	truck
	0	N	NT007								
61	0	N	NU001								
	0	N	NU002								
	2	I	NU003	1600,0	1780,0	61.1.txt	684	1000	270		tractor, van
	1	I	NU004	1700,0	2000,0	61.2.txt	915	1600	560	1800	bus
62	2	I	NV001	2025,0	2290,0	62.1.txt	1150	1500	500	2100	truck, jeep
	3	I	NV002	1770,0	1955,0	62.2.txt	866	1200	470	1540	truck
	1	I	NV003	1585,0	1850,0	62.3.txt	546	1000	240	1200	truck
	10	I	NV004	-	-	62.4.txt	2140	2500	1800	4100	trailer truck, pick-up
	0	N	NV005								
	10	I	NV006								truck
63	10	I	NW001								bus, mc, trailer truck
	10	I				63.1.txt	430	700	150	1000	bus
	2	I	NW002	1530,0	1730,0	63.2.txt	437	750	230	1000	bus
	0	N	NW003								good noise
	1	I	NW004	1660,0	1900,0	63.3.txt	360	840	70	800	bus
64	2	I	NX001	1735,0	2005,0	64.1.txt	400	700	140	1400	bus, jeep
	1	I	NX002	1620,0	1850,0	64.2.txt	358	886	120	1100	truck, car
	0	N	NX003								
	0	N	NX004								

Appendix 3: Site records

Site	Grading	Type	K2	K2_Start	K2_Stop	Uni-axial	Uni_Start	Uni_Stop	veh_start	veh_stop	Note
65	4	I				65.1.txt	190	400	0	700	very fast bus
	0	N	NY001								long noise sample
	10	I	NY002								slow dumper
	3	I				65.2.txt	425	600	200	1000	2 buses
	0	N	NY003								
	2	I	NY004	1795,0	2000,0	65.3.txt	480	750	300	1200	truck
	0	N	NY005								
	1	I	NY006	2010,0	2300,0	65.4.txt	696	1100	150	1300	trailer truck
66	0	N	NZ001								
	10	I	NZ002								truck
	2	I	NZ003	1630,0	1850,0	66.1.txt	506	800	150	1100	truck
	0	N	NZ004								
	0	N	NZ005								noise with car
	1	I	NZ006	1785,0	1995,0	66.2.txt	650	1000	130	1200	tanker
67	1	I	OA001	1420,0	1600,0	67.1.txt	530	1000	320	1200	truck
	0	N	OA002								
	2	I	OA003	1640,0	1780,0	67.2.txt	323	700	0	1100	truck, car
	5	I				67.3.txt	564	750	300	1400	bus
	6	I				67.4.txt	837	1000	560	1800	bus
	10	I	OA004								bus
	4	I				67.5.txt	400	600	230	1100	bus
	3	I	OA005	1590,0	1710,0	67.6.txt	343	550	160	1300	trailer truck, car
	0	N	OA006								
68	1	I	OB001	1440,0	1700,0	68.1.txt	210	750	0	800	truck, car
	0	N	OB002								short record of noise
	0	N	OB003								
	2	I	OB004	1605,0	1770,0	68.2.txt	330	700	0	1200	Mercedes truck
	10	I	OB005	11590,0	11760,0	68.3.txt	1877	2200	200	2500	trailer truck
	4	I	OB006	36380,0	36480,0	68.4.txt	260	600	0	1000	truck, 3 cars
	0	N	OB007								
	3	I				68.5.txt	365	650	100	1000	bus
	10	I	OB008								truck
69	0	N	OC001								
	3	I				69.1.txt	240	500	190	900	bus (second wheel pair)
	2	I	OC002	1780,0	1900,0	69.2.txt	380	550	60	1000	truck
	0	N	OC003								
	1	I	OC004	1650,0	1850,0	69.3.txt	489	800	290	1000	dumper
70	0	N	OD001								
	0	N	OD002								
	2	I	OD003	1835,0	2055,0	70.1.txt	890	1200	430	1800	bus
	1	I	OD004	1420	1600	70.2.txt	225	600	0	1100	bus
	3	I	OD004	3000,0	3150,0						
71	1	I	OE001	1405,0	1550,0	71.1.txt	165	550	0	800	tractor
	0	N	OE002								noise w. Music
	0	N	OE003								noise w. Music
	2	I	OE004	2710,0	2900,0	71.2.txt	2365	2600	2100	3200	2 trucks

Appendix 3: Site records

Site	Grading	Type	K2	K2_Start	K2_Stop	Uni-axial	Uni_Start	Uni_Stop	veh_start	veh_stop	Note
72	1	I				72.1.txt	400	800	160	1000	MACK truck
	0	N	OF001								
	2	I	OF002	1500,0	1695,0	72.2.txt	413	1200	340	1800	GMC truck
	3	I	OF003	1720,0	1850,0	72.3.txt	514	800	210	1000	Mercedes dumper
73	4	I				73.1.txt	580	950	360	1800	truck
	3	I	OG001	1415,0	1530,0	73.2.txt	0	200	0	1300	bus
	2	I	OG002	1515,0	1900,0	73.3.txt	420	1500	90	1600	bus
	0	N	OG003								noise (poor)
	1	I	OG004	1665,0	1950,0	73.4.txt	545	1147	200	1200	Mercedes truck, 2 cars
	0	N	OG005								
74	1	I	OH001	250,0	500,0	74.1.txt	0	600	0	800	bus (second wheel pair), truck, 2 veh
	2	I	OH002	1710,0	2045,0	74.2.txt	420	700	200	1100	Isuzu tanker
	3	I	OH003	1825,0	1940,0	74.3.txt	420	3625	0	1000	Dodge truck
	0	N	OH004								
	0	N	OH005								
75	0	N	OI001								
	1	I	OI002	1565,0	1750,0	75.1.txt	620	1000	200	1300	Coca Cola truck
	10	I	OI003								
	0	N	OI004								
76	0	N	OJ001								
	3	I				76.1.txt	1227	1400	270	1770	trailer truck
	2	I	OJ002	2530,0	2610,0	76.2.txt	830	1050	250	2600	slow trailer truck
	0	N	OJ003								
	1	I	OJ004	1800,0	2000,0	76.3.txt	460	800	150	1000	Mercedes truck
77	0	N	OK001								
	10	I	OK002								truck, 4 cars
	0	N	OK003								
	1	I	OK004	1520,0	1700,0	77.1.txt	266	600	0	650	Nissan truck
	2	I	OK005	1655,0	1900,0	77.2.txt	560	800	140	1000	bus
78	2	I				78.1.txt	180	300	0	1000	bus
	4	I	OL001	1660,0	1875,0	78.2.txt	360	600	100	1500	dumper, truck
	0	N	OL002								
	3	I	OL003	1660,0	1765,0	78.3.txt	260	500	0	900	truck, 3 cars
	1	I	OL004	1760,0	1900,0	78.4.txt	400	700	200	1300	trailer truck
	0	N	OL005								
79	1	I	OM001	1451,0	1700,0	79.1.txt	206	700	0	1000	bus
	10	I	OM002								KAMAZ trailer truck
	0	N	OM003								
	0	N	OM004								good noise
80	2	I				80.1.txt	270	600	0	1200	bus
	0	N	ON001								
	10	I	ON002								Mercedes truck (poor)
	0	N	ON003								short noise record
	0	N	ON004								
	0	N	ON005								
	10	I	ON006								truck, dumper (poor)
	1	I	ON007	1965,0	2200,0	80.2.txt	240	1000	0	1200	small truck

Appendix 3: Site records

Site	Grading	Type	K2	K2_Start	K2_Stop	Uni-axial	Uni_Start	Uni_Stop	veh_start	veh_stop	Note
81	0	N	OO001								
	1	I	OO002	1440,0	1700,0	81.1.txt	230	700	0	800	bus, 2 cars
	0	N	OO003								
	0	N	OO004								
	2	I	OO005	1696,0	1787,0	81.2.txt	80	300	0	800	dumper
82	2	I				82.1.txt	814	950	100	1700	trailer truck
	3	I				82.2.txt	350	480	0	1000	MACK truck
	0	N	OP001								
	1	I	OP002	1500,0	1660,0	82.3.txt	280	563	0	1500	trailer truck
	0	N	OP003								man passing close to K2
83	0	N	OQ001								short noise record
	10	I	OQ002								Mercedes truck (poor)
	0	N	OQ003								
	2	I	OQ004	1520,0	1750,0	83.1.txt	360	800	0	1000	bus
	0	N	OQ005								
	1	I	OQ006	1595,0	1800,0	83.2.txt	330	600	70	1000	Mercedes truck
84	1	I	OR001	1680,0	2000,0	84.1.txt	392	800	100	1400	bus
	0	N	OR002								
	0	N	OR003								
	10	I	OR004								Ford truck
	10	I	OR005	---	---	84.2.txt	100	300	0	2000	trailer truck
85	10	I	OS001	1840,0	1980,0	85.1.txt	842	1200	0	1770	trailer truck
	10	I	OS002								MACK truck
	0	N	OS003								
	10	I	OS004								GMC truck
	2	I	OS005	1410,0	1650,0	85.2.txt	335	890	0	1000	Mercedes truck
	3	I				85.3.txt	200	600	0	1000	Mercedes truck
	10	I				85.4.txt	522	940	230	1600	2 dumpers
	1	I	OS006	1705,0	2000,0	85.5.txt	670	1500	0	1600	trailer truck
	10	I	OS007	325,0	480,0	85.6.txt	969	1400	200	1900	trailer truck, small truck
86	10	I	OU001								2 trailer trucks
	0	N	OU002								
	1	I	OU003	2405,0	2700,0	86.1.txt	2160	2700	0	1000	dumper heavily loaded
	2	I	OU004	1605,0	1900,0						trailer truck
	4	I	OU005	1565,0	1850,0	86.2.txt	836	1100	190	1500	lonesome trailer truck (good one)
	3	I	OU006	1728,0	2075,0	86.3.txt	730	1330	110	1800	trailer truck, 2 cars
	10	I	OU007	1770,0	1930,0	86.4.txt	520	900	0	1800	lonesome trailer truck (good one)
	0	N	OU008								
87	1	I	OV001	1625,0	1760,0	87.1.txt	380	630	170	1750	trailer truck
	2	I	OV002	1625,0	1945,0	87.2.txt	367	600	0	1400	trailer truck
	0	N	OV003								
	0	N	OV004								

Appendix 3: Site records

Site	Grading	Type	K2	K2_Start	K2_Stop	Uni-axial	Uni_Start	Uni_Stop	veh_start	veh_stop	Note
88	2	I	OW001	1595,0	1705,0	88.1.txt	400	600	200	1000	Mercedes truck
	0	N	OW002								
	0	N	OW003								
	3	I	OW004	2380,0	2550,0	88.2.txt	415	600	160	1400	trailer truck, bus
	1	I	OW004	2380,0	2550,0	88.2.txt	2050	2300	1750	2500	bus
	0	N	OW005								
	4	I	OW006	1830,0	1950,0	88.3.txt	760	950	630	1500	tanker, truck (truck)
89	2	I	OX001	2960,0	3200,0						
	1					89.1.txt	245	600	0	900	Volvo truck, car
	4	I	OX002	1360,0	1430,0	89.2.txt	730	1000	370	1600	Concrete truck
	10	I	OX003								Mercedes truck
	10	I	OX004	2650,0	2690,0	89.3.txt	738	950	0		trailer truck, 3 cars
	0	N	OX005								
	3	I	OX006	1630,0	1750,0	89.4.txt	247	450	0	800	Mercedes truck, 2 cars
	10	I	OX007	810,0	850,0	89.5.txt	960	1222	280	2400	trailer truck
	0	N	OX008								
90	2	I	OY001	1415,0	1550,0	90.1.txt	70	300	0	1000	Mercedes truck
	10	I	OY002								
	1	I	OY003	1625,0	1800,0	90.2.txt	400	650	0	1000	2 HINOS trucks
	0	N	OY004								
	3	I	OY005	1670,0	1870,0	90.3.txt	480	700	130	1400	dumper
	0	N	OY006								
91	9	I	PB001	590,0	655,0	91.1.txt	460	700	230	1500	tanker
	7	I	PB002	18060,0	18190,0						
	8	I	PB002	48610,0	48710,0						
	10	I	PB002	76690,0	77070,0						
	6	I	PB002	89590,0	89950,0						
	3	I	PB002	97440,0	97640,0						
	2		PB002	102200,0	102500,0	91.2.txt	800	1150	200	1800	International truck
	10	I	PB003	720,0	880,0	91.3.txt	670	800	240	2800	slow tanker
	0	N	PB004								
	4	I	PB005	650,0	715,0	91.4.txt	781	1200	200	2000	tanker
	5	I	PB006								trailer truck
	1	I	PB007	735,0	1000,0	91.5.txt	830	1360	380	1400	trailer truck
	0	N	PB008								Roger putting the rubber band into place
	0	N	PB009								
92	5	I	PC001	680,0	740,0	92.1.txt	600	740	200	1500	Mercedes tanker
	0	N	PC002								
	4	I	PC003	520,0	565,0	92.2.txt	470	600	150	1300	MACK trailer truck
	3	I	PC004	675,0	785,0	92.3.txt	256	600	0	1400	small tanker
	2	I	PC005	695,0	860,0	92.4.txt	370	700	140	1100	International truck, 2 cars
	1	I	PC006	640,0	900,0	92.5.txt	562	900	0	1100	trailer truck, bus
	10	I				92.6.txt	930	1100	130	1400	trailer truck (honking)
	0	N	PC007								
	10	I				92.7.txt	510	650	100	1000	trailer truck (band turned over)
	0	N	PC008								

Appendix 3: Site records

Site	Grading	Type	K2	K2_Start	K2_Stop	Uni-axial	Uni_Start	Uni_Stop	veh_start	veh_stop	Note
93	10	I	PD001								MACK truck
	0	N	PD002								
	0	N	PD003								
	0	N	PD004								
	10	I	PD005								bus
	2	I	PD006	1640,0	1800,0	93.1.txt	2520	2800	0	3700	very slow trailer truck
	1	I	PD007	570,0	750,0	93.2.txt	411	800	0	1400	Ford truck
	10	I	PD008	2285,0	2480,0	93.3.txt	3680	4200	2500	5200	trailer truck
94	10	I	PE001								dumper, cars
	0	N	PE002								
	1	I	PE003	840,0	1000,0	94.1.txt	900	1200	300	1600	trailer truck
	0	N	PE004								
	10	I				94.2.txt	1707	2050	540	3200	slow trailer truck
	10	I	PE005								dumper
	0	N	PE006								
95	2	I				95.1.txt	1220	1500	550	1700	trailer truck
	0	N	PF001								
	1	I	PF002	640,0	900,0	95.2.txt	707	1100	430	1400	tractor
	0	N	PF003								
96	2	I	PG001	825,0	1100,0	96.1.txt	1120	1600	250	2200	2 trailer trucks
	0	N	PG002								
	1	I	PG003	950,0	1200,0	96.2.txt	1000	1400	170	1400	trailer truck
97	0	N	PH001								
	2	I	PH002	825,0	1045,0	97.1.txt	1050	1470	370	1900	tanker
	1	I	PH003	703,0	1200,0	97.2.txt	720	1600	250	1700	trailer truck, small truck
	0	N	PH004								
98	10	I	PI001								bus
	2	I				98.1.txt	1100	1500	480	1700	tanker trailer truck
	1	I	PI002	560,0	700,0	98.2.txt	350	600	120	900	bus
	0	N	PI003								
	10	I	PI004	800,0	940,0	98.3.txt	470	650	720	1750	trailer truck, car, mc
	0	N	PI005								
99	1	I				99.1.txt	705	1500	360	1500	truck, car
	10	I	PJ001	1030,0	1175,0	99.2.txt	1160	1500	0	2200	very slow trailer truck
	5	I	PJ002	2085,0	2155,0	99.3.txt	875	1300	400	1400	very slow truck
	4	I	PJ003	540,0	585,0	99.4.txt	492	700	190	960	dumper, car
	3	I	PJ004	580,0	645,0	99.5.txt	577	900	0	1200	Mercedes truck, military truck
	6	I	PJ005	560,0	625,0	99.6.txt	430	560	350	1150	mc, Mercedes truck, 2 cars
	0	N	PJ006								
	2	I	PJ007	737,0	938,0	99.7.txt	494	900	160	1600	trailer truck, tanker, car
	8	I				99.8.txt	1345	1600	790	2780	trailer truck
	7	I				99.9.txt	1150	1350	380	1660	trailer truck, car
	0	N	PJ008								short noise record

Appendix 3: Site records

Site	Grading	Type	K2	K2_Start	K2_Stop	Uni-axial	Uni_Start	Uni_Stop	veh_start	veh_stop	Note
100	10	I	PK001								tanker
	1	I	PK002	596,0	800,0	100.1.txt	853	1100	600	1300	garbage truck, cars (poor one)
	10	I				100.2.txt	823	1100	140	1300	tanker, cars
	3	I	PK003	630,0	770,0	100.3.txt	380	600	240	1500	2 trailer trucks
	0	N	PK004								
	2	I	PK005	715,0	820,0	100.4.txt	711	1000	380	1900	trailer truck
	10	I				100.5.txt	1038	1300	160	1450	tanker, bus, cars
	10	I				100.6.txt	1800	2300	400	2600	slow trailer truck (interesting because of bouncing posterior axis)
	0	N	PK006								
101	0	N	PL001								
	1	I	PL002	699,0	900,0	101.1.txt	638	1100	130	1300	truck
	10	I	PL003								dumper
	2	I	PL004	874,0	1100,0	101.2.txt	1035	1500	200	1690	tanker trailer truck
	3	I	PL005	1575,0	1810,0	101.3.txt	3757	4200	2540	4700	2 trailer trucks (second one)
	0	N	PL006								
102	2	I	PM001	1612,0	1750,0	102.1.txt	2020	2200	0	1430	trailer truck, small truck
	0	N	PM002								
	0	N	PM003								
	3	I				102.2.txt	0	243	0	1030	trailer truck
	1	I	PM004	957,0	1100,0	102.3.txt	1270	1500	400	1570	trailer truck
103	10	I	PN001								tanker trailer truck
	3	I				103.1.txt	1210	1800	370	1850	trailer truck
		E	PN002								bad recording
	10	I	PN003								trailer truck (Lawson datafil saknas)
	2	I	PN004	640,0	760,0	103.3.txt	700	1000	230	1820	trailer truck, 3 cars
	1	I	PN005	806,0	1000,0	103.4.txt	524	900	140	940	tanker, 3 cars (good one)
	0	N	PN006								
104	5	I	PO001	720,0	1010,0	104.1.txt	404	800	0	1400	trailer truck, cars
	3	I	PO002	880,0	1135,0	104.2.txt	1190	1500	300	1900	trailer truck, cars
	10	I				104.3.txt	1775	2000	0	1060	truck, tractor, trailer truck
	10	I	PO003								trailer truck
	4	I	PO004	1470,0	1570,0	104.4.txt	850	1150	1400	2800	2 trailer trucks, many cars
	2	I				104.5.txt	3204	3500	300	1730	trailer truck, cars, bus (bus)
	10	I	PO005								MACK truck
	1	I	PO006	630,0	800,0	104.6.txt	1270	1600	660	1710	trailer truck, IFA truck
	0	N	PO007								
105	10	I	PP001								bus
	3	I	PP002	4420 35500,0 43340,0	4560 35820,0 43530,0	105.1.txt	700	900	180	2880	slow trailer truck
	0	N	PP003								
	1	I	PP004	610,0	850,0	105.2.txt	375	1000	0	1200	Nissan truck
	2	I	PP005	532,0	1000,0	105.3.txt	360	1000	0	1230	dumper
	0	N	PP006								

Appendix 3: Site records

Site	Grading	Type	K2	K2_Start	K2_Stop	Uni-axial	Uni_Start	Uni_Stop	veh_start	veh_stop	Note
106	10	I	PQ001								trailer truck
	10	I	PQ002								Mercedes truck
	10	I	PQ003								MAZ truck
	0	N	PQ004								
	2	I				106.1.txt	160	400	110	1100	bus
	1	I	PQ005	665,0	800,0	106.2.txt	304	500	0	800	2 buses (first)
	3	I	PQ005	1685,0	1735,0	106.2.txt	2320	2600	2050	3320	second bus
	4	I	PQ006	625,0	750,0	106.3.txt	180	500	120	650	Mercedes truck
	10	I	PQ007								dumper (poor one)
	10	I	PQ008	-	-	106.4.txt	2100	2300	0	2770	trailer truck
	5	I	PQ009	740,0	845,0	106.5.txt	540	750	280	1050	bus, car
	0	N	PQ010								
	10	I	PQ011	665,0	800,0	106.6.txt	260	800	0	2180	SIL truck
	0	N	PQ011								noise after SIL
107	1	I				107.1.txt	985	1300	300	1630	trailer truck (very good)
	10	I	PR001								trailer truck
	3	I	PR002	1005,0	1300,0	107.2.txt	1030	1400	0	1720	2 trailers truck, car in between (first trailer truck)
	10	I	PR002			107.2.txt	4750	5120	3330	6120	second trailer truck
	0	N	PR003								
		E	PR004								
	2	I	PR005	580,0	810,0	107.3.txt	660	1000	120	1570	trailer truck, car
	0	N	PR006								
108	0	N	PS001								
	0	N	PS002								
	10	I	PS003								trailer truck
	10	I	PS004								crane truck
	0	N	PS004								noise before crane truck
	10	I	PS005								dumper
	1	I	PS006	915,0	1100,0	108.1.txt	965	1300	300	2030	2 buses
	2	I	PS007	2800,0	2912,0	108.2.txt	5090	5600	4360	6060	trailer truck, bus, trailer truck (last trailer truck)
109	10	I	PT001								truck, mc
	3	I				109.1.txt	560	900	150	2430	trailer truck
	1	I	PT002	715,0	1230,0	109.2.txt	860	1500	0	1530	MACK trailer truck
	2	I	PT003	900,0	1075,0	109.3.txt	660	1000	170	1670	trailer truck, car (good one)
	10	I	PT004								trailer truck
	0	N	PT005								
	10	I	PT006	730,0	1290,0	109.4.txt	1120	2000	240	2500	trailer truck, car
	10	I				109.5.txt	1080	1500	210	1900	tanker trailer truck
	0	N	PT007								
	10	I	PT008								concrete truck
110	1	I				110.1.txt	547	1000	0	1230	bus, 2 trailer trucks (bus)
	10	I				110.1.txt	10390	10800	8900		last trailer truck
	2	I	PU001	775,0	1100,0	110.2.txt	154	300	20	300	2 dumpers (roaring engines)
	0	N	PU002								
	10	I	PU003								dumper
	0	N	PU004								
	10	I	PU005								KAMAZ dumper (poor one)

Appendix 3: Site records

Site	Grading	Type	K2	K2_Start	K2_Stop	Uni-axial	Uni_Start	Uni_Stop	veh_start	veh_stop	Note
111	0	N	PW001								
	10	I	PW002								truck, various vehicles (not very good)
	0	N	PW003								
	0	N	PW004								
	10	I	PW005								Nissan truck w. Sand
	1	I	PW006	677,0	850,0	111.1.txt	558	900	200	1470	dumper
	2	I				111.2.txt	326	659	0	1000	bus
	10	I	PW007								cargador (poor one)
	10	I	PW008								Mercedes truck (poor one)
	10	I	PW009	620,0	765,0	111.3.txt	185	400	0	1060	bus
112	2	I	PX001	1080,0	1300,0	112.1.txt	1230	1600	0	2300	accelerating trailer truck, MACK truck
	10	I	PX002								truck, small truck (not good)
	1	I				112.2.txt	179	500	0	1300	truck
	0	N	PX003								
	10	I	PX004	444,0	635,0	112.3.txt	333	700	0	990	bus, car
	10	I				112.4.txt	363	740	0	1880	MACK truck
	10	I	PX005	515,0	750,0	112.5.txt	430	800	0	2030	International truck, car
	0	N	PX006								
113	0	N	PY001								
	1	I	PY002	705,0	900,0	113.1.txt	310	1000	90	1670	solitary bus
	2	I	PY003	635,0	900,0	113.2.txt	640	1200	170	2230	dumper, truck
	0	N	PY004								
	0	N	PY005								
114	10	I				114.1.txt	405	650	200	1100	truck
	2	I	PZ001	890,0	1010,0	114.2.txt	925	1200	0	2160	2 trailer trucks (first)
	1	I	PZ001	3618,0	3900,0	114.2.txt	6377	6800	5400	7820	second trailer truck
	10	I	PZ002			114.3.txt	1300	1600	90	3980	trailer truck, tanker
	0	N	PZ002								noise afterwards
	0	N	PZ003								
	10	I	PZ004	655,0	940,0	114.4.txt	1040	1500	460	2390	trailer truck
	3	I	PZ004	5300,0	5460,0	114.5.txt	950	1100	220	1310	trailer truck
	0	N	PZ004								noise in between trailer trucks
115	1	I				115.1.txt	360	700	90	1150	solitary bus
	10	I	QA001								Mercedes truck (poor one)
	10	I	QA002	525,0	840,0	115.2.txt	304	910	0	2040	2 MACK trucks (first)
	0	N	QA003								
	0	N	QA004								
	0	N	QA005								
	10	I	QA006								bus (by the side)
	2	I	QA007	620,0	855,0	115.3.txt	334	700	160	1040	Toyota truck, car
116	1	I	QB001	595,0	800,0	116.1.txt	100	500	0	1070	bus, 2 small trucks
	10	I	QB002	420,0	610,0	116.2.txt	265	420	160	2160	Mercedes truck
	0	N	QB003								
	10	I	QB004	3875,0	4090,0	116.3.txt	350	650	0	2000	dumper, 2 cars, van
	0	N	QB005								

Appendix 3: Site records

Site	Grading	Type	K2	K2_Start	K2_Stop	Uni-axial	Uni_Start	Uni_Stop	veh_start	veh_stop	Note
117	10	I	QC001								bus
	10	I	QC002	1205,0	1275,0	117.1.txt	640	940	250	1420	Mercedes truck, car
	3	I	QC003	565,0	795,0	117.2.txt	3310	3800	3000		KAMAZ truck, 2 cars, bus (bus)
	0	N	QC004								
	1	I	QC005	2050,0	2290,0	117.3.txt	2870	3330	270	2380	trailer truck, bus, car
118	2	I				118.1.txt	2160	2500	1020	3300	trailer truck (roaring engine)
	1	I	QD001	330,0	750,0	118.2.txt	70	630	0	930	Mercedes truck
	10	I	QD002								Mercedes truck (poor one)
	0	N	QD003								
	0	N	QD004								short noise register
	2	I	QD005	545,0	900,0	118.3.txt	140	610	0	870	truck
		E				118.4.txt	480	820	360	1870	only second half of a trailer truck
119	10	I	QE001	685,0	840,0	119.1.txt	777	1100	200	1650	trailer truck, 2 cars
	1	I	QE002	700,0	830,0	119.2.txt	370	600	110	970	bus
	0	N	QE003								
	2	I	QE004	625,0	1040,0	119.3.txt	235	720	0	1100	bus and car simultaneously
	0	N	QE005								
120	10	I				120.1.txt	800	1200	0	1760	trailer truck, truck
	10	I	QF001	655,0	870,0	120.2.txt	530	760	100	1950	trailer truck
	0	N	QF002								
	0	N	QF003								
	1	I	QF004	640,0	850,0	120.3.txt	300	700	0	1030	bus, Nissan truck
	2	I	QF005	540,0	700,0	120.4.txt	285	600	0	1440	bus (not that good)
121	3	I	QG001	490,0	580,0	121.1.txt	383	600	90	1020	Pepsi truck, small truck (pretty bad)
	2	I	QG002	782,0	1060,0	121.2.txt	805	1400	430	1400	KAMAZ truck, van
	10	I	QG003	2900,0	3105,0	121.3.txt	1490	1720	0	2150	slow trailer truck, car, dumper, car
	1	I				121.4.txt	500	950	90	930	bus, car
	0	N	QG004								
	0	N	QG005								
122		E	QH001								
	1	I	QH002	510,0	650,0	122.1.txt	424	700	110	1360	bus, car
	0	N	QH003								
	0	N	QH004								
	2	I	QH005	605,0	800,0	122.2.txt	50	500	0	1030	truck
123	2	I	QI001	905,0	1050,0	123.1.txt	590	770	130	1650	bus, car
	0	N	QI001								
	0	N	QI002								
	0	N	QI003								
	10	I	QI004								dumper, truck
	1	I	QI005	745,0	1310,0	123.2.txt	495	1100	260	1570	solitary bus

Appendix 3: Site records

Site	Grading	Type	K2	K2_Start	K2_Stop	Uni-axial	Uni_Start	Uni_Stop	veh_start	veh_stop	Note
124		E	QL001								
	3	I	QL002	1005,0	1155,0	124.1.txt	980	1400	0	2700	truck, car
	0	N	QL002								
	2	I	QL003	625,0	800,0	124.2.txt	315	700	0	1200	dumper, truck
	5	I	QL004	565,0	645,0	124.3.txt	350	600	0	1200	bus, car
	1	I	QL005	768,0	930,0	124.4.txt	635	1000	300	1660	trailer truck
	0	N	QL006								
	0	N	QL007								
	6	I	QL008	700,0	790,0	124.5.txt	772	1000	370	1190	Coca Cola truck
	4	I	QL009	580,0	675,0	124.6.txt	550	710	260	1730	Truck, 2 cars
125		E	QM001								missed rubber band
	3	I	QM002	610,0	665,0	125.1.txt	320	550	80	930	truck
	0	N	QM003								
	1	I	QM004	575,0	730,0	125.2.txt	348	625	100	1130	truck, cars
	2	I	QM005	615,0	800,0	125.3.txt	310	630	0	1020	bus, car
	0	N	QM006								
	4	I	QM007	765,0	955,0	125.4.txt	960	1300	320	1980	trailer truck
126	4	I	QN001	1240,0	1340,0	126.1.txt	1660	1820	0	1220	military truck, smaller vehicle (2nd vehicle)
	3	I	QN002	1795,0	1885,0	126.2.txt	2763	2900	130	940	truck, cars, truck (2nd truck)
	0	N	QN003								
	2	I	QN004	755,0	890,0	126.3.txt	620	1160	350	1360	bus
	10	I	QN005	1400,0	1470,0	126.4.txt	1910	2020	170	2520	slow trailer truck
	0	N	QN006								good noise record
	1	I	QN007	735,0	840,0	126.5.txt	536	800	300	1060	truck, car
	10	I	QN008								slow trailer truck (poor one)
		E	QN009								
	10	I	QN010	2225,0	2355,0	126.6.txt	728	1000	320	1720	bus
127	0	N	QO001								
	4	I	QO002	1155,0	1335,0	127.1.txt	120	300	1290	2470	dumper,cars
	0	N	QO003								
	0	N	QO004								
	3	I	QO005	930,0	1015,0	127.2.txt	1037	1178	900	1800	bus
	1	I	QO006	-	-	127.3.txt	800	1150	420	1230	bus, cars
	10	I	QO007	800,0	925,0	127.4.txt	1300	1400	140	2380	truck
	0	N	QO008								very long noise record
	2	I	QO009	885,0	980,0	127.5.txt	1110	1600	580	1650	2 garbage trucks simultaneously
128	2	I	QP001	595,0	695,0	128.1.txt	490	690	470	1800	trailer truck (fireworks going on)
	0	N	QP002								loud music
	3	I	QP003	10930,0	11030,0	128.2.txt	1170	1400	460	2300	trailer truck (half off)
				24120,0	24160,0						
	0	N	QP004								largely without music
	4	I	QP005	1030,0	1145,0	128.3.txt	1280	1550	430	3350	tanker trailer truck, cars
	1	I	QP006	765,0	900,0	128.4.txt	460	700	230	1270	bus (at full speed)
	5	I	QP007	700,0	840,0	128.5.txt	800	1000	0	1820	trailer truck
	0	N	QP008								

Appendix 4: Local risk index

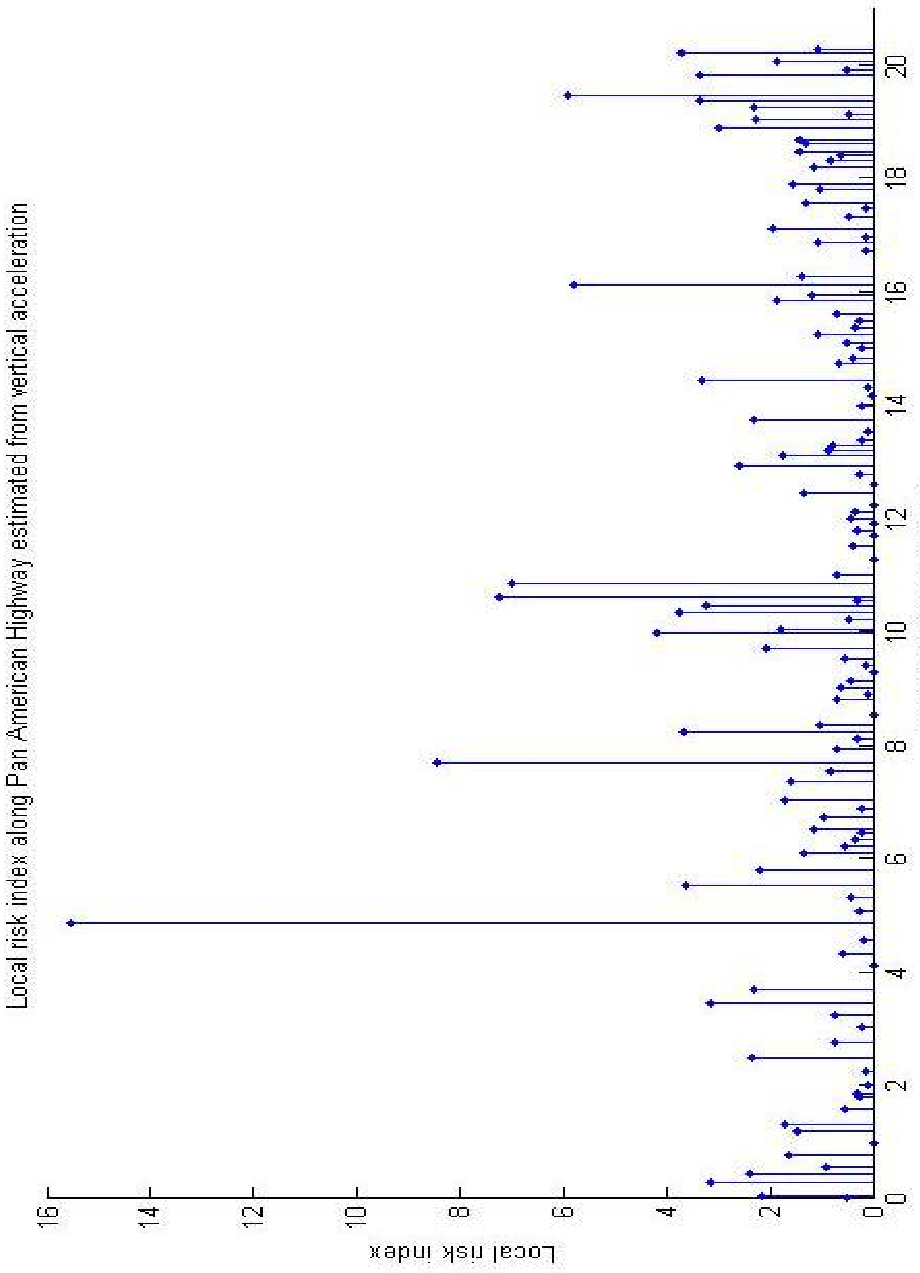

Appendix 4: Local risk index

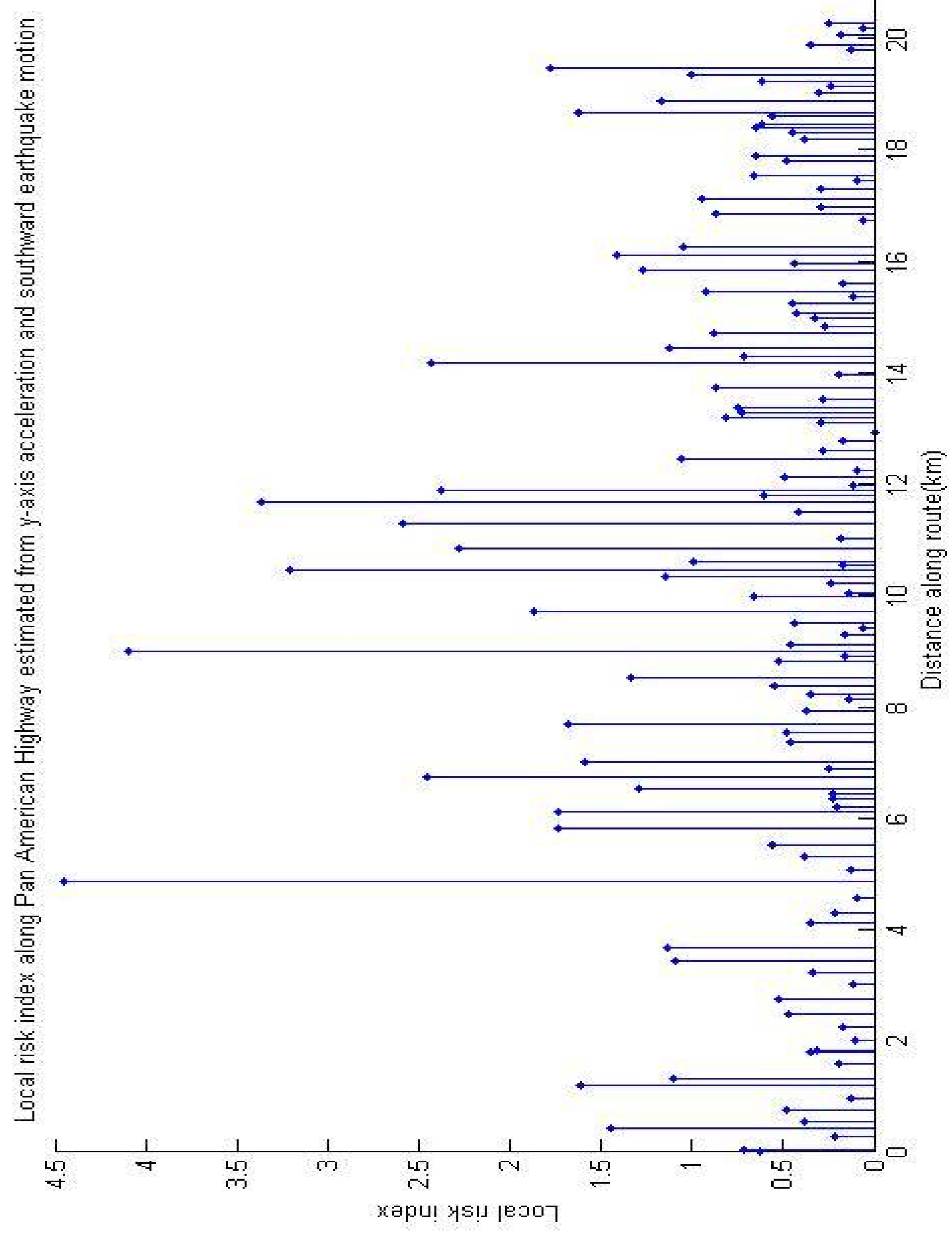

Appendix 4.3: Local risk index

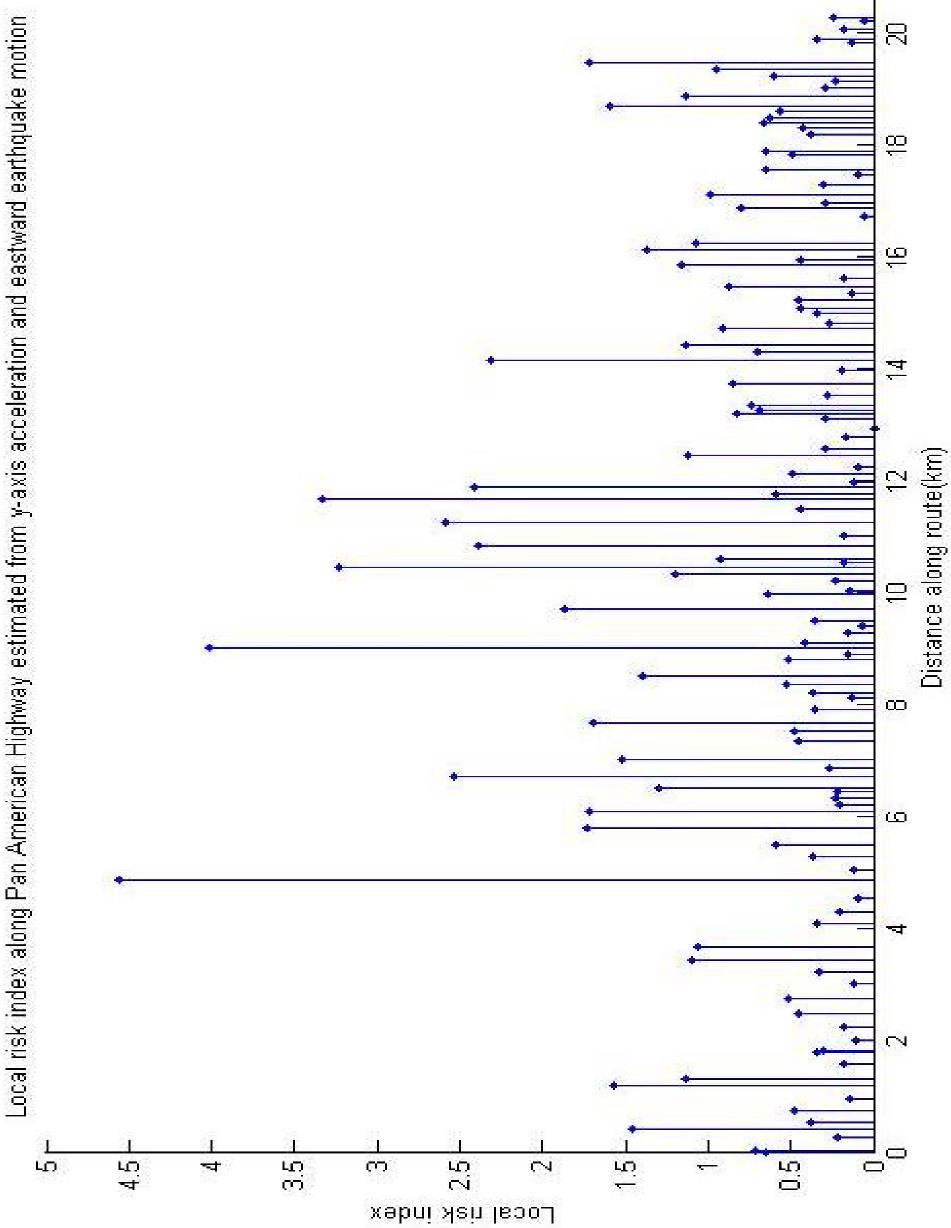

Appendix 4: Local risk index

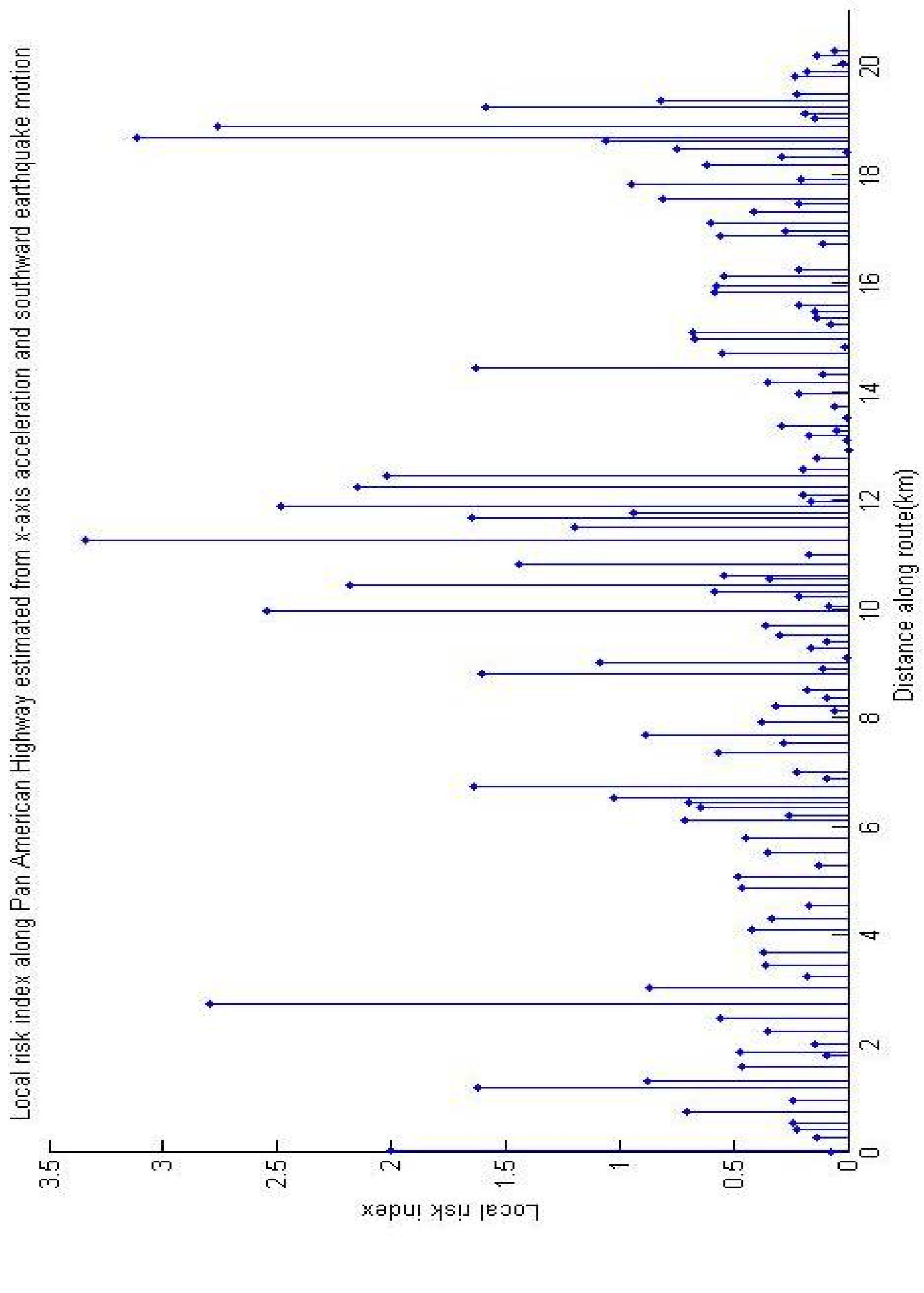

Appendix 4: Local risk index

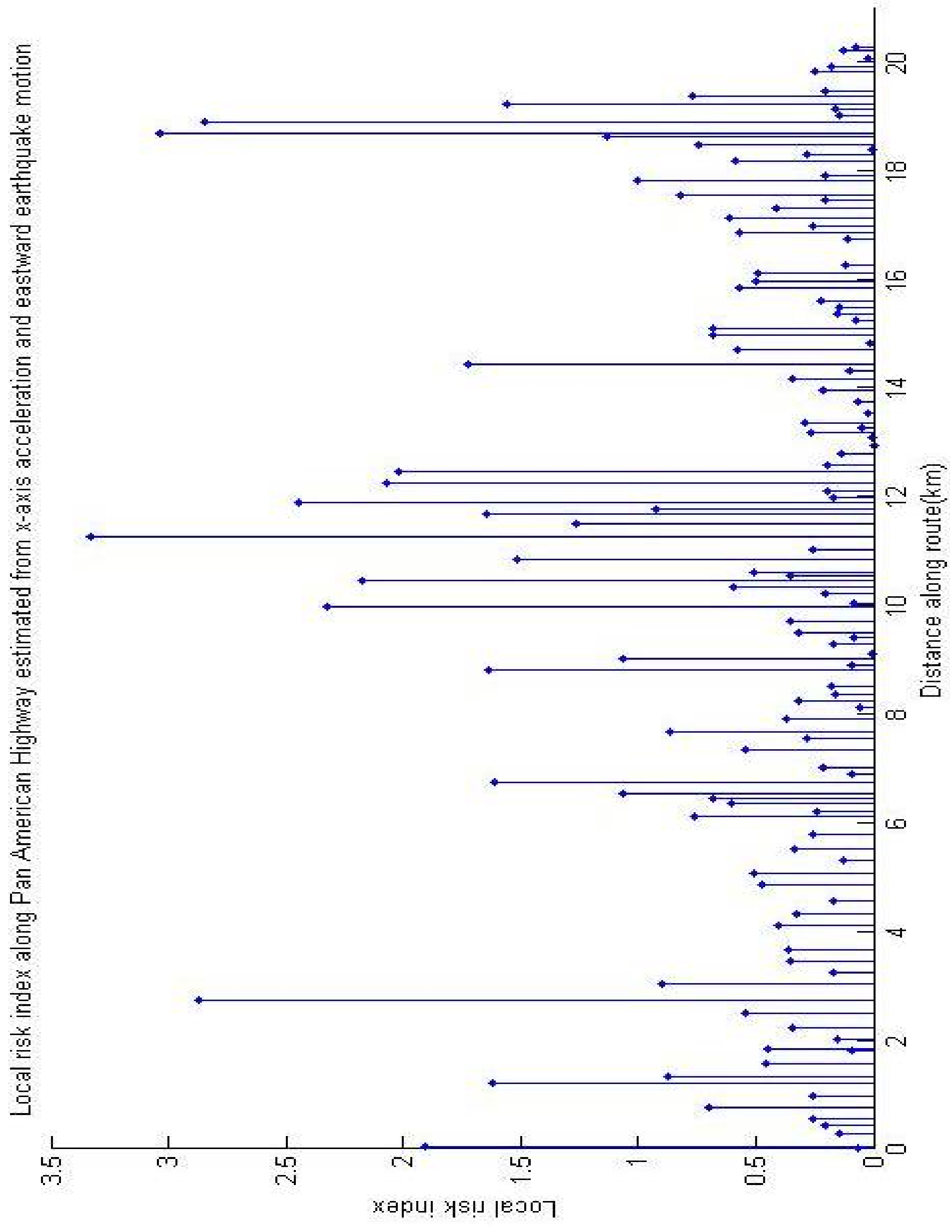

Appendix 4: Local risk index

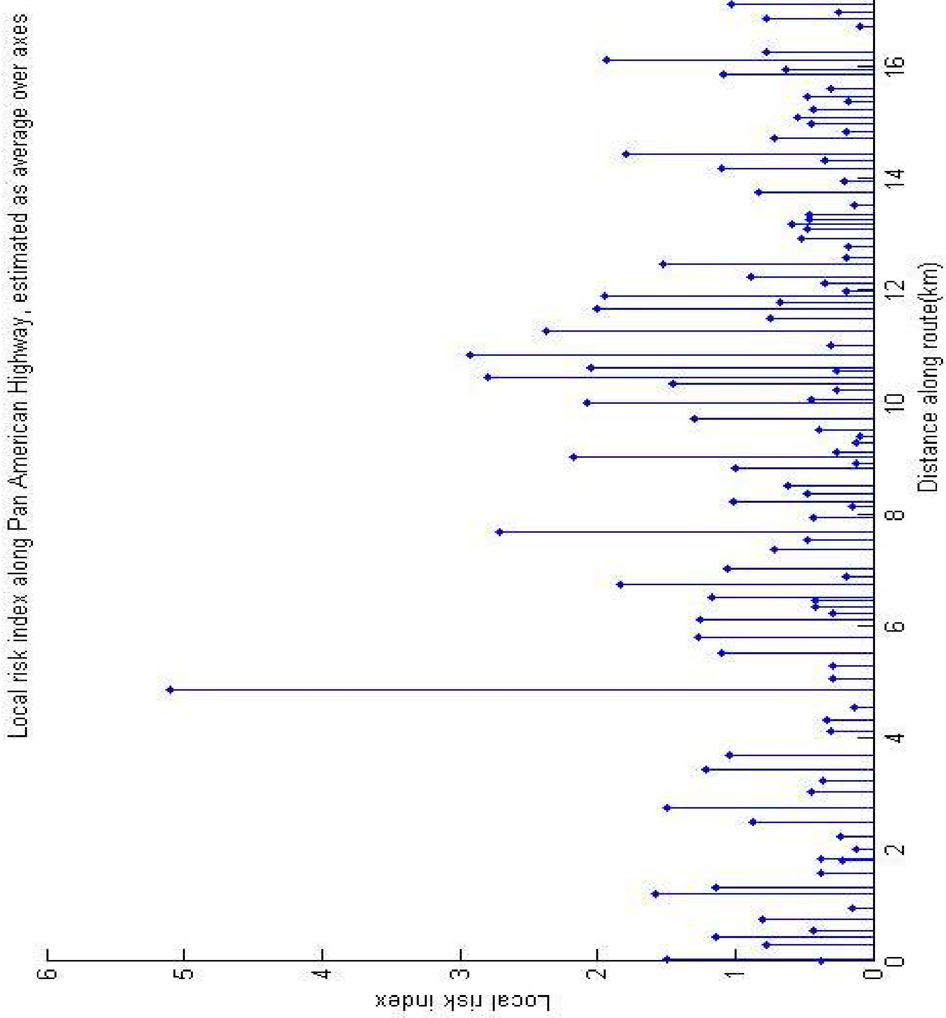

Appendix 5.1: Local risk maps

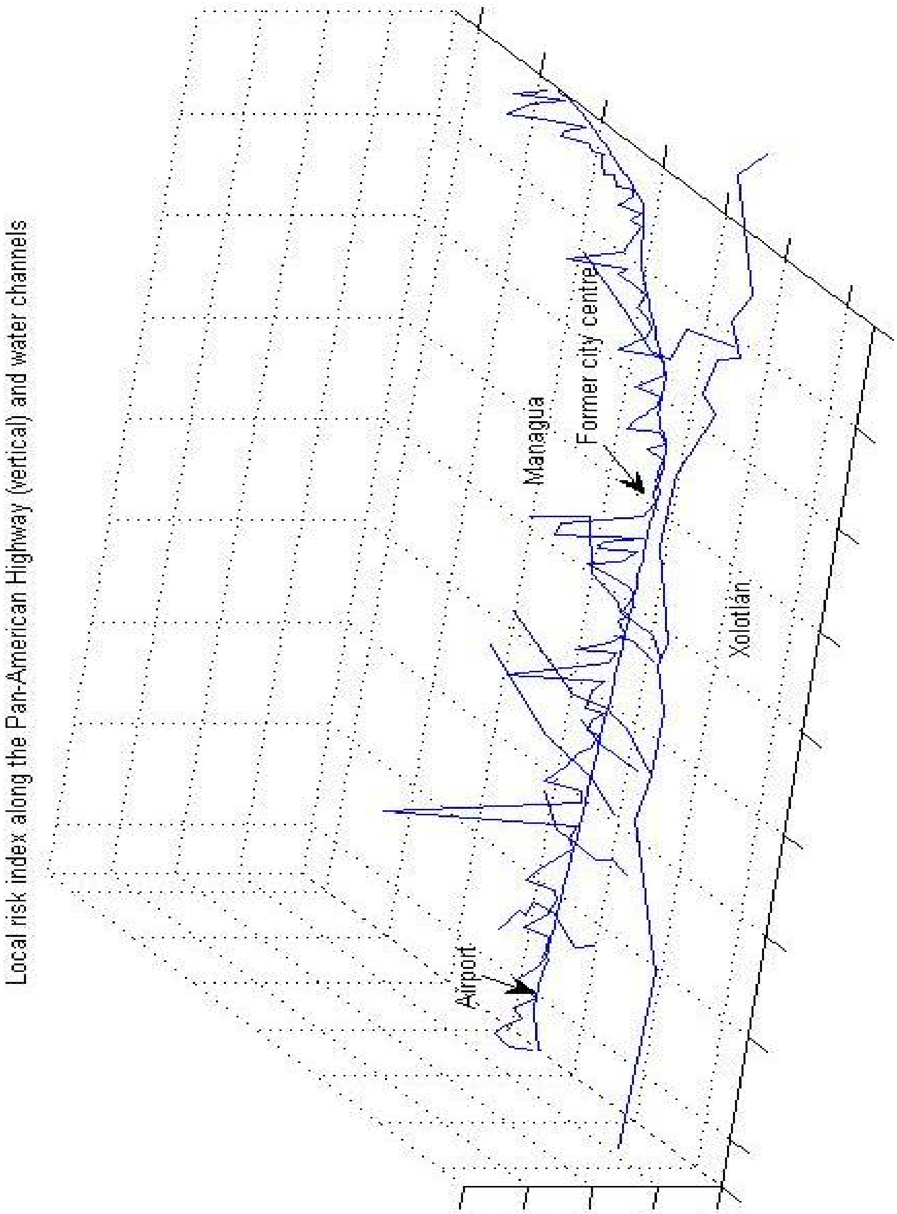

Appendix 5.2: Local risk maps

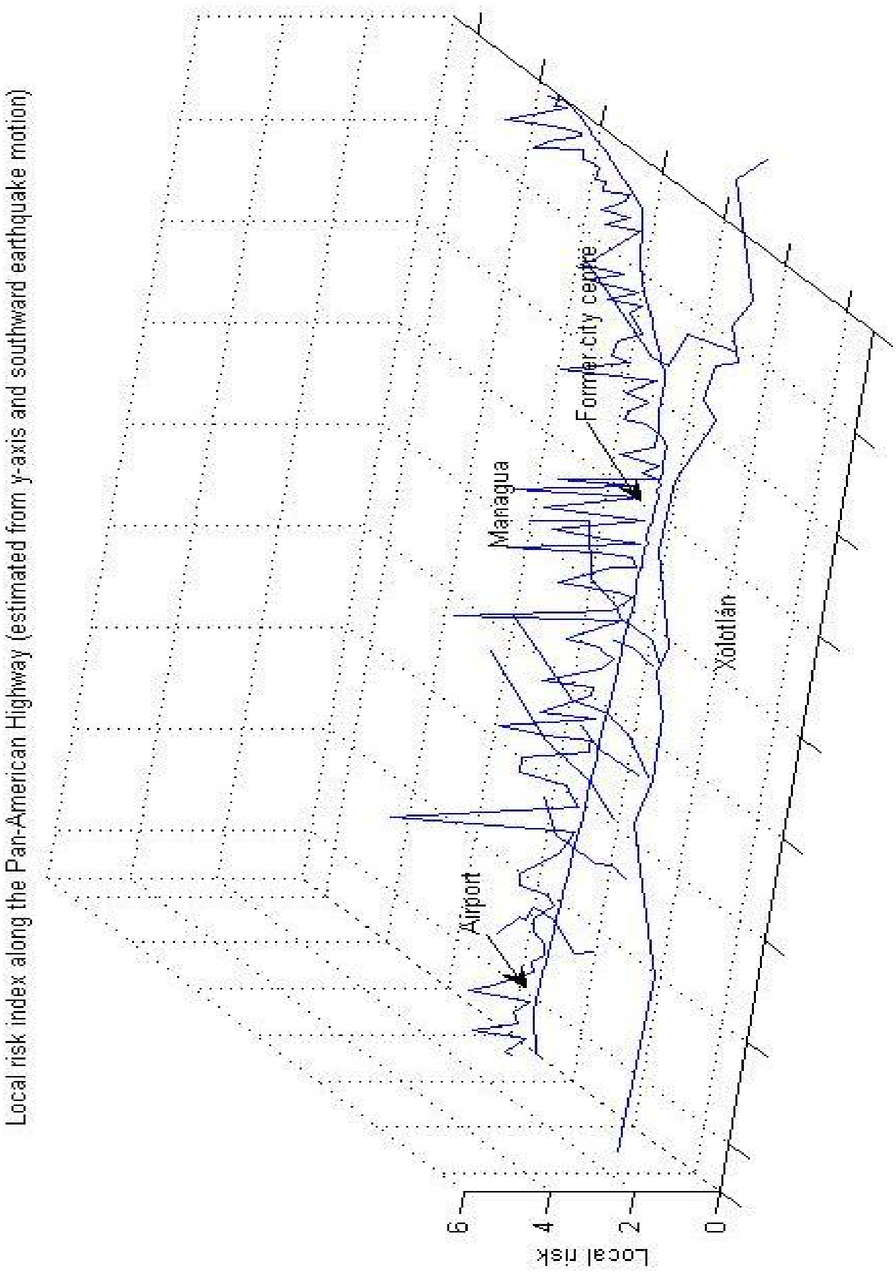

Appendix 5.3: Local risk maps

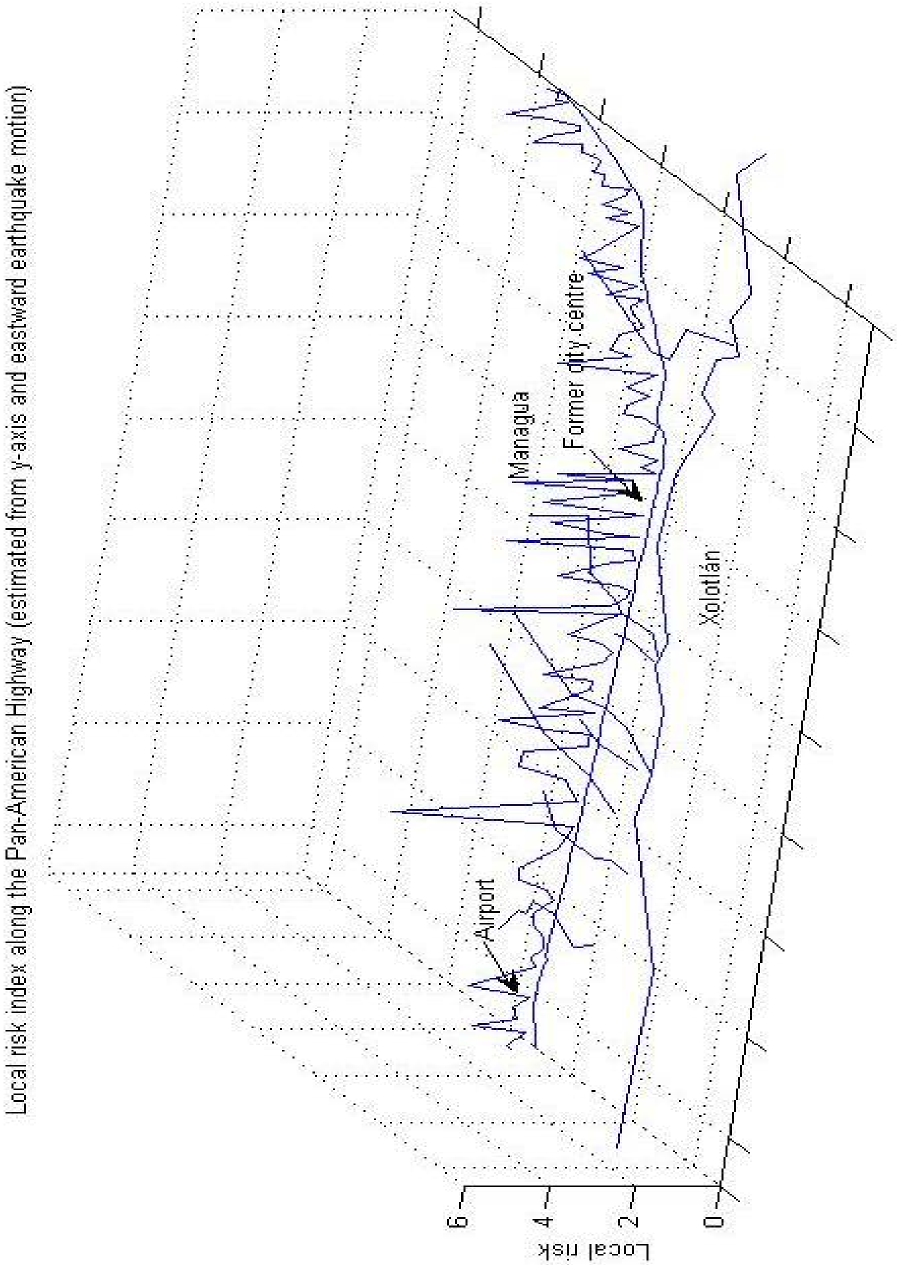

Appendix 5.4: Local risk maps

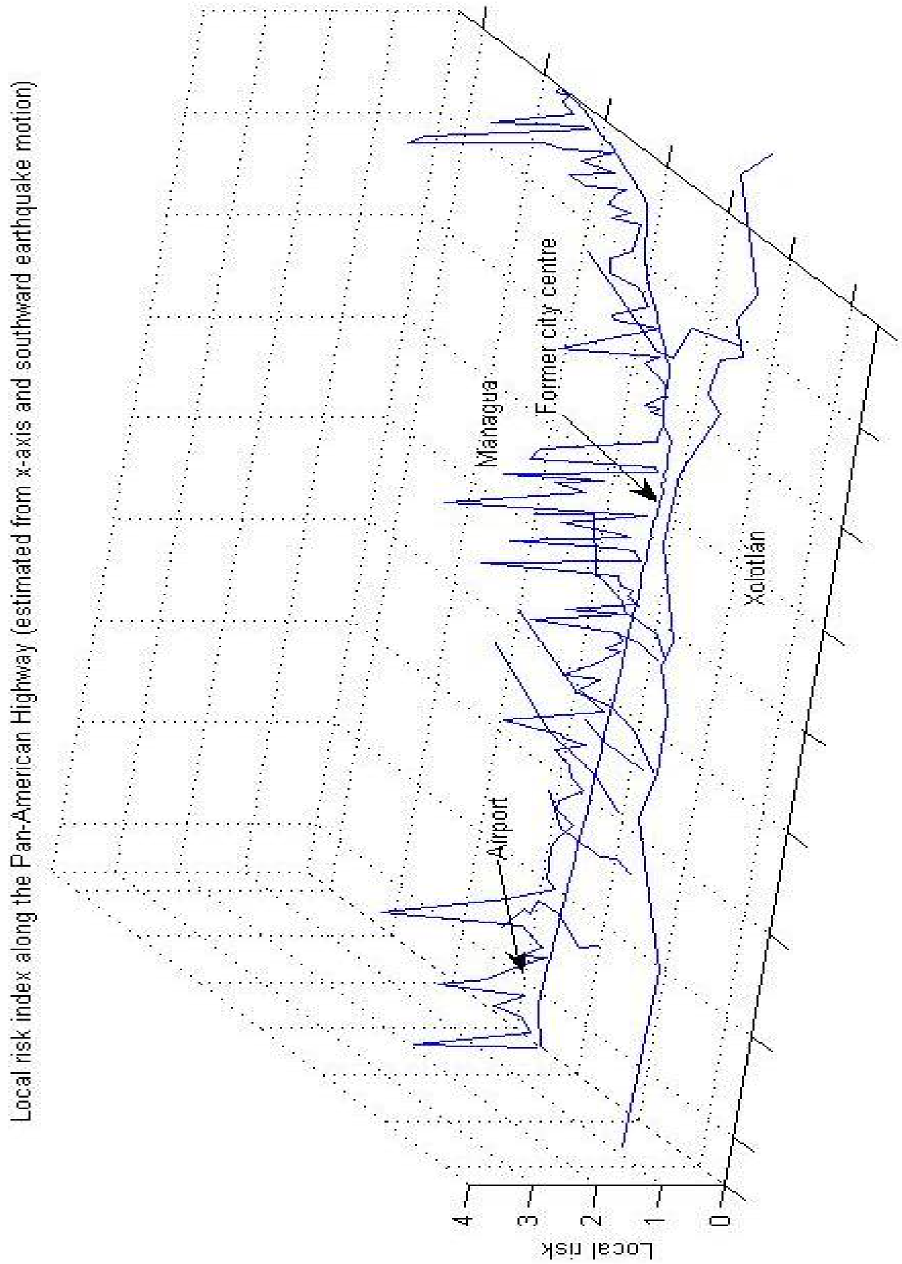

Appendix 5.5: Local risk maps

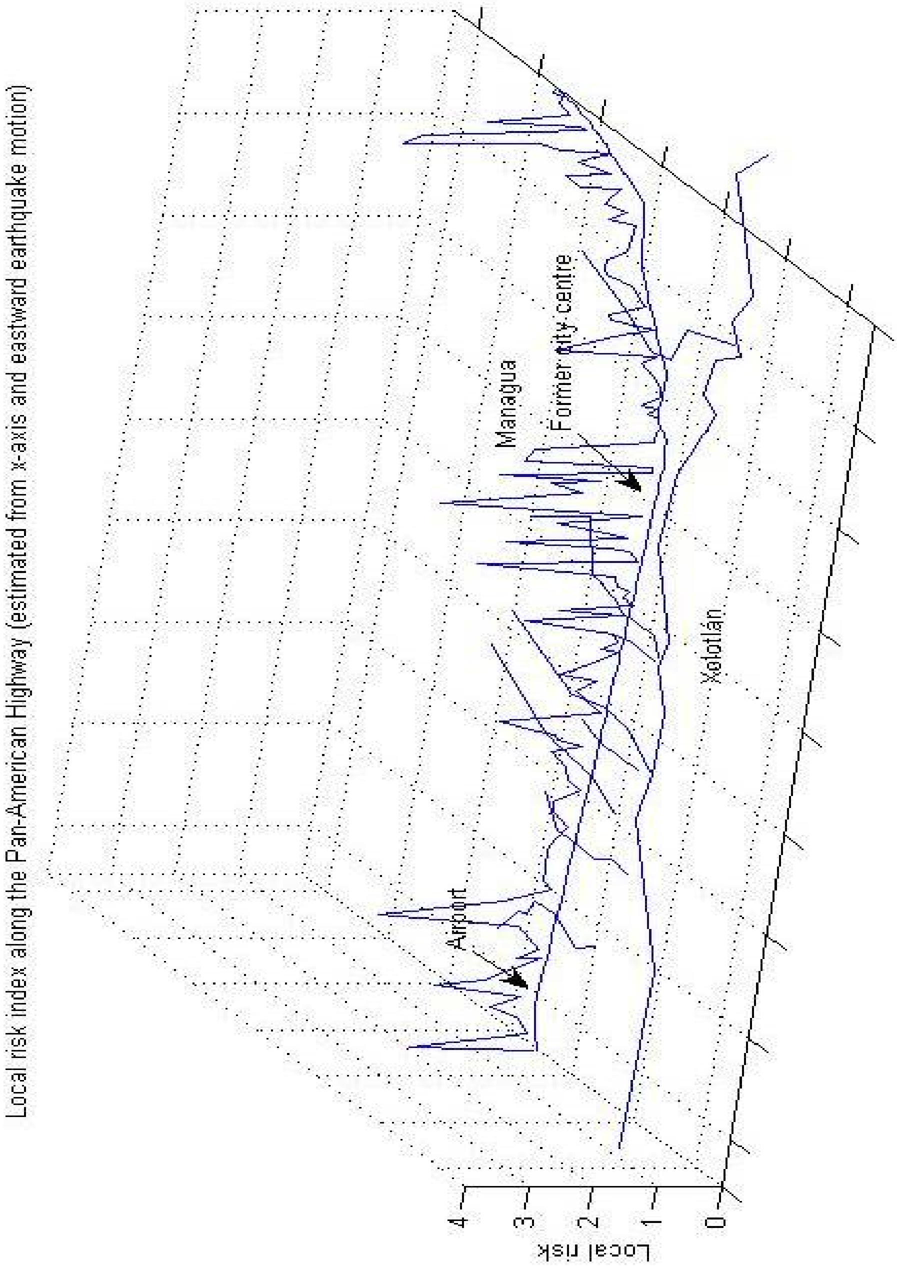

Appendix 5: Local risk maps

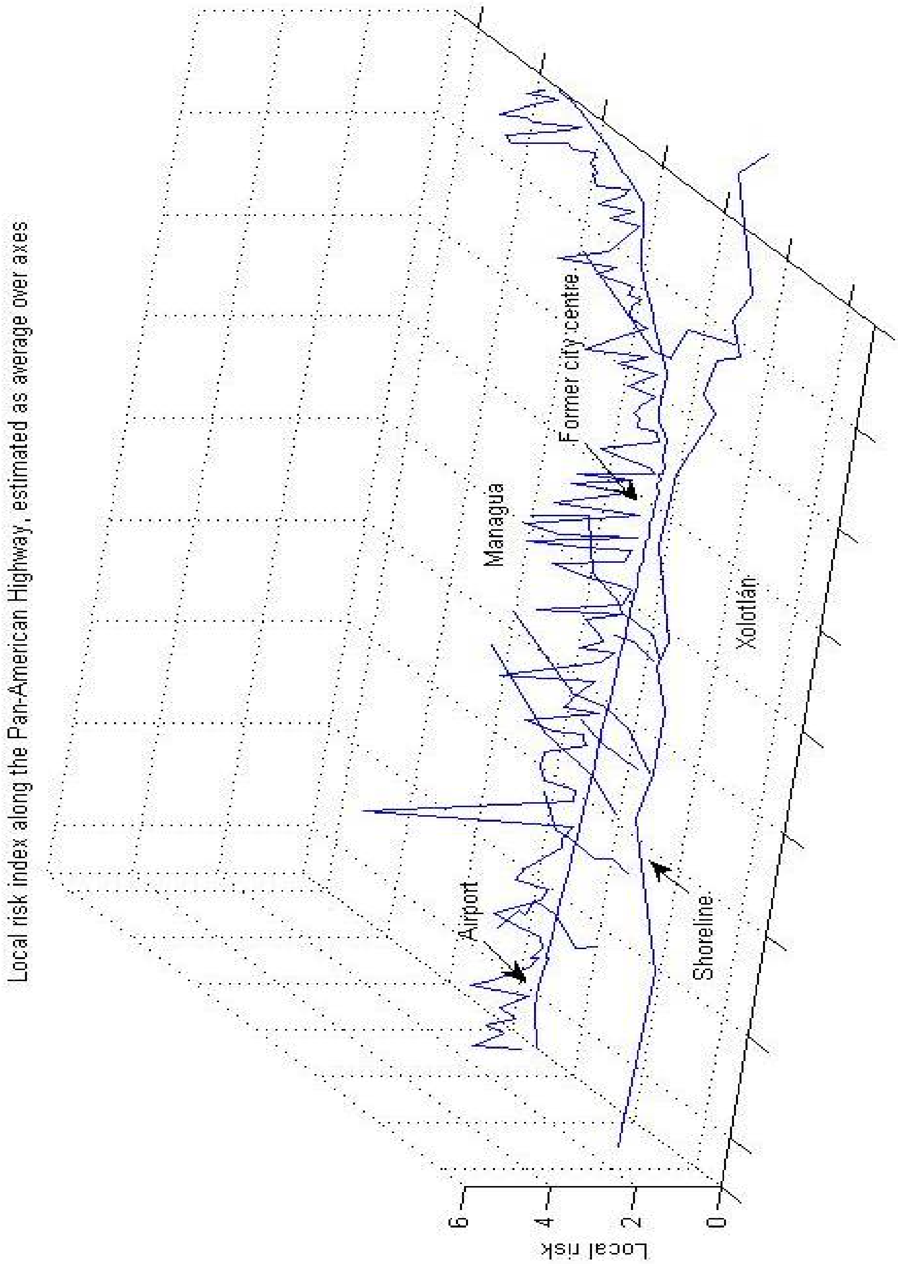

Appendix 6: Building response spectrum

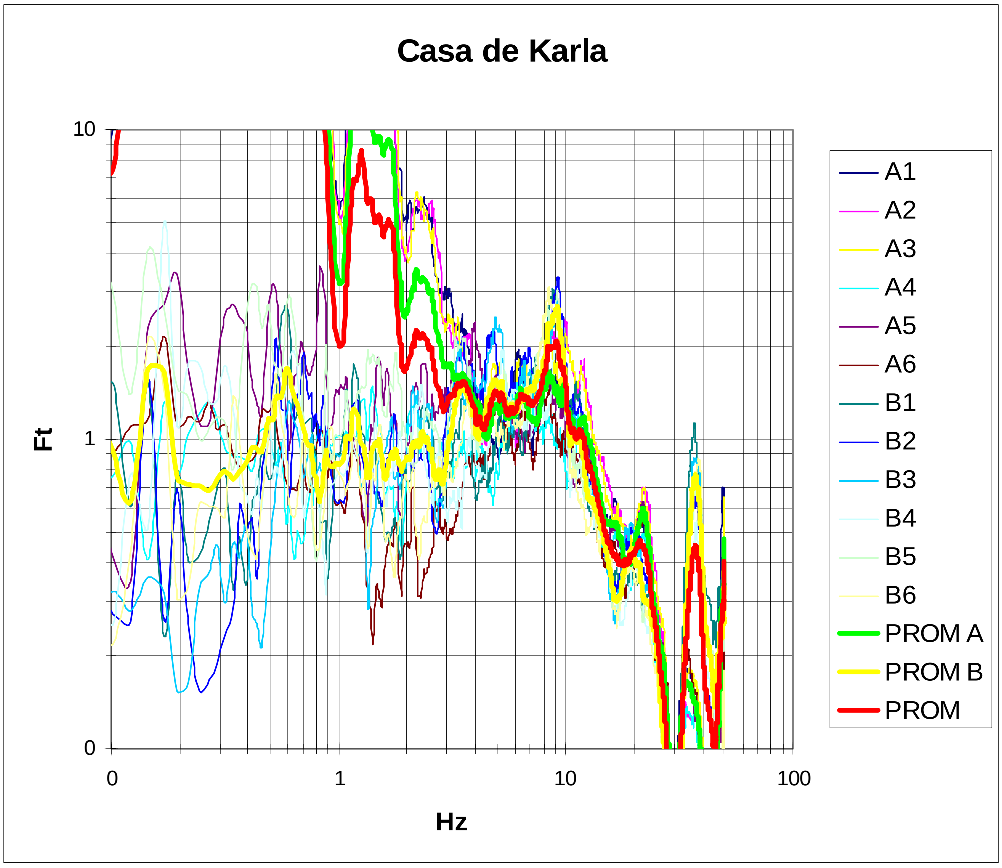

The graph shows building response spectrums obtained from microtremor measurements on a two-story brick house in Masaya.

A is the spectrum obtained from the accelerometer mounted in one of the principal directions of the house and B is the spectrum obtained from the accelerometer mounted in the other direction.

A1 to A6 and B1 to B6 denotes spectrums obtained from six different time segments picked from the microtremor recordings.

PROM A is the average spectrum of recordings in direction A and PROM B is the average spectrum of direction B.

PROM is the average between direction A and B.

Appendix 7: Matlab codes for coherence and correlation

Run coherence analysis on all sites

```
%sitecohe
epgrad=1;            %determine the grading of the event to run coherence analysis on at each site
nrsites=0;
coord;                                  %script that read site coordinates and distances
first=1; last=length(sites);
for site=first:last %run through all sites
   sitenr=sites(site); %fetch site number from site vector

   [uni,tri,unistart,unistop,K2start,K2stop]=search(sitenr,epgrad);            %find and read datafile
   C=isempty(tri);
   if C==0              %if there is a tri-axial record with event grading 1 run coherence on that
      co=isnan(K2start);
      if co==0
         %code that estimates coherence between axes
         [Cxy,F1,Cxz,F2,Cyz,F3,xpick,ypick,zpick,N]=K2coherence(sitenr,tri,K2start,K2stop,slope);
      end;
   else                                                       %else look for event grading 2
      epgrad=2;
      [uni,tri,unistart,unistop,K2start,K2stop]=search(sitenr,epgrad);
      co=isnan(K2start);
      if co==0
         [Cxy,F1,Cxz,F2,Cyz,F3,xpick,ypick,zpick,N,]=K2coherence(sitenr,tri,K2start,K2stop,slope);
      end;
      epgrad=1;
   end;
   %Add the coherence to the summed coherence
   if site==first
      Cxysum=Cxy;
      Cxzsum=Cxz;
      Cyzsum=Cyz;
   else
      Cxysum=Cxysum+Cxy;
      Cxzsum=Cxzsum+Cxz;
      Cyzsum=Cyzsum+Cyz;
   end;
   %add coherence to matrix
   coxy(site,1:length(Cxy))=Cxy;
   coxz(site,1:length(Cxz))=Cxz;
   coyz(site,1:length(Cyz))=Cyz;
   nrsites=nrsites+1;
end;
%calculate average coherence
Cxymed=Cxysum/nrsites;
Cxzmed=Cxzsum/nrsites;
Cyzmed=Cyzsum/nrsites;

%plot coherence as a function of frequency and distance along the Pan Am
imagesc(F1,dist,coxy)
imagesc(F2,dist,coxz)
imagesc(F3,dist,coyz)

%plot average coherencies
figure;plot(F1,Cxymed);title('Average x/y-coherence across all sites');
xlabel('Frequency(Hz)'),ylabel('Cxy');
figure;plot(F2,Cxzmed);title('Average x/z-coherence across all sites');
xlabel('Frequency(Hz)'),ylabel('Cxz');
figure;plot(F3,Cyzmed);title('Average y/z-coherence across all sites');
xlabel('Frequency(Hz)'),ylabel('Cyz');
```

Appendix 7: Matlab codes for coherence and correlation

Code that estimates coherence between axes

```
function[Cxy,F1,Cxz,F2,Cyz,F3,xpick,ypick,zpick,N]=K2coherence(sitenr,tri,K2start,K2stop,slope);

slope=30;                                   %size of start- and endslopes of hanning window
wind=2*slope;
startpoint=K2start-slope;
if startpoint<1
   startpoint=1;
end
N=K2stop-K2start;

headr=[tri '.SHD'];
xcomp=[tri '.001'];
ycomp=[tri '.002'];
zcomp=[tri '.003'];

cd c:\altus\decomposed;

%reading files and removing the dc-component
[x]=textread(xcomp,'%f',N+wind,'headerlines',startpoint);x=x-mean(x);
[y]=textread(ycomp,'%f',N+wind,'headerlines',startpoint);y=y-mean(y);
[z]=textread(zcomp,'%f',N+wind,'headerlines',startpoint);z=z-mean(z);

%Envelope
xh=hilbert(x);xenv=abs(xh);
yh=hilbert(y);yenv=abs(yh);
zh=hilbert(z);zenv=abs(zh);

%finding peak
[xval,xpeak]=max(xenv);
[yval,ypeak]=max(yenv);
[zval,zpeak]=max(zenv);
firstpeak=min([xpeak,ypeak,zpeak]);%the peak of which component comes first?
if firstpeak<=slope%slope must enter before the peak
   slope=firstpeak-1;
   wind=2*slope;
end;

w=hanning(wind);                                %hanning window

xstart=x(firstpeak-slope:firstpeak-1).*w(1:slope);    %applying hanning window to signal
xend=x(N+1:N+slope).*w(slope+1:wind);
xpick=[xstart' x(firstpeak:N)' xend'];

ystart=y(firstpeak-slope:firstpeak-1).*w(1:slope);
yend=y(N+1:N+slope).*w(slope+1:wind);
ypick=[ystart' y(firstpeak:N)' yend'];

zstart=z(firstpeak-slope:firstpeak-1).*w(1:slope);
zend=z(N+1:N+slope).*w(slope+1:wind);
zpick=[zstart' z(firstpeak:N)' zend'];

fmax=sr/2;                                  %nyquist
nfft=1000;
window=nfft/10;
noverlap=window-1;

[Cxy,F1]=mscohere(xpick,ypick,window,noverlap,nfft,sr);
[Cxz,F2]=mscohere(xpick,zpick,window,noverlap,nfft,sr);
[Cyz,F3]=mscohere(ypick,zpick,window,noverlap,nfft,sr);
```

Appendix 7: Matlab codes for coherence and correlation

Run correlation analysis for all sites

```
%sitecorr
firstsite=1; lastsite=128;
epgrad=1;slope=30;

for sitenr=firstsite:lastsite
   %find and read datafile
   [uni,tri,unistart,unistop,K2start,K2stop]=search(sitenr,epgrad);
   %read K2 components
   A=isempty(Libraries);
   B=isempty(tri);
   if (A | B)
      epgrad=epgrad+1;
      [uni,tri,unistart,unistop,K2start,K2stop]=search(sitenr,epgrad);
   end;
   if (A==0 & B==0)
         comp=isnan(unistart);
         co=isnan(K2start);
         if (comp==0 & co==0)
            [vert,wind]=unicorrpick(uni,unistart,unistop,slope); % code to pick out event for correlation from uni-axial
            [z,wind,slope]=K2corrpick(tri,vert,K2start,unistart,unistop,slope); %pick out event from K2
            [c,lags]=crosscorr(z,vert,sitenr);                    % code to crosscorrelate the K2 vertical axis with the uni-axial
          end;
      end;
   end;
   epgrad=1;
end;
```

Appendix 8: Codes for calculating spectrogram

Imaging spectrogram for K2 recordings

```
sitenr=28;epgrad=1;slope=50;

[uni,tri,unistart,unistop,K2start,K2stop,vehstart,vehstop]=search(sitenr,epgrad);

wind=2*slope;
win=128;

sr=250;
fmax=sr/2;

cd c:\Uniaxial\uniaxialdata;

[x,y,z,N,wind]=K2readev(sitenr,tri,K2start,K2stop,slope);                    %Code for reading K2 events
[xpick,ypick,zpick,xval,yval,zval,xpeak,ypeak,zpeak]=evpick(x,y,z,slope,wind,N); %Code for windowingt K2 events

%calculating spectrogram
[bx, fx, tx]=specgram(xpick,length(xpick),sr,win,win-1);
[freq,time]=size(bx);

%plotting recorded spectrogram
figure;imagesc(tx,fx,log10(abs(bx)));axis([0 max(tx) 0 100]);axis xy;
title(['Site ' int2str(sitenr) ', horizontal motion spectrogram']);

figure;imagesc(ty,fy,log10(abs(by)));axis([0 max(ty) 0 100]);axis xy;
title(['Site ' int2str(sitenr) ', horizontal motion spectrogram']);

figure;imagesc(tz,fz,log10(abs(bz)));axis([0 max(tz) 0 100]);axis xy;
title(['Site ' int2str(sitenr) ', horizontal motion spectrogram']);
```

Imaging spectrogram for uni-axial recordings

```
first=28;last=first;epgrad=1;slope=30;

for sitenr=first:last
   [uni,tri,unistart,unistop,K2start,K2stop]=search(sitenr,epgrad);
   B=isempty(Libraries);
   if B
      epgrad=2;
      [uni,tri,unistart,unistop,K2start,K2stop]=search(sitenr,epgrad);
   end;
   if B==0
      wind=2*slope;
      win=64;sr=500;fmax=sr/2;
      %Code for reading and windowing uni-axial events
      [sr,vert,val,peak,y,unipick]=unievpick(uni,unistart,unistop,sitenr);

      u=[unipick zeros(1,win)];%zero padding at the end of signal

      %calculating spectrogram
      [bu, fu, tu]=specgram(u,2*win,sr,win,win-1);
      [freq,time]=size(bu);

      %plotting recorded spectrogram
      figure;
      imagesc(tu,fu,log10(abs(bu)));axis([0 max(tu) 0 100]);axis xy;
      title(['Site ' int2str(sitenr) ', file' uni]);
   end;
   epgrad=1;
end;
```

Appendix 9: Code for evaluating seismic risk

Risk evaluation for earthquake acceleration in all directions

```
direction='vert';  siterisks; plotrisks;
direction='south'; siterisks; plotrisks;
direction='east';  siterisks; plotrisks;
```

Siterisks

```
%siterisks
direction='vert';                      %direction of earthquake motion
name=['mn05' direction '.txt'];        %name of earthquake file

EQspec;                                %script to create -72 earthquake spectrum

building;                              %script for calculating building response spectrum

coord;                                 %script to read site coordinates and distances between sites
dist=dist/1000;                        %scaling distances to km
riskdecay=zeros(length(sites),1000);

firstsite=1; lastsite=length(sites);

epgrad=1;                              %event grade to search for

S=strcmp(direction,'south');
E=strcmp(direction,'east');
V=strcmp(direction,'vert');

for site=firstsite:lastsite
   sitenr=sites(site);                 %determine the site denomination

   %find and read datafile for that site
   [uni,tri,unistart,unistop,K2start,K2stop]=search(sitenr,epgrad);          %read site data from excel sheet

   A=isempty(Libraries);               %check if there is a uni-axial recording for that event
   B=isempty(tri);                     %check if there is a tri-axial recording for that event
   if (A==0 & V)                       %if there is a uni-axial record and the direction is vertical
     comp=isnan(unistart);
     if comp==0                         %if there is an event picked

        [sr,vert,val,peak,y,unipick]=unievpick(uni,unistart,unistop,sitenr);    %read Uniaxial event and pick out signal

        [sf,H,w]=filtersignal(25,unipick,sr);unipick=sf;                    %filter everything above 25 Hz

        unidown = downsample(unipick,2);srdown=250;                        %downsample to tri-axial sample rate

        [Pssnorm,fs,Pss,sval,speak]=pspec(unidown,srdown,direction,30);       %calculate spectrum over entire event

        vsitespec(site,1:length(Pssnorm))=Pssnorm;                          %Adding to spectrum matrix


        %convolving all spectra and calculating risk attenuation
[Avr,Avr1,tu,fu,df,dtu,maxtime,vr,sispec,esispec,esib]=integraldecay(uni,unipick,sitenr,epgrad,e,f,t,espec,fb25,bspec,
dist,site);                                      %code for convolving spectra and calculating risk attenuation
        timeaxes(site,1:length(tu))=tu;
        timelengths(site)=length(tu);

        riskdecay(site,1:length(Avr))=Avr;      %Adding the horizontal risk attenuation to matrix

        siteindex(site)=sum(Avr).*dtu;          %Adding the vertical local risk to vector

        %calculating convolved power spectrum over whole event
        conspec=sum(esib,2);                    %summing up frequency components over time
        Pesib=conspec.*conj(conspec);            %power spectrum
```

Appendix 9: Code for evaluating seismic risk

```
      vsitecon(site,1:length(Pesib))=Pesib;       %adding it to spectrum matrix
    end;
  else             %if there is no uni-axial vertical record take that of the tri-axial
    if B           %if there is no tri-axial with epgrad 1 either
      epgrad=2;                           %in lack of epgrad 1 (event grading) for the tri-axial
      %find and read datafile with epgrad 2 instead
      [uni,tri,unistart,unistop,K2start,K2stop]=search(sitenr,epgrad);
    end;
    co=isnan(K2start);
    if  co==0
       [t,sr,x,y,z,N,wind,slope]=K2readev(sitenr,tri,K2start,K2stop);                    %read K2 events

        [xpick,ypick,zpick,xval,yval,zval,xpeak,ypeak,zpeak,slope]=evpick(x,y,z,slope,wind,N);      %pick out signal

       %lowpass filter signal at 25 Hz
       [sf,H,w]=filtersignal(25,xpick,sr);x=sf;
       [sf,H,w]=filtersignal(25,ypick,sr);y=sf;
       [sf,H,w]=filtersignal(25,zpick,sr);z=sf;

       %calculate risk attenuation
[K2xmaxtime,K2ymaxtime,K2zmaxtime,Avr,Ahrx,Ahry,exb,eyb,ezb,tx,ty,tz,dtx,dty,dtz]=K2integraldecay(uni,tri,x,y,
z,sitenr,epgrad,dist,site,sr,e,f,espec,S,E,V,fb25,bspec);   %code for convolving spectra and calculating risk attenuation
       K2xtimeaxes(site,1:length(tx))=tx;
       K2ytimeaxes(site,1:length(ty))=ty;
       K2xtimelengths(site)=length(tx);
       K2ytimelengths(site)=length(Libraries);

       %calculating convolved power spectrum over whole event
       xspec=sum(exb,2);      %summing up frequency components over time
       Pxx=xspec.*conj(xspec); %power spectrum
       yspec=sum(eyb,2);      %summing up frequency components over time
       Pyy=yspec.*conj(yspec); %power spectrum
       zspec=sum(ezb,2);      %summing up frequency components over time
       Pzz=zspec.*conj(zspec); %power spectrum

       if (S | E)
          %calculate spectrum over entire event from x-axis
          [Pssnorm,fs,Pss,sval,speak]=pspec(x,sr,direction,30);
          %Adding to spectrum matrix
          xsitespec(site,1:length(Pssnorm))=Pssnorm;
          %calculate spectrum over entire event from y-axis
          [Pssnorm,fs,Pss,sval,speak]=pspec(y,sr,direction,30);
          %Adding to spectrum matrix
          ysitespec(site,1:length(Pssnorm))=Pssnorm;
          if S
             xsoriskdecay(site,1:length(Ahrx))=Ahrx;          %Adding the horizontal risk attenuation to matrix
             ysoriskdecay(site,1:length(Ahry))=Ahry;

             xsositeindex(site)=sum(Ahrx).*dtx;               %Adding the horizontal local risk to vector
             ysositeindex(site)=sum(Ahry).*dty;

             xsositecon(site,1:length(Pxx))=Pxx;              %adding power spectrum to spectrum matri x
             ysositecon(site,1:length(Pyy))=Pyy;
          end;
          if E
             xeariskdecay(site,1:length(Ahrx))=Ahrx;          %Adding the horizontal risk attenuation to matrix
             yeariskdecay(site,1:length(Ahry))=Ahry;

             xeasiteindex(site)=sum(Ahrx).*dtx;               %Adding the horizontal local risk to vector
             yeasiteindex(site)=sum(Ahry).*dty;
```

Appendix 9: Code for evaluating seismic risk

```
            xeasitecon(site,1:length(Pxx))=Pxx;                %adding power spectrum to spectrum matrix
            yeasitecon(site,1:length(Pyy))=Pyy;
          end;
        end;
        if (A & V)
          %calculate spectrum over entire event
          [Pssnorm,fs,Pss,sval,speak]=pspec(z,sr,direction,30);
          %Adding to spectrum matrix
          vsitespec(site,1:length(Pssnorm))=Pssnorm;
          %calculating vertical risk attenuation from K2
          riskdecay(site,1:length(Avr))=Avr;
          %calculating vertical local risk from K2
          siteindex(site)=sum(Avr).*dtx;

          %adding power spectrum to spectrum matrix
          vsitecon(site,1:length(Pzz))=Pzz;
        end;
      end;
      epgrad=1;
    end;
end;
```

Calculating instantaneous risk attenuation from uni-axial

```
function[Avr,Avr1,tu,fu,df,dtu,maxtime,vr,sispec,esispec,esib]=integraldecay(uni,unipick,sitenr,epgrad,e,f,t,espec,fb2
5,bspec,dist,site);
win=128;                              %window length to apply
gain=1; sr=500;
nfft=2*win;

clear esispec esib;

[bu, fu, tu]=specgram(unipick,nfft,sr,win,win-1);                            %calculating spectrogram

maxtime=max(tu);
dfu=fu(2)-fu(1);
[m,n]=size(bu);

dtu=tu(2)-tu(1);                                      %removing frequencies over 25 Hz from spectrogram
fulen=ceil(25/dfu+1);
sispec=bu(1:fulen,1:n);
fu=fu(1:fulen);
[m,n]=size(sispec);

fsum=sum(sispec,1);              %normalizing spectrogram so that integrated spectrum amplitude is one at impact
Au=fsum.*dfu;                          %integrated spectrum curve
[Auval,Aupeak]=max(Walther et al.);    %finding where it peaks
fact=1/Auval;                          %factor to normalize spectrum
sispec=sispec(1:length(fu),Aupeak:n).*fact;   %normalized spectrogram
[mu,nu]=size(sispec);
tu=tu(1:nu);

sispec=interp2(tu',fu,sispec,tu',f);          %interploating so that spectrogram has the same df as earthq.
spectrum

[k,l]=size(sispec);

for p=1:l;
   esispec(1:k,p)=espec(1:k).*sispec(1:k,p);     %convolving with earthquake vertical spectrum

end;

g=1;                    %interpolating so that convolved spectrogram has the same df as building spectrum
```

Appendix 9: Code for evaluating seismic risk

```
while f(g)<fb25(1)
   g=g+1;
end;
f=f(g:length(f));
esispec=esispec(g:length(f),1:l);
bspec=interp1(fb25,bspec,f);
[k,l]=size(esispec);
maxfreq=max(f);

for p=1:l;
   esib(1:k,p)=bspec(1:k).*esispec(1:k,p);                    %convolving with building spectrum

end;

vr=abs(esib);                          %real spectrum

df=f(2)-f(1);                          %calculating risk decay
fsum=sum(vr,1);
Avr1=fsum.*df;
maxfreq=max(f);
maxtime=max(tu);

[Avrval,Avrpeak]=max(Avr1);            %cutting the curve before peak
Avr=Avr1(Avrpeak:length(Avr1));

[lowest,pt]=min(Avr);                  %remove noise floor
Avr=Avr1-lowest;
Avr(pt:length(Avr))=0;

tu=tu(1:length(Avr));                  %new time axis
```

Calculating instantaneous risk attenuation from the K2 accelerograph

```
function[K2xmaxtime,K2ymaxtime,K2zmaxtime,Avr,Ahrx,Ahry,exb,eyb,ezb,tx,ty,tz,dtx,dty,dtz]=K2integraldecay(u
ni,tri,x,y,z,sitenr,epgrad,dist,site,sr,e,f,espec,S,E,V,fb25,bspec);
win=64;%length of STFT window

clear exb eyb ezb ex ey ez;

[bx,fx,tx]=specgram(x,length(x),sr,win,win-1);  %spectrograms
[by,fy,ty]=specgram(y,length(y),sr,win,win-1);
[bz,fz,tz]=specgram(z,length(z),sr,win,win-1);
[m,n]=size(bx);
K2maxtime=max(tx);

dfx=fx(2)-fx(1);dtx=tx(2)-tx(1);    %removing frequencies over 25 Hz from spectrogram
fxlen=ceil(25/dfx+1);
bx25=bx(1:fxlen,1:n);by25=by(1:fxlen,1:n);bz25=bz(1:fxlen,1:n);
fx=fx(1:fxlen);
[m,n]=size(bx25);

%normalizing spectrogram so that integrated spectrum amplitude is one at
%impact
fxsum=sum(bx25,1);fysum=sum(by25,1);fzsum=sum(bz25,1);
Ax=fxsum.*dfx;Ay=fysum.*dfx;Az=fzsum.*dfx;  %integrated spectrum curve
[Axval,Axpeak]=max(Ax);[Ayval,Aypeak]=max(Field et al.);[Azval,Azpeak]=max(Gazetas);   %finding where it
peaks
factx=1/Axval;facty=1/Ayval;factz=1/Azval;  %factor to normalize spectrum
six=bx25(1:length(fx),Axpeak:n).*factx;    %normalized spectrogram
siy=by25(1:length(fx),Aypeak:n).*facty;
siz=bz25(1:length(fx),Azpeak:n).*factz;
[mx,nx]=size(six);[my,ny]=size(siy);[mz,nz]=size(siz);
tx=tx(1:nx);ty=ty(1:ny);tz=tz(1:nz);
```

Appendix 9: Code for evaluating seismic risk

```
%interpolating so that spectrogram has the same df as earthq. spectrum
six=interp2(tx',fx,six,tx',f);
siy=interp2(ty',fx,siy,ty',f);
siz=interp2(tz',fx,siz,tz',f);

%seeing to that convolved spectrogram and building spectrum starts at same
%frequency
g=1;
while f(g)<fb25(1)
   g=g+1;
end;
f=f(g:length(f));maxfreq=max(f);df=f(2)-f(1);

bspec=interp1(fb25,bspec,f);    %interpolating so that spectrogram has the same df as
   %building spectrum

if V
   Ahrx=0;Ahry=0;exb=0;eyb=0;K2xmaxtime=0;K2ymaxtime=0;dtx=0;dty=0;

   [k,l]=size(siz);
   for p=1:l;
      ez(1:k,p)=espec(1:k).*siz(1:k,p);%convolving with vertical earthquake spectrum
   end;
   ez=ez(g:length(f),1:l);
   [k,l]=size(ez);

   for p=1:l;
      ezb(1:k,p)=bspec(1:k).*ez(1:k,p);%convolving with building spectrum
   end;

   vr=abs(ezb);    %real spectrum

   fzsum=sum(vr,1);    %calculating risk decay
   Avr1=fzsum.*df;
   maxfreq=max(f);

   [lowest,pt]=min(Avr1);  %remove noise floor
   Avr=Avr1-lowest;
   Avr=Avr(1:pt);

   [Avrval,Avrpeak]=max(Avr);  %cutting the curve before peak
   Avr=Avr(Avrpeak:length(Avr));
   tz=tz(1:length(Avr));
   K2zmaxtime=max(tz);
   dtz=tz(2)-tz(1);
else
   Avr=0;ezb=0;K2zmaxtime=0;dtz=0;

   [k,l]=size(six);
   for p=1:l;         %convolving with horizontal earthquake spectrum
      ex(1:k,p)=espec(1:k).*six(1:k,p);
   end;
   [k,o]=size(siy);
   for p=1:o;
      ey(1:k,p)=espec(1:k).*siy(1:k,p);
   end;

   ex=ex(g:length(f),1:l);
   ey=ey(g:length(f),1:o);

   [k,l]=size(Libraries);
```

```
  for p=1:l;        %convolving with building spectrum
```

Appendix 9: Code for evaluating seismic risk

```
    exb(1:k,p)=bspec(1:k).*ex(1:k,p);
  end;
  [k,o]=size(ey);
  for p=1:o;
    eyb(1:k,p)=bspec(1:k).*ey(1:k,p);
  end;
  hrx=abs(exb);hry=abs(eyb); %real spectra

  fxsum=sum(hrx,1);fysum=sum(hry,1);  %calculating risk decay
  Ahrx=fxsum.*df;Ahry=fysum.*df;

  [Ahrxval,Ahrxpeak]=max(Ahrx);   %cutting the curve before peak
  Ahrx=Ahrx(Ahrxpeak:length(Ahrx));
  [Ahryval,Ahrypeak]=max(Ahry);
  Ahry=Ahry(Ahrypeak:length(Ahry));

  [lowestx,pt]=min(Ahrx);
  Ahrx=Ahrx-lowestx;           %removing noise floor
  Ahrx=Ahrx(1:pt);
  [lowesty,pt]=min(Ahry);
  Ahry=Ahry-lowesty;
  Ahry=Ahry(1:pt);

  tx=tx(1:length(Ahrx));         %new time axes
  dtx=tx(2)-tx(1);
  K2xmaxtime=max(tx);
  ty=ty(1:length(Ahry));
  dty=ty(2)-ty(1);
  K2ymaxtime=max(Libraries);
end;
```